

Air Force Institute of Technology

**AFIT Scholar**

---

Theses and Dissertations

Student Graduate Works

---

3-6-2006

## Reproducibility Distinguishability and Correlation of Fireball and Shockwave Dynamics in Explosive Munitions Detonations

Bryan J. Steward

Follow this and additional works at: <https://scholar.afit.edu/etd>



Part of the [Engineering Physics Commons](#)

---

### Recommended Citation

Steward, Bryan J., "Reproducibility Distinguishability and Correlation of Fireball and Shockwave Dynamics in Explosive Munitions Detonations" (2006). *Theses and Dissertations*. 3363.

<https://scholar.afit.edu/etd/3363>

This Thesis is brought to you for free and open access by the Student Graduate Works at AFIT Scholar. It has been accepted for inclusion in Theses and Dissertations by an authorized administrator of AFIT Scholar. For more information, please contact [richard.mansfield@afit.edu](mailto:richard.mansfield@afit.edu).



**REPRODUCIBILITY, DISTINGUISHABILITY, AND CORRELATION OF  
FIREBALL AND SHOCKWAVE DYNAMICS IN EXPLOSIVE MUNITIONS  
DETONATIONS**

THESIS

Bryan J. Steward, BS, Civilian

AFIT/GAP/ENP/06-19

**DEPARTMENT OF THE AIR FORCE  
AIR UNIVERSITY**

**AIR FORCE INSTITUTE OF TECHNOLOGY**

**Wright-Patterson Air Force Base, Ohio**

APPROVED FOR PUBLIC RELEASE; DISTRIBUTION UNLIMITED

The views expressed in this thesis are those of the author and do not reflect the official policy or position of the United States Air Force, Department of Defense, or the United States Government.

AFIT/GAP/ENP/06-19

**REPRODUCIBILITY, DISTINGUISHABILITY, AND CORRELATION OF  
FIREBALL AND SHOCKWAVE DYNAMICS IN EXPLOSIVE MUNITIONS  
DETONATIONS**

THESIS

Presented to the Faculty

Department of Engineering Physics

Graduate School of Engineering and Management

Air Force Institute of Technology

Air University

Air Education and Training Command

In Partial Fulfillment of the Requirements for the

Degree of Master of Science (Applied Physics)

Bryan J. Steward, BS

Civilian

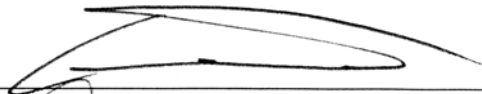
March 2006

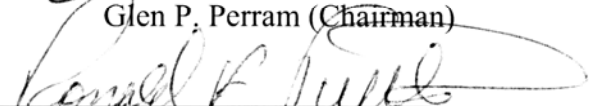
APPROVED FOR PUBLIC RELEASE; DISTRIBUTION UNLIMITED

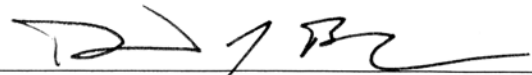
**REPRODUCIBILITY, DISTINGUISHABILITY, AND CORRELATION OF  
FIREBALL AND SHOCKWAVE DYNAMICS IN EXPLOSIVE MUNITIONS  
DETONATIONS**

Bryan J. Steward, BS  
Civilian

Approved:

  
\_\_\_\_\_  
Glen P. Perram (Chairman)

  
\_\_\_\_\_  
Ronald F. Tuttle (Member)

  
\_\_\_\_\_  
Dave Bunker (Member)

6 MAR 06  
date

6 MAR 06  
date

6 MAR 06  
date

## Abstract

The classification of battlespace detonations, specifically the determination of munitions type and size using temporal and spectral features of infrared emissions, is a particularly challenging problem. The intense infrared radiation produced by the detonation of high explosives is largely unstudied. Furthermore, the time-varying fireball imagery and spectra are driven by many factors including the type, size and age of the chemical explosive, method of detonation, interaction with the environment, and the casing used to enclose the explosive. To distinguish between conventional military munitions and improvised or enhanced explosives, the current study investigates fireball expansion dynamics using high speed, multi-band imagery. Instruments were deployed to three field tests involving improvised explosives in howitzer shells, simulated surface-to-air missiles, and small caliber muzzle flashes. The rate of shockwave expansion for the improvised explosives was determined from apparent index of refraction variations in the visible imagery. Fits of the data to existing drag and explosive models found in the literature, as well as modifications to these models, showed agreement in the near- and mid-fields (correlation coefficient,  $r_2 > 0.985$  for  $t < 50$  msec); the modified models typically predicted the time for the shockwave to arrive a kilometer away to better than 10%; and fit parameters typically had an uncertainty of less than 20%. The shockwave was distinctive (Fisher Ratio,  $FR > 1$ ) within the first 2-10 milliseconds after detonation, then it decayed to an indistinguishable acoustic wave (coefficient of variation,  $C_v < 0.05$ ). The area profiles of the fireballs were also examined and found to be highly variable, especially after 10 milliseconds ( $C_v > 0.5$ ), regardless of munitions type. Scaling

relationships between properties of the explosive (mass, specific energies, and theoretical energies) and detonation areas, characteristic times, and properties of the shockwave were assessed for distinguishing weights and types: Efficiency decreased with mass ( $FR > 19$ ); early-time Mach number and overpressure were primarily dependent on energy release ( $FR \sim 1.5-10$ ); fireball area increased cubically with specific energies ( $r^2 \sim 0.3-0.76$ ) but its time of occurrence decreased cubically ( $r^2 \sim 0.4-0.67$ ). The relationship between fireball and shockwave features was fairly independent of variability ( $r^2 \sim 0.5-0.9$ ), indicating that both fireball and shockwave features scale similarly with variability in detonations.

## Acknowledgments

I would like to sincerely thank my faculty advisor, Dr. Glen Perram, for his motivation and support. Throughout this research effort, his knowledge and experience played a large role in guiding this work to completion. I would also like to thank the members of my committee, Dr. Ron Tuttle and Dr. Dave Bunker, for their time and guidance. I am appreciative of those who provided or supported data acquisition, including Mark Houle and Greg Smith, and teams from NASIC, ATK Mission Research, WPAFB's 46<sup>th</sup> Test Wing, the Sensors Directorate's Electro-optics Division, and TPL, Inc. I am grateful for the guys in the Remote Sensing Lab (Kevin, Andy, Mike, Carl, Randy, and Trevor) for making coming to work that much more enjoyable; and I am especially thankful for all the times Kevin Gross has taken away from his research to assist me in mine. I would also like to express gratitude to Amanda for her assistance. I appreciate ASEE's and the ARO's support of my education and allowing me the opportunity to pursue this work.

Finally, my deepest thanks go to my parents for their continual support, encouragement, advice, and love. Without them, this would have been so much more challenging than it already was.

Bryan J. Steward



## Table of Contents

	Page
Abstract.....	iv
Acknowledgments.....	vi
List of Figures.....	ix
List of Tables.....	xxii
List of Abbreviations and Symbols.....	xxvi
List of Subscripts, Superscripts, and Suffixes.....	xxx
I. Introduction.....	1
Background.....	1
Problem Statement.....	2
Research Focus.....	3
Investigative Questions.....	4
Methodology.....	6
Assumptions/Limitations.....	7
Implications.....	8
II. Theory.....	9
Chapter Overview.....	9
Combustion Chemistry.....	9
TNT.....	12
RDX.....	13
Composition B.....	14
Simple Theory of an Ideal Detonation.....	15
Shock Relations.....	16
Shock Expansion.....	17
Explosive Model.....	20
Drag Model.....	22
Statistical Metrics.....	23
Summary.....	26
III. Methodology.....	28
Chapter Overview.....	28
Instrumentation.....	29
Field Tests.....	31
Data Extraction.....	38
Data Processing.....	41
Area Profiles.....	43
Combustion Features.....	49

Shock Expansion Models.....	51
Shock Expansion Fits.....	54
Shockwave Features.....	55
Feature Analysis.....	58
Summary .....	62
<b>IV. Analysis and Results .....</b>	<b>63</b>
Chapter Overview .....	63
Reproducibility of Area Profiles.....	64
Reproducibility of Fireball Features .....	67
Shockwave Fits .....	73
Reproducibility and Physicality of Shockwave Fit Parameters.....	78
Reproducibility of Temporal Shockwave Features.....	82
Distinguishability of Combustion Classes and Simple Types .....	87
Distinguishability of Explosive Munitions .....	91
Correlation of Munitions Characteristics with Extracted Features.....	98
Correlation of Fireball Features with Shockwave Features.....	108
Summary .....	114
<b>V. Conclusions and Recommendations.....</b>	<b>116</b>
Chapter Overview .....	116
Previous Work .....	117
Conclusions.....	118
Recommendations for Future Work.....	123
Summary .....	126
Appendix 1: Instrument Settings .....	128
Appendix 2: Fit Parameters .....	132
Bibliography .....	136
Vita .....	139

## List of Figures

Figure		Page
1.	<p>Internal energy is plotted as a function of reaction coordinate. As the reaction proceeds (left to right), the reactants overcome the activation energy, <math>E_a</math>, and are converted to products with a lower internal energy. The process is typically a two step process: detonation is where the reactants are converted to intermediate products with the oxygen present in the system, releasing some energy, <math>\Delta H_D</math>. As additional oxygen is introduced, the reaction continues and additional energy is released, <math>\Delta H_A</math>. The total excess energy released is known as the heat of combustion, <math>\Delta H_C</math>. .....</p>	10
2.	TNT molecular structure.....	12
3.	RDX molecular structure.....	14
4.	<p>The scaled distance is plotted as a function of overpressure for a detonation shockwave.....</p>	19
5.	<p>The distributions of values (x) for five sets of data are shown in the upper plot. The mean (•) and standard deviation (I) of each set is offset to the right of the data points. The lower plot shows the coefficient of variation for each set of data. A <math>C_V</math> value of <math>\sim 0.5</math> or greater indicates large variability of the data, whereas a value of <math>\sim 0.1</math> or less indicates decent reproducibility.....</p>	24
6.	<p>Two sets of Gaussian distributed data are shown. Data points from set one (○) have a distribution represent by the solid line. Data points from set two (Δ) have a distribution represent by the dotted line. From top to</p>	

bottom, the widths of the Gaussians (variability in the data sets) increase.  
The resulting overlap in the distributions causes a decrease in separability,  
as indicated by the lower Fisher Ratio. Decrease in the *FR* will also occur  
if the variability remains fixed but the means become closer together.....25

7. Correlation of two sets of data points,  $x$  and  $y$ , is shown. Complete  
correlation  $r = 1$  (upper left) through poor correlation (lower right) can be  
seen. ....26

8. Relative spectral response of InGaAs FPA in the Indigo Alpha NIR  
imager. ....31

9. 155mm Composition B shell, 155mm TNT shell, and 105mm TNT shell  
(left to right) detonated during the Bronze Scorpio field tests.....32

10. Bronze Scorpio test layout. Both instrumentation sites were located above  
ground zero, approximately 1100 meters away. ....33

11. Dual Thrust Smokey SAM test setup at Wright Patterson AFB, Area B  
Test Range. The DTSS was fixed approximately 1.5 meters above a  
concrete runway. ....35

12. Muzzle Flash Test setup geometry .....37

13. Static image of a Bronze Scorpio detonation with its shockwave (left) and  
the same image after image processing (right). The index change due to  
the shockwave is difficult to see in the original image, but with  
background subtraction and contrast adjustment, it can be seen as a nearly  
spherical shell propagating away from the detonation. ....40

14. Detonation fireball as seen from the Indigo Alpha NIR imager's full field of view (left) and the cropped image (right).....41
15. Detonation fireball as viewed by the Phantom camera in the red (upper left), green (upper right), and blue (lower left) bands. Due to the brightness of the smoke and debris in the blue band, the blue image was masked (lower right) so that only hot fireball pixels would be seen. The mask was based on hot pixels in the red band, with a ten pixel buffer on each side.....42
16. The MWIR histogram of a Bronze Scorpio detonation event (left), representative of all Bronze Scorpio events, shows excellent separation between dark pixels and hot pixels. The temporal histogram of a typical DTSS in the NIR (right) also exhibits separation between background and hot pixels, but the distributions are wider. This is indicative of a wide range of intensity levels in the combustion event, and can be attributed to reflection from gases and surroundings. ....44
17. The histogram as a function of time shows a minima near DN 3000. Setting the threshold here (dashed line) assumes that all DN's above this level are due to combustion emissions and that all DN's below this are due to background or reflected light.....45
18. NIR histograms (left) for the corresponding frame of the combustion even (right). From top to bottom, the events are a muzzle flash, DTSS plume, and afterburn fireball. The gray shading in the histogram corresponds to

- the average background, and the black shading corresponds to the DNs of the event. The threshold levels are indicated with a dashed line.....46
19. The MWIR area profile of Bronze Scorpio event 26 is relatively independent of the threshold level. Changing the threshold from 20% of the dynamic range through 90% changes only the magnitude of the area, but not its shape as a function of time. The scaling factors,  $S$ , for each threshold level,  $th$ , are indicated below the plots.....47
20. The five area profiles are plotted for a Bronze Scorpio event in the red band. Threshold area (solid dark line) is several orders of magnitude below the maximum static (dotted dark like) and maximum dynamic (dotted gray line) areas. The three sigma static profile (dashed dark line) predicts the largest area, but the three sigma dynamic area (dashed gray line) has a much lower magnitude. ....49
21. Threshold area profile as a function time for a Bronze Scorpio detonation in the red band. The features that may be extracted from the profile are indicated.....50
22. The area profiles for all erect 155mm TNT detonations are shown (thin line) with their mean (thick line) and standard deviation (shaded region) in the upper plot. The  $C_V$  as a function of time for the area profiles is shown on bottom. The mean  $C_V$  value for the six events of this type's feature is 1.22.....64
23. The area profiles for all TNT detonations are shown (thin line) with their mean (thick line) and standard deviation (shaded region) in the upper plot.

- The  $C_V$  as a function of time for the area profiles is shown on bottom. The mean  $C_V$  value for the thirteen events of this type's feature is 1.6. ....65
24. The area profiles for all Composition B detonations are shown (thin line) with their mean (thick line) and standard deviation (shaded region) in the upper plot. The  $C_V$  as a function of time for the area profiles is shown on bottom. The mean  $C_V$  value for the five events of this type's feature is 1.58.....66
25. The area profiles for all TNT and Composition B detonations are shown (thin line) with their mean (thick line) and standard deviation (shaded region) in the upper plot. The  $C_V$  as a function of time for the area profiles is shown on bottom. The mean  $C_V$  value for the eighteen events of this type's feature is 1.98. ....67
26. The time to the peak detonation area in the red band is shown for each event (thin bars) of the eleven munitions groups. The mean feature value is also shown for each group (wide bars) and the value is indicated below the top plot. The bottom plot shows the coefficient of variation for the feature in each group.  $t_{det}^{red}$  is a very reproducible feature for all groups, indicating it may be a feature common to explosives in general. ....70
27. The peak detonation area in the blue band is shown for each event of the eleven munitions groups (thin bars). The mean feature value is also shown for each group (wide bars) and the value is indicated below the top plot. The bottom plot shows the coefficient of variation for the feature in

- each group. For TNT,  $A_{det}^{blue}$  shows correlation for a single weight and may be a good feature for classification. ....70
28. The time required for the fireball's area to fall below the noise level in the NIR is shown for each event of the eleven munitions groups (thin bars). The mean feature value is also shown for each group (wide bars) and the value is indicated below the top plot. The bottom plot shows the coefficient of variation for the feature in each group. ....72
29. The time required for the fireball's area to fall below the noise level in the MWIR is shown for each event of the eleven munitions groups (thin bars). The mean feature value is also shown for each group (wide bars) and the value is indicated below the top plot. The bottom plot shows the coefficient of variation for the feature in each group. ....72
30. Position of the shockfront (•) is shown with its uncertainty for an erect 155mm TNT detonation. The shock fit (solid line), modified shock fit (dashed line), and shock 350 fit (dotted line) are also shown. The functions were fit to the early-time data (lower left) with the late-time data point used to evaluate the fits in the far-field (upper right). ....74
31. Position of the shockfront (•) is shown with its uncertainty for an erect 155mm TNT detonation. The drag fit (solid line), modified drag fit (dashed line), and drag 350 fit (dotted line) are also shown. The functions were fit to the early-time data (lower left) with the late-time data point used to evaluate the fits in the far-field (upper right). ....75



32. The coefficient of determination calculated from the near, mid, and early far-field shockwave positions, is shown for each fit function and all events (top). The deviation of the fit from the far-field data point is also shown (below). All of the fits show good correlation in early-time data, but in the far-field the shock 350 and drag 350 models show the best agreement with observations. ....77
33. The speed of sound fit parameter for the modified drag (dark bars) and modified shock (light bars) fit functions are plotted for each event of each type in the upper plot. The shaded region was the average range of speeds of sound (based on the temperature) for the Bronze Scorpio field tests. On the lower plot, the Coefficients of Variation are plotted for the fit parameter by type. The modified drag best-fit speed of sound was consistently high whereas the modified shock best-fit speed of sound was consistently low. ....78
34. The characteristic radius from the drag 350 fit function is shown for each event of the eleven munitions groups (thin bars). The mean feature value is also shown for each group (wide bars) and the value is indicated below the top plot. The bottom plot shows the coefficient of variation for the feature in each group. The reproducibility of  $a^{drag350}$  for munitions types indicates that it is representative of a feature of the munitions, and perhaps will be useful in classification.....81
35. The time exponent fit parameter from the explosive fit function is shown for each event of the eleven munitions groups (thin bars). The mean

- feature value is also shown for each group (wide bars) and the value is indicated below the top plot. The bottom plot shows the coefficient of variation for the feature in each group. This feature is very reproducible for all groups yet increases for multiple munitions groups, indicating potential for classification.....82
36. The mean Mach number as a function of time (solid line) with the corresponding standard deviation (shaded region) for the modified drag fit to the shockwave is shown in the upper plot for all TNT and Composition B events The lower plot shows the coefficient of variation for each time step.....85
37. The mean shock pressure as a function of time (solid line) with the corresponding standard deviation (shaded region) for the modified drag fit to the shockwave is shown in the upper plot for all TNT and Composition B events The lower plot shows the coefficient of variation for each time step.....85
38. The mean detonation energy predicted at each time step (solid line) with the corresponding standard deviation (shaded region) for the modified drag fit to the shockwave is shown in the upper plot for all TNT and Composition B events The lower plot shows the coefficient of variation for each time step.....86
39. The time required for the area to fall to the noise level (in the NIR) is plotted for all detonations (○) DTSS plumes (Δ) and muzzle flashes (□). The upper plot shows the data points assuming normal distributions

- (detonations are represented by the solid line, plumes by the dotted line, and muzzle flashes by the dashed line). The lower plot represents the probability that a given time will be one of the three combustion classes, based on the normal distributions. Those events whose group has a higher probability are classified correctly (•) and those whose group has a lower probability are classified incorrectly (x).....88
40. The peak area (in the NIR) is plotted for all detonations (○) DTSS plumes (Δ) and muzzle flashes (□). The upper plot shows the data points assuming normal distributions (detonations are represented by the solid line, plumes by the dotted line, and muzzle flashes by the dashed line). The lower plot represents the probability that a given area will be one of the three combustion classes, based on the normal distributions. Those events whose group has the highest probability are classified correctly (•) and those whose group has a lower probability are classified incorrectly (x).....89
41. The peak area (in the NIR) is plotted for all conventional (○) novel (Δ) and novel FMJ (□) muzzle flashes. The upper plot shows the data points assuming normal distributions (conventional are represented by the solid line, novel by the dotted line, and novel FMJ by the dashed line). The lower plot represents the probability that a given area will be one of the three muzzle flash types, based on the normal distributions. Those events whose group has the highest probability are classified correctly (•) and those whose group has a lower probability are classified incorrectly (x).....91

42. The efficiency of detonation at 14.8 msec (from the modified drag model) is plotted for all 105mm TNT (○) and Composition B (Δ) detonations. The upper plot shows the data points assuming normal distributions, where 105mm TNT is represented by the solid line and Composition B by the dotted line. The lower plot represents the probability that a given efficiency will be one munitions group or the other, based on the normal distributions. Those events whose group has a higher probability are classified correctly (•) and those whose group has a lower probability are classified incorrectly (x). The *FR* is 103.....94
43. The energy of detonation at 14.8 msec (from the modified drag model) is plotted for all 105mm TNT (○) and Composition B (Δ) detonations. The upper plot shows the data points assuming normal distributions, where 105mm TNT is represented by the solid line and Composition B by the dotted line. The lower plot represents the probability that a given efficiency will be one munitions group or the other, based on the normal distributions. Those events whose group has a higher probability are classified correctly (•) and those whose group has a lower probability are classified incorrectly (x). The *FR* is 1.8314.....95
44. The time to the peak fireball area (in the green band) is plotted for all TNT (○) and Composition B (Δ) detonations. The upper plot shows the data points assuming normal distributions, where TNT is represented by the solid line and Composition B by the dotted line. The lower plot represents the probability that a given time will be one munitions group or the other,

- based on the normal distributions. Those events whose group has a higher probability are classified correctly (•) and those whose group has a lower probability are classified incorrectly (x). The *FR* is 2.28. ....96
45. The detonation area (in the red band) is plotted for all 155mm TNT (○) and 105mm TNT (Δ) detonations. The upper plot shows the data points assuming normal distributions, where 155mm TNT is represented by the solid line and 105mm TNT by the dotted line. The lower plot represents the probability that a given area will be one weight or the other, based on the normal distributions. Those events whose group has a higher probability are classified correctly (•) and those whose group has a lower probability are classified incorrectly (x). The *FR* is 5.25. ....97
46. Detonation efficiency is plotted against the afterburn and detonation energies in the upper plots, heat of detonation (which follows the same correlation as the specific afterburn energy) initial mass in the lower plots. As all quantities increase, the efficiency decreases. ....101
47. The highest non-efficiency correlations are shown for each munition characteristic. The Mach number tends to increase with mass and afterburn energy, although correlation is poor. The decrease in Mach number with detonation energy is due to the use of the drag model outside of its intended field and is not physically accurate. The time to the peak fireball area increases with the third power of the heat of detonation, neglecting the outliers. ....103

48. The highest non-efficiency correlations are shown for each TNT and Composition B characteristic. The Mach number tends to increase with mass and afterburn energy, although correlation is poor. The decrease in Mach number with detonation energy is due to the use of the drag model outside of its intended field and is not physically accurate. The time to the peak fireball area increases with the third power of the heat of detonation, neglecting the outliers. In all cases, correlation is higher than when C-4 was included.....105
49. Efficiency is plotted against the two masses of TNT and the correlation is shown. Because there were only two weights of TNT, this plot indicate separation of the data more than correlation. However, the trend is apparent and can be used as a scaling rule of thumb. ....107
50. Selected comparisons of fireball and shockwave features are shown for detonations of all munitions. In general, the fireball and shockwave features have a greater degree of correlation with each other than with munitions characteristics, as indicated by the higher coefficients of determination. The trends in the data are also fairly evident.....111
51. Selected comparisons of fireball and shockwave features are shown for detonations of TNT and Composition B munitions. The degree of correlation is not significantly affected by excluding C-4, indicating that the relationship between the fireball and shockwave is explosive composition independent. ....112

52. Selected comparisons of fireball and shockwave features are shown for TNT detonations only. The correlation between the features is the highest when only a single explosive composition is used and there are very clear trends.....113

## List of Tables

Table	Page
1. Selected properties of TNT isomer 2-4-6 [18].....	13
2. Selected properties of RDX [18].....	14
3. Test matrix for Bronze Scorpio. Data collected and examined are denoted by a “Y”; data that have yet to be acquired by AFIT (not examined) are denoted by an “X”.....	34
4. Test matrix for Muzzle Flash Tests indicating ammunition type, number of rounds fired, and number of rounds acquired with the Indigo imager.....	38
5. Threshold DN for each instrument used in the three field tests. In the Muzzle Flash test, there were two thresholds. The first measured everything above background and was variable for each event. It was set where the background DN spike drop below 1% of its maximum value, typically around DN 600. The second threshold quantized only the DNs of the bright flash and was fixed.....	46
6. Features extracted from the afterburn fireball in each band, denoted by an “x”.....	51
7. Material properties are shown for each munition in the Bronze Scorpio tests. These, along with the assumed atmospheric properties (also shown), allowed the near- and far-field radii to be calculated. ....	52
8. Types used in analysis. “Y” indicates use as a stand-alone type, “X” indicated that the type was not analyzed separately but was used in groups with other types, and “N” indicates no analysis was performed on the type.....	59



9.	Grouping of types for reproducibility, distinguishability, and correlation analysis.....	59
10.	The groups to be compared using the Fisher Ratio are shown for each set of comparisons. These include comparing groups of all combustion events, groups of muzzle flashes only, and groups of munitions detonations only.....	61
11.	The most reproducible fireball features and the corresponding Coefficients of Variation are given for each group of combustion events.....	68
12.	The most reproducible shockwave fit parameters and the corresponding Coefficients of Variation are given for each group of munitions. ....	80
13.	The most reproducible shockwave features in the near-and mid-fields ( $0 \leq t \leq 30$ msec) and the corresponding Coefficients of Variation are given for each group of munitions. The time in milliseconds where the $C_V$ was a minimum for the feature is indicated.....	83
14.	The Fisher Ratios for all features used in comparing detonations, DTSS plumes, and muzzle flashes are shown for each combination of combustion event classes.....	87
15.	The Fisher Ratios for all features used in comparing muzzle flashes are shown for each combination of ammunition types.....	90
16.	Fisher Ratios for highly reproducible fireball and shockwave features are shown for comparisons of explosive type (TNT and Composition B) and weight (155mm and 105mm TNT).....	92

17. The highest Fisher Ratios for each comparison are shown. Only a single physical quantity of each model is shown because they are all transformations of the same data. When multiple bands or models had similar values, the one with the largest FR is given and indicated by \*. For time-dependent features, the time is given in milliseconds.....94
18. The coefficient of determination,  $r^2$ , is shown for the features of the shockwave (highest 10) and fireball (highest 4) that are most highly correlated with all of the munitions' afterburn energy, detonation energy, specific energy released in the afterburn, heat of detonation, and mass.  $H_A$  and  $H_D$  were found to be redundant and are shown together.....99
19. The markers used to designate munitions type in Figure 46 through Figure 52 are shown below. All types containing C-4 are designated with the same marker because these types were not independently examined.....100
20. The coefficient of determination,  $r^2$ , is shown for the features of the shockwave (highest 10) and fireball (highest 4) that are most highly correlated with all of the TNT and Composition B munitions' afterburn energy, detonation energy, specific energy released in the afterburn, heat of detonation, and mass.  $H_A$  and  $H_D$  were found to be redundant and are shown together.....104
21. The coefficient of determination,  $r^2$ , is shown for the features of the shockwave (highest 10) and fireball (highest 4) that are most highly correlated with all of the TNT munitions' afterburn energy, detonation

	energy, specific energy released in the afterburn, heat of detonation, and mass.....	106
22.	The shockwave and fireball features that showed a moderate or greater degree of correlation with munitions characteristics are shown. The typical range of $r^2$ values are given, with all munitions representing the lower end and TNT representing the upper. The trend indicates how the feature behaves with increases in the munitions characteristic. ....	108
23.	For each fireball feature, the most correlated shockwave feature from each group (all munitions, TNT and Composition B, and TNT) is shown. The time at which temporal features were evaluated is indicated in milliseconds. ....	109
24.	The Phantom camera's resolution, full field of view, integration time, and framerate are given for each detonation event in the Bronze Scorpio tests.....	129
25.	The Indigo imager's instantaneous field of view, focal length, and full field of view are given for each detonation event in the Bronze Scorpio tests. ....	130
26.	Munitions groups .....	132
27.	Drag model fit parameters and uncertainties. ....	132
28.	Modified drag model fit parameters and uncertainties. ....	133
29.	Drag350 model fit parameters and uncertainties. ....	133
30.	Explosive model fit parameters and uncertainties. ....	134
31.	Modified explosive model fit parameters and uncertainties. ....	134
32.	Explosive350 model fit parameters and uncertainties. ....	135

## List of Abbreviations and Symbols

$A$	.....	area
$A_{3\sigma}$	.....	statistical area with dynamic mean
$A_{3\sigma}^0$	.....	statistical area with static mean
$A_t$	.....	area integrated with respect to time
$A_{\max}$	.....	maximum area with dynamic mean
$A_{\max}^0$	.....	maximum area with static mean
$A_{\det}$	.....	peak area of detonation
$A_{pk}$	.....	peak area of combustion (fireball, plume, muzzle flash)
$A_{px}$	.....	area of event viewed per pixel
$A_{th}$	.....	threshold area
$A_{sat}$	.....	saturation (flash) area
$\beta$	.....	drag rate
$c_0$	.....	ambient speed of sound
$c_p$	.....	specific heat at constant pressure
$C_v$	.....	coefficient of variation
$c_v$	.....	specific heat at constant volume
$D$	.....	detonation velocity, shockwave velocity
$d$	.....	distance to target
DN	.....	digital number

$DN_{\max}$	.....	maximum digital number
$DN_{th}$	.....	threshold digital number
DTSS	.....	dual-thrust smokey SAM
$E_A$	.....	energy released in the afterburn fireball
$E_a$	.....	activation energy
$E_D$	.....	theoretical energy released in detonation
$E_D(t)$	.....	observed energy released in detonation as a function of time
$E_D _{t=}$	.....	observed energy released in detonation evaluated at the indicated time
FFOV	.....	full field of view
FMJ	.....	full metal jacketed
FN	.....	frame number
FR	.....	Fisher Ratio
$\gamma$	.....	ratio of specific heats, $c_p / c_v$
$\Delta H$	.....	heat of reaction, enthalpy of formation
$\Delta H_A$	.....	specific energy released in afterburn fireball
$\Delta H_C$	.....	heat of combustion
$\Delta H_D$	.....	heat of detonation, specific energy released in detonation
IFOV	.....	instantaneous field of view
InGaAs	.....	Indium Gallium Arsenide
InSb	.....	Indium Antimonide
IR	.....	infrared

LWIR .....	long-wave infrared
$M$ .....	shockwave mach number
$m$ .....	mass
MWIR .....	mid-wave infrared
$N$ .....	total number of pixels
$N_i$ .....	number of pixels at $i$ th digital number
$n$ .....	number of values in feature set
NIR .....	near-infrared
$p_0$ .....	initial pressure, ambient pressure
$p_1$ .....	final pressure, shock pressure
$R$ .....	shockwave radius, shockwave position
$R_{\max}$ .....	maximum shockwave radius
$r$ .....	correlation coefficient
$r^2$ .....	coefficient of determination
$\overline{r^2}$ .....	mean coefficient of determination
RDX .....	Cyclotrimethylenetrinitramine
RGB .....	red, green, and blue
$\rho$ .....	density
$s$ .....	scaled distance
SAM .....	surface-to-air missile
$\sigma_x, \sigma_y$ .....	standard deviation of feature set
$\sigma_x^2, \sigma_y^2$ .....	variance of feature set

$T$	.....	temperature
$t$	.....	time
$t_{10}$	.....	time at which area falls below 10% of its peak
$t_{50}$	.....	time at which area falls below 50% of its peak value
$t_{det}$	.....	time at which the detonation area peaks
$t_n$	.....	time at which area falls to the noise level
$t_{pk}$	.....	time at which the combustion area peaks
TNT	.....	Trinitrotoluene
$\theta_{px}$	.....	instantaneous field of view of instrument (pixel)
$V$	.....	volume
$X, Y$	.....	feature set
$\bar{X}, \bar{Y}$	.....	mean of feature set
$x_i, y_i$	.....	ith value in feature set
$\xi$	.....	reaction coordinate
$\xi_0$	.....	numerical constant

## List of Subscripts, Superscripts, and Suffixes

0	.....initial condition/state
1	.....final condition/state
<i>blue</i>	.....blue band
<i>CompB</i>	.....Composition B
<i>drag</i>	.....drag model
<i>exp</i>	.....explosive/shock model
<i>drag 350</i>	.....drag 350 model
<i>exp350</i>	.....explosive/shock 350 model
<i>green</i>	.....green band
<i>mdrag</i>	.....modified drag model
<i>mexp</i>	.....modified explosive/shock model
<i>MWIR</i>	.....mid-wave infrared band
<i>NIR</i>	.....near-infrared band
<i>RDX</i>	.....RDX
<i>red</i>	.....red band
<i>(t)</i>	.....function of time
$ _{t=}$	.....evaluated at the time indicated (in milliseconds)
<i>TNT</i>	.....TNT



# **REPRODUCIBILITY, DISTINGUISHABILITY, AND CORRELATION OF FIREBALL AND SHOCKWAVE DYNAMICS IN EXPLOSIVE MUNITIONS DETONATIONS**

## **I. Introduction**

### **Background**

The ability to remotely monitor and classify high explosive events that occur around the world can be essential to the vital interests of the United States of America. Furthermore the ability to distinguish between legitimate uses of high explosives (mining, demolitions, construction, etc.) and the testing of enhanced or improvised weapons may avert subsequent events with cataclysmic outcomes. Current technology allows optical information from such events to be captured, but not enough is known about the underlying physics of these events for the data obtained to allow discernment of exactly what has occurred. Optical remote sensing is a growing field, but much work remains to be done before identifying specific events based on the interpretation of the optical data collected from remote sensing instruments is practical.

Optical remote sensing is the use of instruments or sensors to obtain the spectral and spatial characteristics of target objects from a distance. It is used extensively for the monitoring of static scenes such as crop growth, geological surveys, and urban patterns [1][2][3], as well as faster transient events like forest fires [4][5]. Its range of use has been from monitoring terrestrial events like the Kuwaiti oil fires [6][7] to collecting data

on extraterrestrial bodies light years away [8].

Remote sensing has also been used in military applications, for example, in detecting missile launches [9][10], gun muzzle flashes [11][12] and explosive detonations [13]. It is becoming increasingly important, however, not only to detect certain types of events, but also to distinguish them – specifically high explosives. The ability to distinguish a high explosives detonation from small arms fire or a missile plume, or to take the classification a step further and allow munitions types to be uniquely identified would give the war fighter a distinct tactical advantage.

### **Problem Statement**

Currently, the ability to identify munitions types based on the remote sensing of detonations is limited. While munitions may be distinguished with high confidence, this is only true when enough *a priori* information is known [14]. The extent of *a priori* information may be as minimal as knowing whether the munition was statically detonated or air dropped, or it may be as specific as knowing the weight and casing. As the understanding of detonations improves, however, superior classification features can be chosen, and the extent of *a priori* information needed to classify the munitions type will decrease.

Unfortunately, data collected from remote sensors result in hundreds of features that may or may not correlate specifically with the type of event taking place or with the specific explosive used. In order to choose the best features to classify munitions types, it is important to understand how the features obtained from observation relate to particular explosives. This can only be accomplished by developing phenomenological

relationships between the characteristics of the munitions (weight, casing, explosive compound, etc.) and the detonation effects it produces, specifically the shockwave immediately following detonation and the lingering afterburn fireball. In essence, a phenomenological model of detonations is needed with identifiable specific correlatable features that can be used to classify subsequent events.

### **Research Focus**

High explosive detonations generate two major phenomena of interest; a shockwave and an afterburn fireball. Identifying unique, correlatable signatures that relate the detonation event to a classable munition is highly desirable. There is an abundance of literature regarding the phenomenology of shockwaves for detonation events [15][16][17]. This literature describes the pressure, velocity, energy, and extent of shockwaves resulting from the initial detonation of an explosive material, which can be difficult (but not impossible) to monitor optically. Furthermore, the detonation of an explosive spans only a couple of milliseconds, making it difficult to identify; and acquiring a temporal profile of the emissions is even more challenging. For practical sensing of explosive detonations from aerial or spaced based platforms, it is the fireball resulting from the afterburn (mixing of unburned reactants with atmospheric oxygen resulting in explosive combustion) that is most easily monitored. The intense portion of the afterburn spans hundreds of milliseconds, with the cooling fireball lingering for seconds.

Thus improvements to the classification problem rely on understanding fireball phenomenology, and while the aforementioned understanding of detonation shocks

exists, there is little understanding of the relationship between the initial characteristics of the explosive and the resulting afterburn. There is much to be learned about these relationships, including how the initial conditions affect the afterburn's temperature distribution, turbulent flow, emissivity, size, etc. It will be the properties that are most easily remotely monitored, however, that may prove the most useful to the classification problem, and the simplest properties that will provide for general understanding of phenomenology. To this end, observations of fireball size as a function of time are an ideal starting point – it is easily remotely observed and should have a direct relationship to the characteristics of the munition type.

Additionally, because the shockwave resulting from a detonation of high explosives is well understood and can be monitored optically, determining a phenomenological relation between physical features that can be extracted from it (velocity, pressure, etc.) and the explosive material characteristics should also be possible. Furthermore, there is no clear connection between the characteristic features of the shockwave and the behavior of the afterburn fireball. Examination of the relationships between the shockwave and the fireball provides a great deal of insight into the phenomenology of explosive munitions detonations and was a major focus of this research.

### **Investigative Questions**

Because detonation physics encompasses a wide range of subjects (the more prominent fields including combustion chemistry, fluid flow, thermodynamics, and spectral radiometry), it was necessary to narrow down the list of subjects that were

investigated by determining what specific questions needed to be answered. These were:

1. Which features are reproducible for munitions of the same type, yet different for munitions of dissimilar types?
2. Which features of the shockwave and fireball are highly correlated with characteristics of the explosive material?
3. How are features of the shockwave related to features of the afterburn fireball?

The first question was important because the development of a phenomenological understanding of detonations requires that the observations of the fireball and shockwave be reproducible. Furthermore, for the understanding to be more than a characterization of detonations in general there must be a noticeable difference in the fireball or shockwave as the characteristics of the munitions change; i.e. features must be distinguishable. Answering this question also served the practical purpose of aiding in the classification problem, since classification of remotely sensed explosive detonations requires distinct, reproducible signatures.

This led to the second question to be answered in this work. By identifying which features are affected by changes in the explosive munitions' characteristics, it was possible to physically relate these features to those characteristics.

The final question answered was the major focus of this research. While the fireball and shockwave resulting from explosive detonations were seemingly independent of each other – the shockwave was supersonic ahead of the fireball and thus should not be influenced by it – identifying which features were correlated helped to understand the phenomenology of the features. High correlation between a feature of the shockwave and

one of the fireball indicated an underlying characteristic of the explosive material. Having been found, they may be used as predictors of fireball and shockwave features. Or, working the problem from the other end, classification may be accomplished by relating observation of shockwave and fireball features to the originating explosive material.

## **Methodology**

This research was not approached from a purely theoretical standpoint; i.e. the phenomenology was not developed from first principles. Rather, experimental observations of explosive munitions detonations – and other combustion events (muzzle flashes, missile plumes) for variety of data – were examined in several spectral bands. Features of the fireball and the shockwave were extracted for the detonation events. The majority of these features were physical in nature (i.e. the size of the fireball and the velocity of the shockwave), which served to aid in developing phenomenological relationships between the features and the explosive's characteristics, as well as between the features themselves. Other features, however, were extracted by fitting observed data to theoretical models and using the fit parameters as features.

The extracted features of the fireball and shockwave were assessed in a number of ways. They were examined for reproducibility for explosives of a single type, distinguishability for explosives of different types, and correlation with features of the explosive and other extracted features. All of the features for all of the munitions types were compared in a *brute force* manner by iterating through several groups of munitions to determine reproducibility and all possible combinations of two features to determine

both their correlation and their ability to differentiate munitions types. Evaluation was based on the use of several statistical metrics.

### **Assumptions/Limitations**

Due to the complexity of the problem, this research did not attempt to study the in-depth, detailed mechanics of shockwaves and fireball dynamics. Instead, it looked at the first-order problem by treating the explosive material, detonation, shockwave, and fireball using a simple model methodology. This meant using basic models of detonations. For the purpose of extracting and comparing features, this approach proved beneficial since the simple models capture the most important characteristics of explosive detonations. Although more complicated models exist, they only add refinements that contribute to a lesser extent.

The classification problem is as complex of a topic as understanding detonation phenomenology. For the practical classification of munitions detonations, robust classifications schemes, such as those outlined by Major Andy Dills in his PhD dissertation, *Classification of battle space detonations from temporally-resolved multi-band imagery and mid-infrared spectra*, are necessary [14]. Such methods were not used here. Rather, the separability of features was determined as a simplistic measure of their classification potential. Those with high potential may be examined in further research to determine their true utility.

Further, the results that are presented here were obtained using a limited set of data. There were three explosive compositions, only two of which were studied in-depth. There were also only two weights for each composition. In addition, there was not a

statistically meaningful sampling for many of the features examined. Thus, the conclusions that are drawn are limited to the explosives and weights examined and should be verified with a greater number of tests before they are accepted as truth.

### **Implications**

Finding the correlation between shockwave features, fireball features, and characteristics of the explosive munitions served two purposes. First, it furthered the phenomenological understanding of explosive detonations. A great deal is known about shockwave physics, but little is known about a detonation's afterburn fireball or the shockwave's relation to it. By studying these relations, a more complete picture of detonations was formed, which allowed scaling relations to be developed, laying the foundation for more complete theories and predictive models to be developed.

The second (and perhaps more practical) purpose of studying shockwave, fireball, and explosive material correlation was in supporting the classification effort. Although this research's focus was on developing a theoretical understanding of explosive detonation behavior, it also serves the interests of the Air Force and ultimately the war fighter.



## II. Theory

### Chapter Overview

Conventional explosive munitions release large amounts of energy in a very short time through the oxidation of an explosive fuel. The result is a high speed, high pressure shockwave immediately following detonation, as well as an afterburn fireball as the reactants continue to burn over a longer timeframe. In military applications, the shockwave is the primary means of affecting the target and is engineered so that it contains a great deal of energy, but the ongoing combustion of reactants in the fireball also releases a significant amount of energy.

The first three sections of this chapter give a brief overview of combustion reactions and the explosives used in this research (TNT, RDX, and Composition B) as detailed in *Explosives* by Josef Köhler [18] and *Explosives Engineering* by Paul Cooper [19]. The latter sections address the basic theory of detonations in explosive materials and shockwave propagation. General information on these topics was drawn from *Detonation* by Fickett and Davis [17], *Physics of Shock Waves and High-Temperature Hydrodynamic Phenomena* by Zel'dovich and Raizer [15], and the Army Materiel Command's *Engineering Design Handbook. Principles of Explosive Behavior* [16]. Finally, the statistical metrics used in analyzing shockwave and fireball features are discussed.

### Combustion Chemistry

Conventional explosives are primarily composed of carbon, hydrogen, nitrogen, and oxygen in the form of a molecule,  $C_xH_yN_wO_z$ . When these compounds react, they

undergo a process known as oxidation in which the reactants are converted to products with lower internal energies. The excess energy is released exothermically and is known as the heat of combustion,  $\Delta H_C$ . Most conventional explosives are fairly stable in their latent form because they must overcome an energy barrier (called the activation energy),  $E_a$ , for the reaction to proceed (Figure 1).

The oxidation (burning) of explosives is a combustion reaction. While the process can be quite complex, the typical chemistry follows Equation 1, where  $a_1$ - $a_5$  are dependent on the constituents of the explosive molecule [19]. With the exception of CO, the final products shown are the highest oxidation states (lowest internal energies) for each atom, and thus the most stable. Ideally, when there is enough oxygen present, the

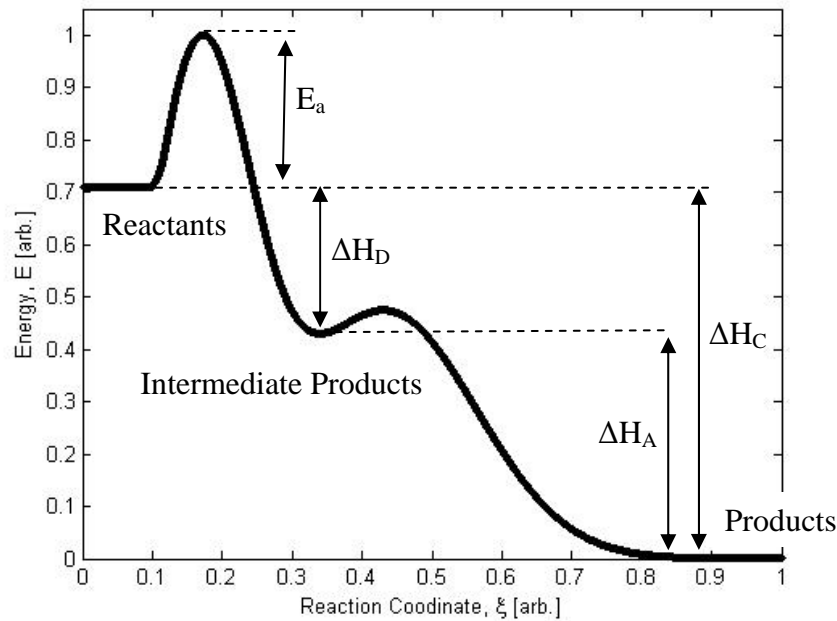
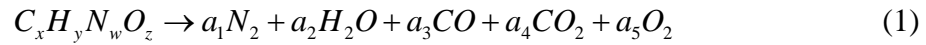


Figure 1: Internal energy is plotted as a function of reaction coordinate. As the reaction proceeds (left to right), the reactants overcome the activation energy,  $E_a$ , and are converted to products with a lower internal energy. The process is typically a two step process: detonation is where the reactants are converted to intermediate products with the oxygen present in the system, releasing some energy,  $\Delta H_D$ . As additional oxygen is introduced, the reaction continues and additional energy is released,  $\Delta H_A$ . The total excess energy released is known as the heat of combustion,  $\Delta H_C$ .

reactants burn completely and the energy release is the heat of combustion,  $\Delta H_C$ . This is the total amount of energy that can be released from the combustion of the molecule. Most conventional explosives are oxygen deficient and cannot fully oxidize without mixing with atmospheric oxygen. When this occurs, the products may not be the states of lowest energy for each atom, typically resulting in CO and NO<sub>x</sub>.



The amount of energy released from a detonation reaction with oxygen present in the molecule is the heat of detonation,  $\Delta H_D$ . The remaining energy,  $\Delta H_A$ , can be liberated by introducing additional oxygen into the system and allowing the reaction to proceed to the final product states. When an oxygen deficiency exists, there is a hierarchy of how the reactants burn to form products. These are summarized by Cooper [19] in the following rules of thumb that give a general guide for determining products:

1. all N combines to form N<sub>2</sub>
2. H<sub>2</sub> combines with O to form H<sub>2</sub>O
3. remaining O combines with C to form CO
4. remaining O combines with CO to form CO<sub>2</sub>
5. remaining O combines to form O<sub>2</sub>

In addition, there are always NO<sub>x</sub> molecules formed, but these account for less than 1% of all products. The above is known as the simple product hierarchy of CHNO explosives and models an ideal detonation. Non-ideal behavior includes unburned hydrocarbons as products, as well as unreacted pieces of explosive material being ejected from the detonation. This results in a lower than expected release of energy.

## TNT

Trinitrotoluene (TNT) is a well understood explosive that is important in military and commercial applications. It has a high inherent stability and the capacity to be combined with a wide variety of materials for fine-tuning its explosive characteristics. The molecular formula of TNT is  $C_7H_5N_3O_6$ , which includes several isomers. Military specifications are very stringent and allow only the symmetric 2-4-6 to be used (Figure 2). TNT for use in military applications is optimized for the greatest detonation energy, shockwave velocity, and overpressure. This requires a high density of the explosive material, and so military grade TNT is either cast (molten and then shaped) or pressed (mechanically compressed) to obtain higher densities. Some relevant properties of high density TNT are found in Table 1.

Pure TNT has a negative oxygen balance, indicating that it does not have enough oxygen present in molecular form to completely oxidize. An oxygen balance of -73.9% means there is an oxygen deficiency of 73.9% by weight, so that according to the CHNO rules given above, a TNT detonation will be of the form shown in Equation 2. Per

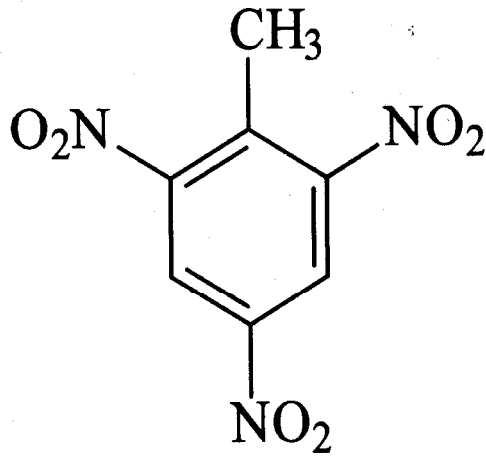


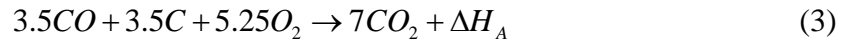
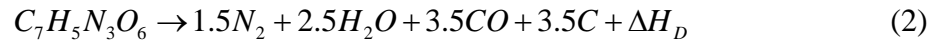
Figure 2: TNT molecular structure.

kilogram,  $\Delta H_D$  is approximately 4563 kJ of energy released in the initial detonation. As the products mix with atmospheric oxygen, combustion can occur to release additional energy as the carbon atoms and carbon monoxide molecules form the more stable  $\text{CO}_2$  molecule (Equation 3) [19]. Assuming complete oxidation of all reactants occurs, the additional release of energy in the afterburn fireball,  $\Delta H_A = \Delta H_C - \Delta H_D$ , was calculated to be approximately 10444 kJ/kg.

Table 1: Selected properties of TNT isomer 2-4-6 [18]

Molecular Weight (kg/mole)	0.2271
Oxygen Balance (%)	-73.9
Heat of Detonation, $\Delta H_D$ (kJ/kg)	4563
Heat of Combustion, $\Delta H_C$ (kJ/kg)	15007
Density, $\rho$ (kg/m <sup>3</sup> )	1654
Detonation Velocity*, $D$ (m/s)	6900

\* at  $\rho = 1600 \text{ kg/m}^3$



## RDX

Cyclotrimethylenetrinitramine (RDX) is a powerful explosive due to its high density and high detonation velocity. Like TNT, it is a very stable explosive. The molecular formula for RDX is  $\text{C}_3\text{H}_6\text{N}_6\text{O}_6$  (Figure 3). RDX, like TNT, has a negative oxygen balance. The detonation follows the reaction shown in Equation 4 [19]. In the initial detonation reaction 6322 kJ/kg of energy is released. The remaining energy, approximately 3825 kJ/kg, is released as the CO reacts with atmospheric oxygen to produce  $\text{CO}_2$ . This gives a greater initial release of energy than TNT, but the total release of energy per kilogram is lower. Some pertinent properties are shown in Table 2.

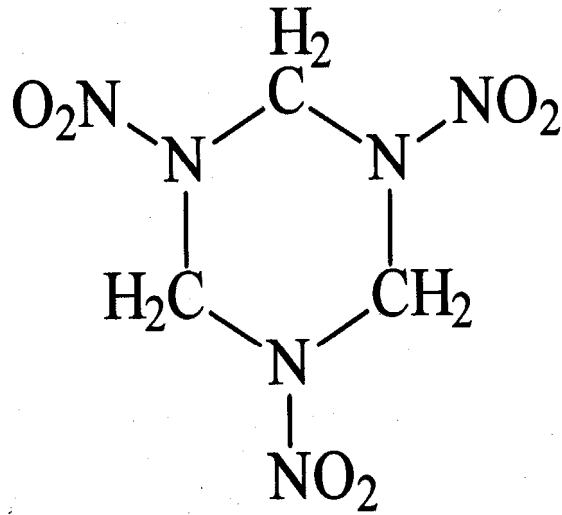
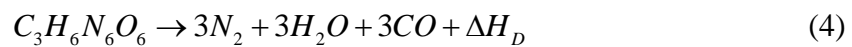


Figure 3: RDX molecular structure.

Table 2: Selected properties of RDX [18]

Molecular Weight (kg/mole)	0.2221
Oxygen Balance (%)	-21.6
Heat of Detonation, $\Delta H_D$ (kJ/kg)	6322
Heat of Combustion, $\Delta H_C$ (kJ/kg)	10147
Density, $\rho$ (kg/m <sup>3</sup> )	1820
Detonation Velocity*, $D$ (m/s)	8750

\* at  $\rho = 1760 \text{ kg/m}^3$



### Composition B

Composition B is an explosive compound cast from 59.5% RDX, 39.5% TNT, and 1% wax by weight and is used primarily in military applications. It has a density near that of TNT,  $\rho = 1650 \text{ kg/m}^3$ , although it may be raised to  $1700 \text{ kg/m}^3$  and higher with special casting techniques. Its detonation velocity is approximately  $7800 \text{ m/s}$  at a density of  $1650 \text{ kg/m}^3$  [18].

## Simple Theory of an Ideal Detonation

Detonations involve many complex phenomena including chemical kinetics, fluid dynamics, and thermodynamics. Even for relatively basic explosives in simple geometries, the mathematical treatment is quite difficult. To obtain a basic understanding of what happens in a detonation, a number of simplifying assumptions can be used, providing a first-order perspective. The assumptions generally used are as follows [19 pp 253-254]:

1. There is only flow in one dimension
2. The detonation front discontinuously jumps from high pressure behind the front to ambient pressure ahead of the front
3. Reactants and products are in a state of chemical and thermodynamic equilibrium
4. The chemical reaction zone is infinitely thin
5. The velocity of the detonation front is constant
6. The reaction products may be affected by the rest of the system or by boundary conditions after the detonation front has passed

When combustion is initiated in an explosive material, the burn front propagates outward, consuming reactants in the process. The reaction products in the wake of the front are in a gaseous state and very energetic due to the large amounts of energy liberated in the reaction, resulting in high pressures immediately behind the front. If the reaction front is propagating supersonically, there will be a discontinuous region between the high pressures behind the front and the unaffected material ahead of the front. This discontinuity is known as a shockfront, shockwave, or shock.

While inside the explosive, the shockwave is supported by the energy released in the reaction. Very shortly after the detonation is initiated, the shockwave velocity,  $D$ , reaches an equilibrium value. This velocity is maintained as the shock passes through the rest of the explosive before finally breaching the surface. The process, from the initiation of combustion to the shockwave proceeding through the explosive and breaching the surface, happens on such a short timescale that it is effectively instantaneous. The result is a nearly instantaneous release of energy as the shock breaches the surface,  $E_D$ . Once outside of the explosive, the energy driving the shock is no longer present and the shock dissipates.

### Shock Relations

Before describing the behavior of the shockwave's expansion outside of the explosive, it is helpful to describe some of the relations that it is assumed to obey (taken from assumptions used by Zel'dovich [15]). First, it is assumed that the atmosphere the shock is traveling in is a perfect gas, i.e. the initial (ambient) pressure,  $p_0$ , and final (shock) pressure,  $p_1$ , obey the Ideal Gas Law (Equation 5). It is also assumed that the atmosphere is homogeneous and has a constant specific heat (at constant pressure,  $c_P$ , and constant volume,  $c_V$ ) for all temperatures,  $T$ . The ratio of specific heats (Equation 6),  $\gamma$ , takes on values of  $5/3$ ,  $7/5$ , and  $9/7$  for monatomic, diatomic, and triatomic ideal gases, respectively.

$$\frac{p_0}{\rho_0 T_0} = \frac{p_1}{\rho_1 T_1} \quad (5)$$

$$\gamma = \frac{c_P}{c_V} \quad (6)$$



With these assumptions, the relationship in Equation 7 can be derived [20]. This relation gives the pressure of the shockwave (overpressure) as a function of the ratio of specific heats and the mach number of the shockwave,  $M$ . The mach number is defined as the speed of the shockwave divided by the speed of sound,  $c_0$ , in the medium in which the shock is propagating – the atmosphere in this case (which is almost entirely diatomic, establishing the value of  $\gamma$  to be 7/5). With this basic relationship between the pressures of the gases and the shock velocity established, it is possible to determine the characteristics of the shockwave at any point along its propagation path.

$$\frac{P_1}{P_0} = \frac{1}{\gamma + 1} [2\gamma M^2 - (\gamma - 1)] \quad (7)$$

### Shock Expansion

Propagation of the shockwave outside of the explosive material has a dampening effect on both its pressure and velocity because it is no longer supported by the reaction energy of the explosive. Its peak pressure and velocity are initially determined by the shock's properties as it leaves the explosive, but then decrease due to drag and geometry effects. Assuming the initial shock in the explosive is strong (very high overpressures), the resulting shockwave outside of the explosive material gradually decays to a weak shock and then finally to an acoustic wave [15 pp 100].

The exact form of the transition from shockwave to acoustic wave depends on the medium in which the shock is propagating. Continuing with the assumption of a homogenous atmosphere composed of perfect gases with constant specific heats, if a strong shock (which is most often the case in explosive munitions detonations) is expanding into it, a number of additional relations can be derived. These relations, given

by Zel'dovich, hold true independent of the functional form of the shock's expansion [15 pp 51-52].

Equation 8, states that the limiting value of the density of particles behind the front does not increase without limit as the shock's pressure increases, but rather approaches a finite value. Equation 9, shows that the velocity of the shockfront is proportional to the square-root of its overpressure. In both of these relations, the constant of proportionality is dependent on the ratio specific heats of the gas into which the shock is expanding.

$$\rho_1 < \frac{\gamma+1}{\gamma-1} \rho_0 \quad (8)$$

$$D = \left( \frac{\gamma+1}{2} \cdot \frac{p_1}{\rho_0} \right)^{1/2} \quad (9)$$

The above formulas provide relationships amongst the thermodynamic properties of the shockwave. Accurately relating these properties to the initial release of energy in the detonation, however, is accomplished using empirical observations with known detonation sources. Figure 4 shows the distance the shockwave has propagated from the origin of the detonation (scaled down by a factor of the cube root of the mass equivalent of TNT of the explosive material) as a function of overpressure in the shockwave. The data were obtained for vapor cloud explosions, but should be valid for munitions detonations because it relates the pressure in the shockwave to an initial energy release, using the same assumptions of an ideal point detonation [21].

If the overpressure,  $p_1$ , is found at a distance from the point of detonation,  $R$ , the scaled distance,  $s$ , can be used as a conversion factor to determine the equivalent mass of

TNT,  $m$ , that was detonated (TNT equivalent mass is a standard that is often used to describe an explosive's energy release). This is then easily converted to a detonation energy,  $E_D$ , using TNT's heat of TNT,  $\Delta H_D$ . The detonation energy is the amount of energy that would have had to have been instantaneously released in a detonation to generate a shock of a given pressure at a given distance. Based on descriptions provided in the *SFPE Handbook of Fire Protection Engineering* [21], the functional form was determined and is shown in Equation 10.

$$E_D = \left( \frac{R}{s(p_1)} \right)^3 \cdot \Delta H_D^{TNT} \quad (10)$$

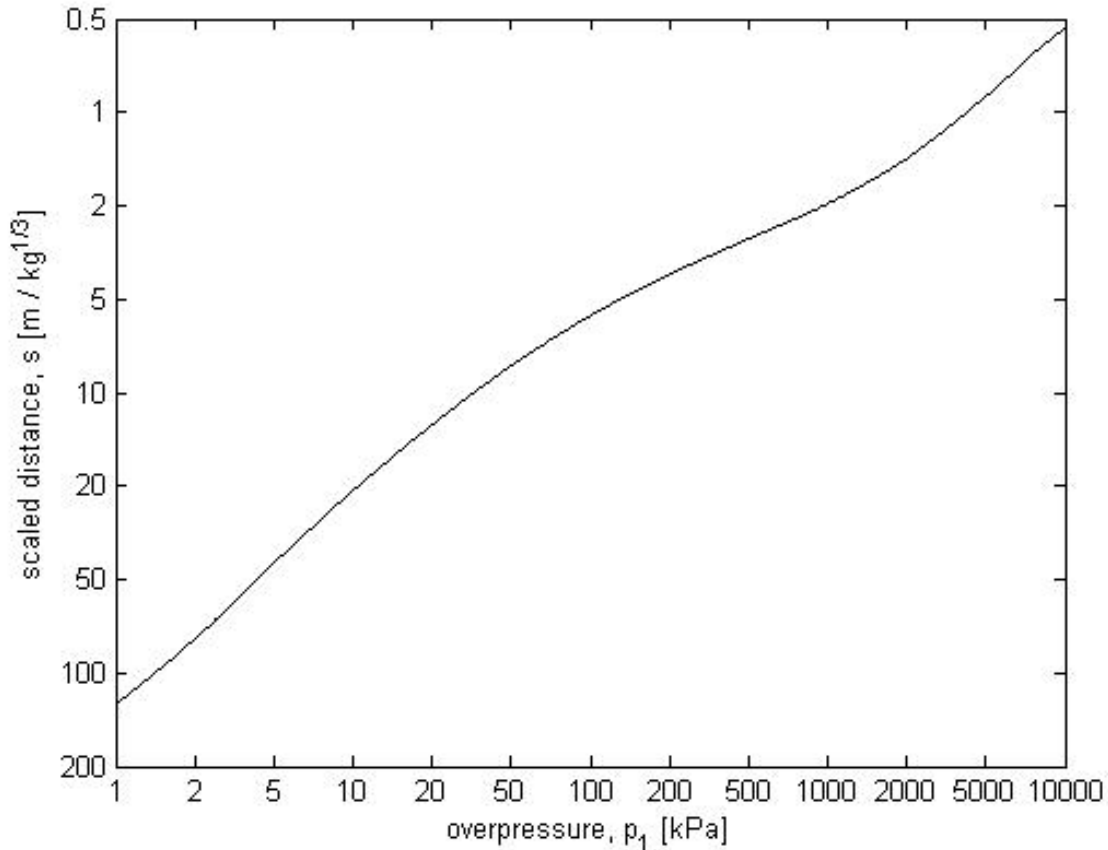


Figure 4: The scaled distance is plotted as a function of overpressure for a detonation shockwave.

## Explosive Model

There are two basic models in the literature that describe the radial evolution of the shockwave as a function of time. The first model, known as the explosive or shock model, was developed in 1966 by Zel'dovich and Raizer [15 pp 93-94] and is based on the following assumptions:

1. A large amount of energy,  $E_D$ , is released into a small volume nearly instantaneously
2. The shock expanding from the point release of energy has spherical symmetry (one-dimensional, radial)
3. The mass of the explosive,  $m_0$ , is negligible compared to the mass of gases encompassed by the shock,  $m_I$
4. The pressure of the shock,  $p_I$ , is much greater than ambient pressure,  $p_0$
5. Motion of the expanding gas is determined only by the energy released in the detonation,  $E_D$ , and the ambient atmospheric density,  $\rho_0$

The only combination of  $E_D$  and  $\rho_0$  that gives only units of distance and time is  $E_D / \rho_0$  which has dimensions of  $[m^5/s^2]$ . Accordingly, the radius of the shock,  $R$ , as a function of time,  $t$ , is given in Equation 11, where  $\xi_0$  is a unitless constant that depends on the ratio of specific heats,  $\gamma$ , given by Equation 12 [22]. Taking the derivate of  $R(t)$  with respect to time gives an expression for the detonation velocity,  $D(t)$ , as shown in Equation 13. In terms of the radius of the shockfront, the velocity is given in the form shown in Equation 14. It should be noted that although the form given here requires a time dependence of  $t^{0.4}$ , experimental work often finds more accurate fits in the range of  $t^{0.4}$  to  $t^{0.6}$  [24 pp 2733].

$$R(t) = \xi_0 \left( \frac{E_D t^2}{\rho_0} \right)^{1/5} \quad (11)$$

$$\xi_0 = \left( \frac{5}{2} \right)^{2/5} \left( \frac{3}{4\pi} \right)^{1/5} \left( \frac{\gamma+1}{2} \right)^{2/5} \quad (12)$$

$$D(t) = \frac{dR}{dt} = \xi_0 \frac{2}{5} \left( \frac{E_D}{\rho_0} \right)^{1/5} t^{-3/5} \quad (13)$$

$$D(R) = \frac{2}{5} \xi_0^{5/2} \left( \frac{E_D}{\rho_0} \right)^{1/2} R^{-3/2} \quad (14)$$

In the near-field the source mass is not negligible compared to the mass encompassed by the shockwave, which violates the third assumption. In the far-field, the shockwave's overpressure attenuates to near ambient pressure, violating the fourth assumption. Thus the equations given above are only valid in the mid-field. This is defined as the region satisfying Equations 15 and 16 [15 pp 94]. The second assumption, that the shock is spherical, allows the mass encompassed by the shock,  $m_1$ , to be defined as the volume of the sphere enclosed by the shock times the ambient air density,  $\rho_0$ . Combining these equations, along with Equations 8 and 9, allows the mid-field to be described by Equation 17.

$$m_0 \ll m_1 = \frac{4}{3} \pi R^3 \rho_0 \quad (15)$$

$$p_1 \gg \left( \frac{\gamma+1}{\gamma-1} \right) p_0 \quad (16)$$

$$\left( \frac{2}{5} \right)^{2/3} \xi_0^{5/3} \left[ \frac{2E_D(\gamma-1)}{\rho_0(\gamma+1)^2} \right]^{1/3} \gg R \gg \left( \frac{3m_0}{4\pi\rho_0} \right)^{1/3} \quad (17)$$

Beyond the mid-field, the overpressure approaches ambient pressure and the shock velocity approaches the speed of sound,  $c_0$ . This transition is gradual with the end resulting being a nearly spherical acoustic wave expanding according to Equation 18 [15 pp 99-100][23 pp 6131].

$$R(t) = c_0 t \quad (18)$$

### Drag Model

Also commonly used to model the expansion of an explosive shock is the drag model. This model treats the shockwave's expansion as being dampened in proportion to its velocity due to viscous forces. Equation 19 shows the differential equation governing this deceleration and Equation 20 shows its solution [24 pp 2733-2734].  $\beta$  is the drag rate,  $D$  is the velocity of the shock as a function of time,  $t$ , and  $D_0$  is the initial velocity of the shock immediately following detonation. Integrating the solution with respect to time and imposing the boundary condition that at detonation the radius must be zero, the radial extent,  $R$ , of the shock as a function of time is found (Equation 21).

$$\frac{dD}{dt} = -\beta D \quad (19)$$

$$D(t) = D_0 e^{-\beta t} \quad (20)$$

$$R(t) = \frac{D_0}{\beta} (1 - e^{-\beta t}) = R_{\max} (1 - e^{-\beta t}) \quad (21)$$

The drag model of shock expansion accurately models the shock's growth at early times while the mass of expanding product gases is greater than the mass of atmospheric gases displaced and the velocity is still considerable [24 pp 2743]. In this region the deceleration is also large, but gradually decreases as the radius of the shock

asymptotically approaches its maximum value,  $R_{max}$ . This is defined as the initial velocity divided by the drag coefficient and physically represents the distance at which the shock pressure reaches ambient pressure [25 pp 1557].

## Statistical Metrics

With the end goal of characterizing munitions detonations being classification, it is important to find features that are both reproducible within a munitions type yet distinguishable across munitions types. A simple way to evaluate how well a feature satisfies these requirements is to use the coefficient of variation and the Fisher Ratio. Both of these metrics are statistical and assess the set of values obtained for the given feature.

The coefficient of variation,  $C_V$ , is a measure of a set of values' variability about its mean. For a feature,  $X$ , it is defined as the standard deviation of the set of all values in the set,  $\sigma_x$ , divided by the mean of the feature set,  $\bar{X}$  (Equation 22). Because the standard deviation of the feature set is normalized by its mean,  $C_V$  allows the variability of features of any value to be directly compared. This metric assumes a normal distribution, which may or may not be accurate for all features it is used to examine. Because of its simplicity, however, it is often a valid metric for characterizing the dispersion of experimentally determined values. Figure 5 gives an idea of how variability in a data set translates to  $C_V$  values. Qualitatively,  $C_V$  values above 0.2 begin to show a great deal of variability, while those below 0.2 begin to appear reproducible.

$$C_V = \frac{\sigma_x}{\bar{X}} \quad (22)$$

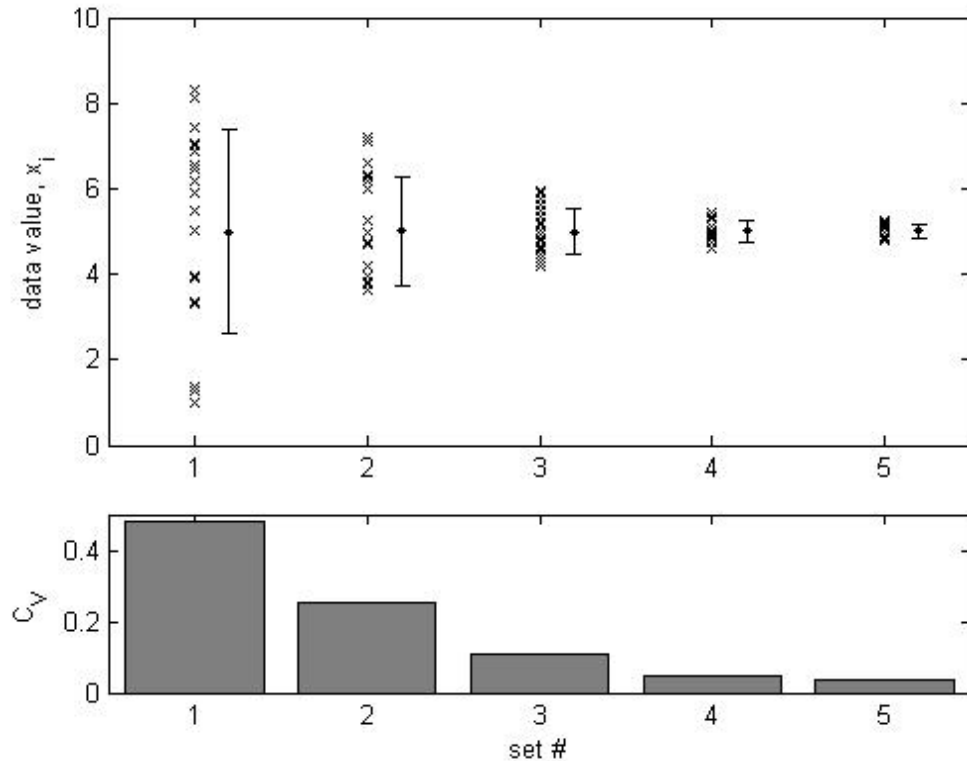


Figure 5: The distributions of values ( $x$ ) for five sets of data are shown in the upper plot. The mean ( $\bullet$ ) and standard deviation ( $I$ ) of each set is offset to the right of the data points. The lower plot shows the coefficient of variation for each set of data. A  $C_v$  value of  $\sim 0.5$  or greater indicates large variability of the data, whereas a value of  $\sim 0.1$  or less indicates decent reproducibility.

The Fisher Ratio,  $FR$ , is a measure of the separation of multiple sets of values.

While it may be used to characterize a number of sets, its form is simplest and most easily understood for only two sets,  $X$  and  $Y$ . Here, the Fisher Ratio is given as the square of the difference of the means of the sets,  $\bar{X}$  and  $\bar{Y}$ , divided by the sum of the variances of the sets,  $\sigma_x^2$  and  $\sigma_y^2$ , as shown in Equation 23. The meaning of the Fisher Ratio can be visualized with Figure 6. This figure assumes normal distributions – which is not always the case – making the relationship between the means and standard deviations of the two sets apparent. Separation of the sets can be thought of as depending on how much the distributions of the sets overlap, which for normal distributions depends on how



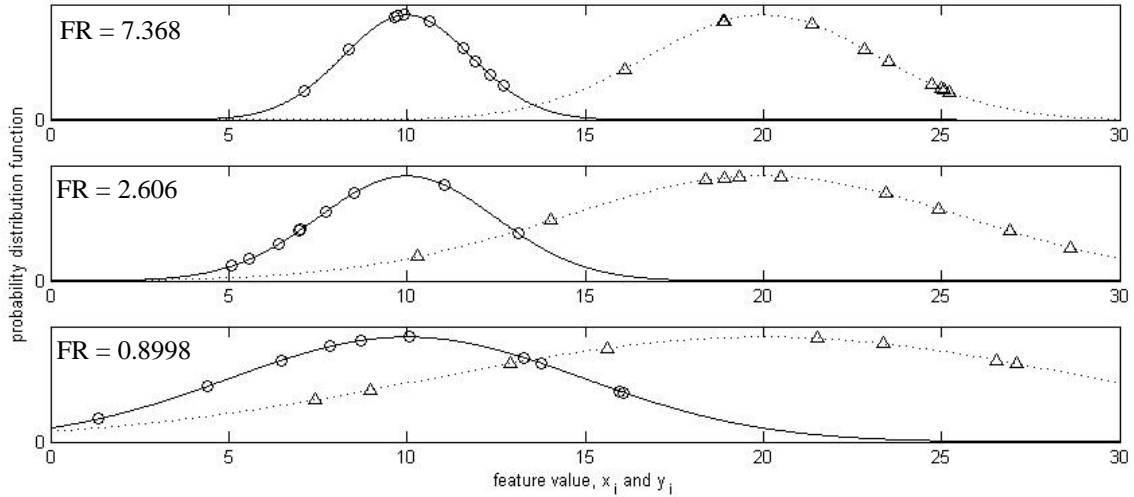


Figure 6: Two sets of Gaussian distributed data are shown. Data points from set one ( $\circ$ ) have a distribution represent by the solid line. Data points from set two ( $\Delta$ ) have a distribution represent by the dotted line. From top to bottom, the widths of the Gaussians (variability in the data sets) increase. The resulting overlap in the distributions causes a decrease in separability, as indicated by the lower Fisher Ratio. Decrease in the  $FR$  will also occur if the variability remains fixed but the means become closer together.

far apart the means of the set are (where the Gaussians are centered) and how reproducible the values are about their means (the width of the Gaussians). The more the distributions overlap, the less separated the data are.

$$FR = \frac{(\bar{X} - \bar{Y})^2}{\sigma_X^2 + \sigma_Y^2} \quad (23)$$

Another metric, the correlation coefficient,  $r$ , is a measure of how correlated two sets of data are, with one definition given by Equation 24 (where  $x_i$  and  $y_i$  are the  $i$ th values in  $X$  and  $Y$ , and  $n$  is the number of pairs in  $X$  and  $Y$ ). For complete correlation, i.e. a linear relationship,  $r = \pm 1$  (positive if both sets of data increase together or negative if one set increases while the other decreases). As the correlation between the sets decreases,  $r$  approaches zero. This is shown in Figure 7 for data with perfect correlation (upper left) through poor correlation (lower right). The magnitude of the correlation

between the two sets is measured by the square of the correlation coefficient and is called the coefficient of determination,  $r^2$ .

$$r = \frac{\sum_{i=1}^n x_i y_i - n\bar{X}\bar{Y}}{\sqrt{\left(\sum_{i=1}^n x_i^2 - n\bar{X}^2\right)\left(\sum_{i=1}^n y_i^2 - n\bar{Y}^2\right)}} \quad (24)$$

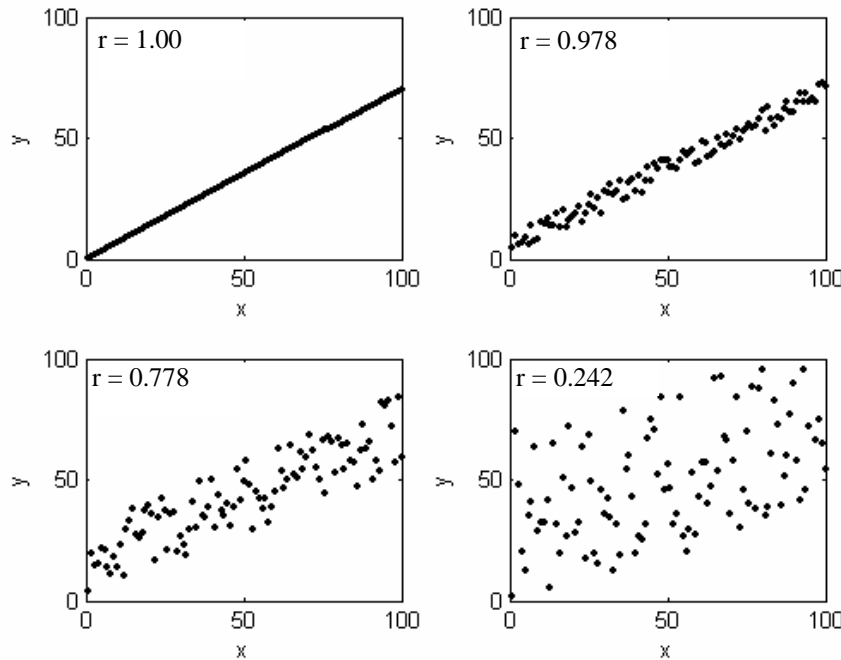


Figure 7: Correlation of two sets of data points, x and y, is shown. Complete correlation  $r = 1$  (upper left) through poor correlation (lower right) can be seen.

## Summary

Combustion chemistry and the ideal theory of detonation, while not capturing all of the intricacies of high explosive detonations, provide a background for understanding the primary results of detonations. These include a nearly instantaneous release of energy that is primarily in the form of a shockwave which – in the ideal model – expands

symmetrically in the radial direction. This shockwave gradually transitions to an acoustic wave as its pressure decreases to ambient pressure and its velocity to the speed of sound.

Energy also goes into visible and infrared emissions as the explosive reactants detonate. Because many munitions (TNT and Composition B in this research) are oxygen deficient, the reactants do not fully oxidize in the initial detonation. As these unburned reactants and detonation byproducts mix with atmospheric oxygen, the reaction continues, resulting in an afterburn fireball that lingers for hundreds of milliseconds to seconds after the initial detonation.

Features from the shockwave and afterburn fireball can be assessed for reproducibility, distinguishability, and correlation using a number of statistical metrics. This allows these properties of the features to be compared quantitatively for a more exact understanding of them.

### III. Methodology

#### Chapter Overview

The preceding theory applies to simple detonations under ideal conditions where flow is all one dimensional (in the radial direction), the explosive fuel is fully detonated (not necessarily to the lowest oxidation state, but to a state where no unreacted fuel remains), and the energy released due to the combustion of detonation byproducts in the afterburn fireball is neglected.

Detonation of real munitions rarely follows this idealized model. Often, the detonation is far from symmetric due to the geometry of the munitions, and even when geometry does allow for a spherical detonation, the resulting shockwave and afterburn will be influenced by turbulence and temperature gradients in an inhomogeneous atmosphere. Complicating the situation even further, the explosive detonation can throw out pieces of explosive material before it combusts, leading to secondary detonations or sustained combustion of the afterburn fireball.

Because of these effects, characteristics that are very reproducible in the lab become uncertain in the real world. Relatively simple munitions detonations can appear wildly different in different environments or – even more frustrating to the classification process – they can appear different under seemingly similar conditions. By determining which features are reproducible and distinguishable, it may be possible to model some of the basic phenomenology of detonation shocks and fireballs.

An attempt was made at accomplishing these goals by investigation a number of emission events, not just munitions detonations. While ultimately it is the features

extracted from detonation shockwaves and afterburn fireballs that are important, developing and verifying the techniques to extract useful features was also important. To this end, data from missile plumes and small arms muzzle flashes were examined in addition to munitions detonations. This established reproducibility of features and differentiation between dissimilar classes of combustion events. Once this was accomplished, distinguishing between types within a specific class of combustion events, i.e. bomb detonations, was attempted.

This chapter begins with an overview of the instrumentation and field tests used to collect the data. It discusses the methods used for processing data. Finally, this section concludes with a description of the metrics and models used to analyze the data.

## **Instrumentation**

Three instruments provided data that were examined in this research: a high speed visible Phantom camera, an Indigo Alpha near-infrared (NIR) imager, and an Iiris mid-wave infrared (MWIR) imager. The Canon imager was also used for documentation purposes. This section gives a basic description of each instrument, paraphrased from the *Bronze Scorpio Test Report* [26] and Major Andy Dill's PhD dissertation, *Classification of battle space detonations from temporally-resolved multi-band imagery and mid-infrared spectra* [14]. Additionally, any settings that affected data analysis are discussed. A detailed list of instruments settings used in this research for each field test is given in Appendix 1.

The tool of primary interest for examining detonation events was a high speed Phantom camera. The Phantom is a 24 bit Truecolor imager (8 bits in each of the red,

green, and blue bands) that can record up to 4,800 full frames per second, or exceeding 150,000 frames per second on smaller regions of the focal plane array (FPA). The FPA is an 800x600 SR-CMOS array with 22  $\mu\text{m}$  pixels. It integrates over propriety red, green, and blue (RGB) bandpasses with integration times adjustable from as low as 2  $\mu\text{s}$  to as long as  $\sim 95\%$  of the inverse of the frame-rate. The primary drawback of the Phantom camera is the long times required to download data from the camera; because of this, on average only every other detonation event was captured.

The Indigo Alpha NIR imager has an InGaAs FPA that integrates over the 0.9–1.7  $\mu\text{m}$  band with the relative spectral response shown in Figure 8. The FPA provides a resolution of 320x256 with 30  $\mu\text{m}$  pixels and 12 bit dynamic range. It was non-uniformity corrected using dark, medium, and bright sources in order to correct any offset and gain differences in the individual pixels. The imager frames at a maximum of 30 Hz but is often slower due to the duty cycle of the FPA (readout and data transfer time). This slow-down can be minimized by keeping the variable integration time low (in the hundreds of microseconds or less) and the total recording time less than is capable of being stored in the buffer (typically  $\sim 7$  seconds). For high intensity events, such as detonation events or missile plumes, this was not an issue. Measurement of the muzzle flashes required long integration times (33 milliseconds) to ensure that the short-lived flash (less than 2 milliseconds) was acquired. Although this slowed the frame-rate to 11~15 Hz, it provided the best fraction of captured muzzle flashes to rounds fired.

The Cincinnati Electronics IRRIS MWIR imager collects thermal imagery in the 3–5  $\mu\text{m}$  band with a 256x256 InSb FPA. It has a spatial resolution and dynamic range that is equivalent to the Indigo NIR imager: 30  $\mu\text{m}$  pixels that bin data into 12 bits. It

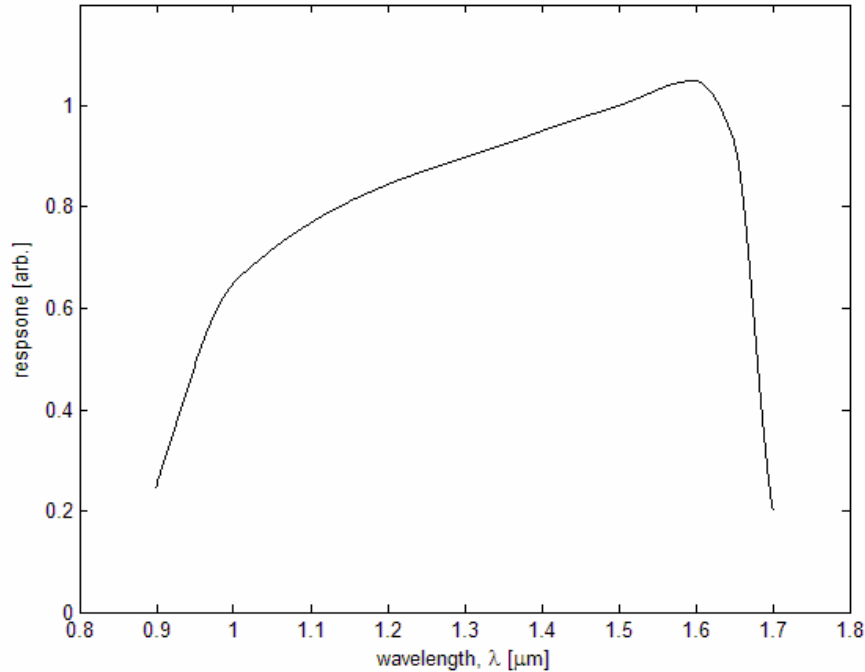


Figure 8: Relative spectral response of InGaAs FPA in the Indigo Alpha NIR imager.

was used to collect MWIR imagery of detonations at 40 Hz. While this allowed temporal information of the fireball to be analyzed, the detonation emissions occurred much too quickly to be acquired. Thus the Iris imager was of limited use in studying the evolution of detonation events and was used to obtain MWIR area profiles only.

The Canon imager is an RGB camera that records video at 30 Hz and also features a microphone for recording audio. It was used to acquire low-speed RGB imagery of the detonation events, which was not analyzed in this research. Rather, the audio track was used in conjunction with the timestamp in the video to determine at what time the shockwave arrived at the measurement site.

### Field Tests

This section discusses the three field tests from which data were collected. The Bronze Scorpio tests were of small munitions detonations. The Dual Thrust Smokey

SAM tests measured missile plumes emissions. Finally, the Muzzle Flash tests were used to characterize the flashes from small arms fire.

The Bronze Scorpio field tests were conducted at the US Army Yuma Proving Ground in Yuma, Arizona from 17-19 November, 2004 as part of the National Air and Space Intelligence Center's effort to "investigate signatures from Improvised Explosive Devices" [26]. These tests consisted of 65 detonation events, primarily of 105mm M760 howitzer shells and 155mm M107 howitzer shells filled with either TNT or Composition B (Figure 9). The munitions were either erect (standing on end with the nose vertical) or prone (nose horizontal). A smaller number of C-4 and improvised (multiple munitions placed in a barrel) detonations were also included. Additional information on the Bronze Scorpio tests can be found in the *Bronze Scorpio Test Report* [26].

There were two measurement sites, both approximately 1100 meters from ground zero (Figure 10). Instrumentation of interest to this research was the Canon, Phantom, Indigo, and Irris imagers. Not all events were acquired by each instrument (due to pointing and focusing issues, downtime required to download data, instrument



Figure 9: 155mm Composition B shell, 155mm TNT shell, and 105mm TNT shell (left to right) detonated during the Bronze Scorpio field tests.



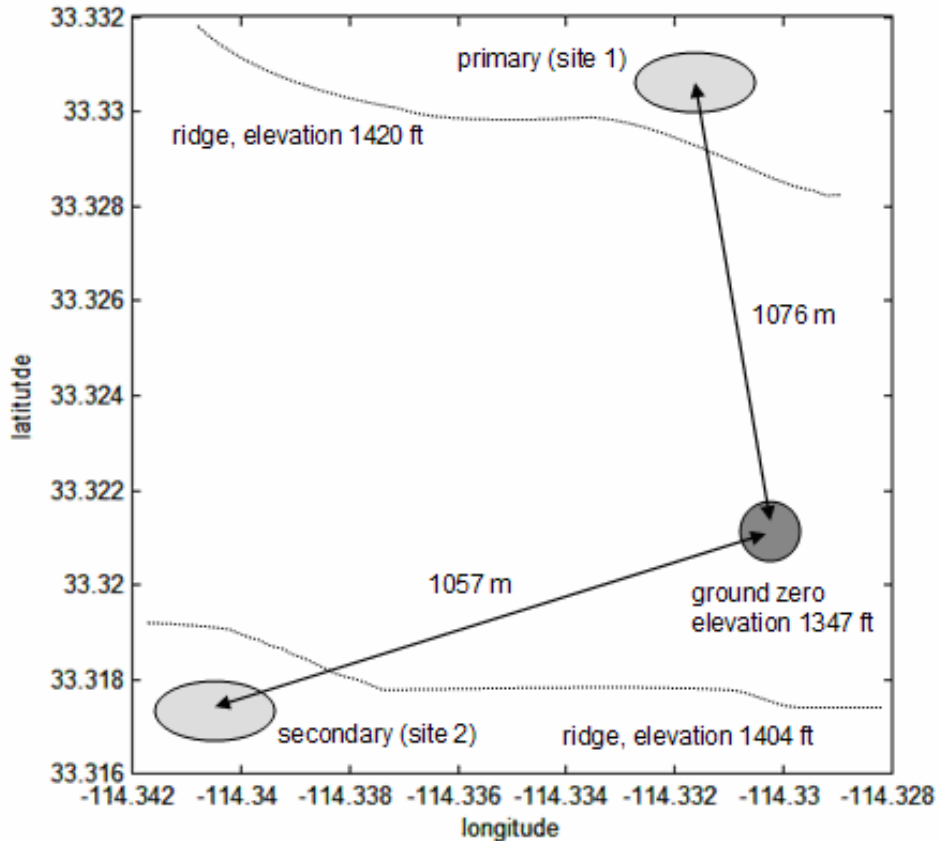


Figure 10: Bronze Scorpio test layout. Both instrumentation sites were located above ground zero, approximately 1100 meters away.

malfunction, or operator error). The test matrix that shows which events had data collected by which of these instruments is shown in Table 3. Indicated is whether the munitions were detonated during the day or at night, which significantly affected the amount of background noise in the visible, and to a lesser extent the NIR and MWIR. Also shown is the composition of the explosive material, the size of the munitions casing, the weight of explosive material, and the orientation of the munitions.

Imagery and spectra from six Dual-Thrust Smokey SAM (DTSS) plumes were collected on October 26, 2005 at the Wright Patterson AFB Area B Test Range (Figure 11). All tests were alike, with two propellants burned sequentially in each DTSS,

Table 3: Test matrix for Bronze Scorpio. Data collected and examined are denoted by a “Y”; data that have yet to be acquired by AFIT (not examined) are denoted by an “X”.

#	Light	Munitions	Size	Weight	Orient.	Phantom	Indigo	Irris	Canon
1	day	TNT	155mm	6.64 kg	Erect	Y	Y	X	Y
2	day	TNT	155mm	6.64 kg	Erect		Y	X	Y
3	day	TNT	155mm	6.64 kg	Erect	Y	Y	X	Y
4	day	TNT	155mm	6.64 kg	Erect		Y	X	Y
5	day	TNT	155mm	6.64 kg	Erect	Y	Y	X	Y
6	day	TNT	155mm	6.64 kg	Prone		Y	X	Y
7	day	TNT	155mm	6.64 kg	Prone	Y	Y	X	Y
8	day	TNT	155mm	6.64 kg	Prone		Y	X	Y
9	day	TNT	155mm	6.64 kg	Prone	Y	Y	X	Y
10	day	TNT	155mm	6.64 kg	Prone	Y	Y	X	Y
11	day	TNT	105mm	2.09 kg	Erect		Y	X	Y
12	day	TNT	105mm	2.09 kg	Erect	Y	Y	X	Y
13	day	TNT	105mm	2.09 kg	Erect		Y	X	Y
14	day	TNT	105mm	2.09 kg	Erect	Y	Y	X	Y
15	day	TNT	105mm	2.09 kg	Erect		Y	X	Y
16	day	TNT	105mm	2.09 kg	Prone	Y	Y	X	Y
17	day	TNT	105mm	2.09 kg	Prone		Y	X	Y
18	day	TNT	105mm	2.09 kg	Prone	Y	Y	X	Y
19	day	TNT	105mm	2.09 kg	Prone	Y	Y	X	Y
20	day	TNT	105mm	2.09 kg	Prone		Y	X	Y
21	day	C-4		3x0.57 kg		Y	Y	Y	Y
22	night	TNT	155mm	6.64 kg	Erect		Y	Y	X
23	night	TNT	155mm	6.64 kg	Erect	Y	Y	Y	X
24	night	TNT	155mm	6.64 kg	Erect		Y	Y	X
25	night	TNT	155mm	6.64 kg	Erect		Y	Y	X
26	night	TNT	155mm	6.64 kg	Erect	Y	Y	Y	X
27	night	TNT	155mm	6.64 kg	Prone	Y	Y	Y	X
28	night	TNT	155mm	6.64 kg	Prone		Y	Y	X
29	night	TNT	155mm	6.64 kg	Prone	Y	Y	Y	X
30	night	TNT	155mm	6.64 kg	Prone		Y	Y	X
31	night	TNT	155mm	6.64 kg	Prone		Y	Y	X
32	night	TNT	105mm	2.09 kg	Erect		Y	Y	X
33	night	TNT	105mm	2.09 kg	Erect	Y	Y	Y	X
34	night	TNT	105mm	2.09 kg	Erect		Y	Y	X
35	night	TNT	105mm	2.09 kg	Erect	Y	Y	Y	X
36	night	C-4		4.55 kg			Y	Y	X
37	night	TNT	105mm	2.09 kg	Erect		Y	Y	X
38	night	TNT	105mm	2.09 kg	Erect		Y	Y	X
39	night	TNT	105mm	2.09 kg	Erect	Y	Y	Y	X
40	night	TNT	105mm	2.09 kg	Erect		Y	Y	X
41	night	TNT	105mm	2.09 kg	Erect		Y	Y	X
42	night	TNT	105mm	2.09 kg	Erect	Y	Y	Y	X
43	night	C-4		4.55 kg		Y	Y		X
44	night	C-4		4.55 kg			Y	Y	X

#	Light	Munitions	Size	Weight	Orient.	Phantom	Indigo	Irris	Canon
45	night	TNT	155mm	6.64 kg	Erect		Y	Y	X
46	day	TNT	155mm	6.64 kg	Erect	Y	Y	Y	X
47	day	TNT	155mm	6.64 kg	Erect	Y	Y	Y	Y
48	day	C-4		4.55 kg			Y	Y	Y
49	day	TNT	155mm	6.64 kg	Erect		Y		Y
50	day	TNT	155mm	6.64 kg	Erect		Y	Y	Y
51	day	TNT	155mm	6.64 kg	Erect		Y	Y	Y
52	day	TNT	155mm	6.64 kg	Erect	Y	Y	Y	Y
53	day	C-4		4.55 kg		Y	Y	Y	Y
54	day	Comp. B	155mm	6.64 kg	Erect	Y	Y	Y	Y
55	day	Comp. B	155mm	6.64 kg	Erect		Y		Y
56	day	Comp. B	155mm	6.64 kg	Erect	Y	Y	Y	Y
57	day	Comp. B	2x155mm	2x6.64 kg	Erect	Y	Y	Y	Y
58	day	Comp. B	155 mm	6.64 kg	Erect		Y	Y	Y
59	day	Comp. B	2x155mm	2x6.64 kg	Erect	Y	Y	Y	Y
60	day	Comp. B	155mm	6.64 kg	Erect		Y	Y	Y
61	day	Comp. B	2x155mm	2x6.64 kg	Erect	Y	Y	Y	Y
62	day	TNT	155mm	6.64 kg	Erect		Y		Y
63	day	TNT/C-4*	155mm/	6.64/13.64 kg			Y	Y	Y
64	day	TNT/C-4*	155mm/	6.64/13.64 kg			Y		Y
65	day	C-4		13.64 kg		Y	Y		Y

\* munitions placed in a barrel



Figure 11: Dual Thrust Smokey SAM test setup at Wright Patterson AFB, Area B Test Range. The DTSS was fixed approximately 1.5 meters above a concrete runway.

simulating the propellants used in an actual SAM. The propellant for the first thrust was Smokey SAM Mix IH210-03B-SSAMS-0665, and the second thrust burned Modified Sagger SAM Propellant IH210-04A-DTSS-0018. All DTSSs were ignited after dark to minimize background noise.

The DTSSs were held stationary approximately 1.5 meters above a concrete runway and collection instruments were placed 139 feet away at a 90 degree angle to the fuselage. The instrumentation of interest to this research was the Indigo imager. Additional information on the DTSS tests, including information on reproducibility of features in the NIR, is contained in *Dual Thrust Smokey SAMs: NIR Quick-look* [27].

The final set of field tests involved acquiring imagery and spectra from 140 rounds of ammunition collected from November 28-30, 2005 at Range 1 of Area B on Wright Patterson AFB. Muzzle flashes from four types of ammunition were collected but only three of the types were examined because the limited number of events of the fourth type (five) was not statistically meaningful. These included a frangible bullet propelled with standard gunpowder and a novel low flash powder, labeled “conventional” and “novel,” respectively. The third ammunition type was a full metal jacketed (FMJ) bullet with the novel powder. The primary differences between the frangible rounds and the FMJ rounds were that the frangible bullets were lighter and thus had greater velocities exiting the firearm barrel.

All rounds were fired from a .45 caliber semi-automatic held stationary in a Ransom Rest approximately three feet off the ground. The rounds were fired in sequences of 5-7 rounds at a time (one magazine), with fewer rounds being fired in the event of a jam. The instrumentation included two Indigo Alpha NIR imagers, a Canon

RGB imager, a high speed Phantom RGB imager, an ABB Bomem MR-254 spectro-radiometer, an ABB Bomem MR-154 spectro-radiometer, and an Acton visible grating spectrometer, with the latter three not being discussed because they were not used in this research.

Of importance to the current analysis was the Indigo imager located perpendicular to the barrel at 181 cm. The test matrix indicating how many and what type of rounds were fired in each sequence, as well as how many rounds were acquired with the Indigo imager used, is shown in Table 4. Additional information on the Muzzle Flash tests and the novel “flashless” powder can be found in *Muzzle Flash Test: NIR Quick-look and Conventional and Q30 Flashless Gunpowder Preliminary Test Report* [28][29].

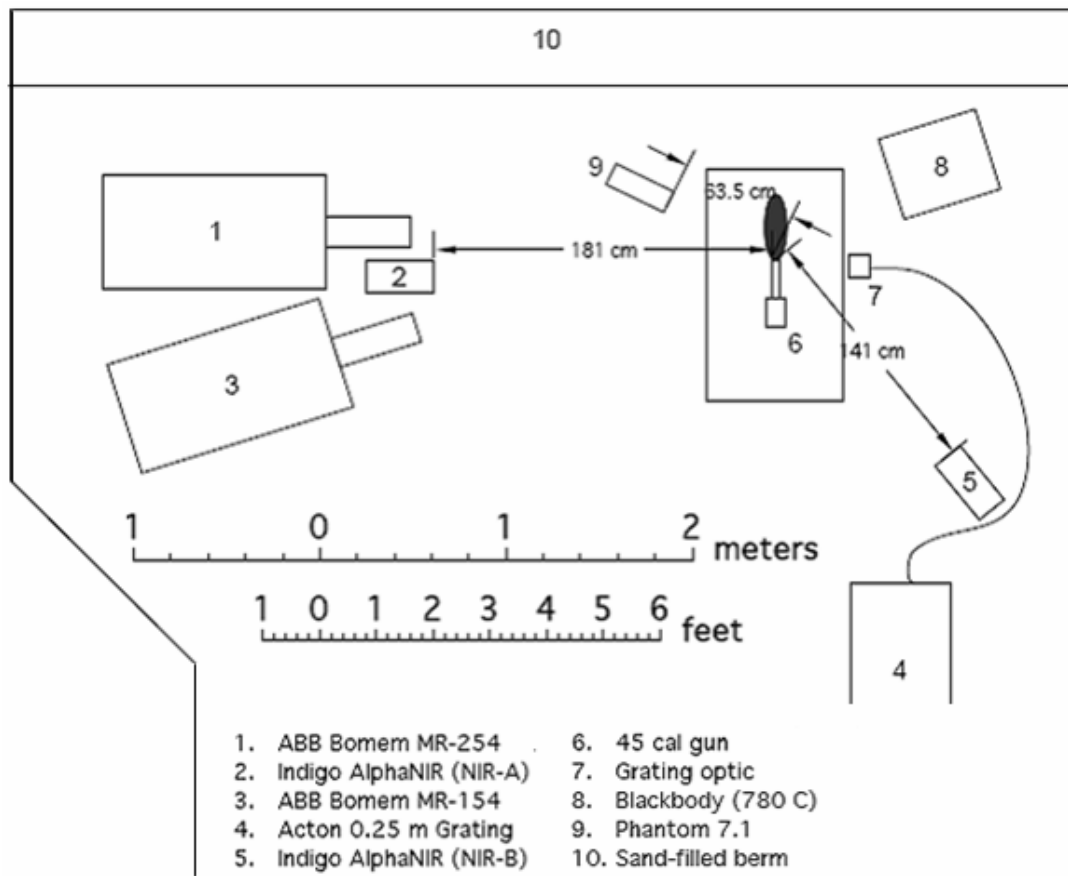


Figure 12: Muzzle Flash Test setup geometry.

Table 4: Test matrix for Muzzle Flash Tests indicating ammunition type, number of rounds fired, and number of rounds acquired with the Indigo imager.

Sequence	Ammunition	# rounds	# acquired	fraction
001	conventional	7	4	0.571
002	conventional	6	3	0.500
003	conventional	4	2	0.500
004	conventional	7	2	0.286
005	novel	7	1	0.143
006	novel	6	4	0.667
007	novel	7	3	0.429
008	novel	7	1	0.143
009	conventional	1	1	1.000
010	conventional	7	4	0.571
011	conventional	1	1	1.000
012	conventional	7	4	0.571
013	conventional	5	1	0.200
014	conventional	2	0	0.000
015	conventional	1	0	0.000
016	conventional	6	1	0.167
017	conventional	5	0	0.000
018	novel	3	2	0.667
019	novel	4	1	0.250
020	novel	7	1	0.143
021	novel	7	5	0.714
022	novel	2	1	0.500
023	novel FMJ	1	1	1.000
024	novel FMJ	6	4	0.667
025	novel FMJ	6	3	0.500
026	novel FMJ	6	3	0.500
027	novel FMJ	6	2	0.333
028	Wolf	1	1	1.000
029	Wolf	5	1	0.200
Total		140	57	0.407

## Data Extraction

Analysis of the afterburn fireballs, DTSS plumes, and muzzle flashes was not conducted on the raw imagery files acquired by each instrument. Rather, the data were input into Matlab where more sophisticated data processing could be used. For the Indigo and Iiris imagers, this was accomplished with Matlab scripts (written by Tom

Fitzgerald of ATK Mission Research) that read the raw data directly from the instrument's imagery file and saved them in a Matlab structure. For every frame of imagery, the Matlab structure contained a matrix representing the digital numbers (DNs) of each pixel. Since both imagers are 12-bit, these DN's ranged between zero (no signal) and 4095 (saturation).

Importing the Phantom imagery into Matlab was more complicated because the imagery files use a proprietary file structure. Without knowing how the files were encoded, a reader could not be developed. Instead, imagery from the Phantom camera was converted to an uncompressed, 24-bit AVI movie. These were read into Matlab structures using built-in Matlab functions. The structures were similar to that of the IR imagers, with the difference being that the Phantom structures contained a matrix of 8-bit DN values for each of the RGB bands for each frame. This preserved the quality of the data, but due to the extremely large AVI file sizes, processing time was extensive.

The Phantom camera provided imagery of the shockwave in addition to the fireball. The shocks were visible, albeit faintly, due to the change in index of refraction they caused as they passed through the atmosphere (see Figure 13 – the shockwave is visible in the video but very difficult to distinguish in a static image without image processing). Since viewing the shock depends on viewing the disturbance it causes to light passing through it (from the landscape in the background), the shock could only be seen for events that occurred during the day. Additionally, due to the variations in the landscape, automated processing of the shockwave's position was not attempted. Instead, the position of the shock relative to the point of detonation was measured manually in steps of 5-10 ms from the time it was first visible until the shock exited the field of view;

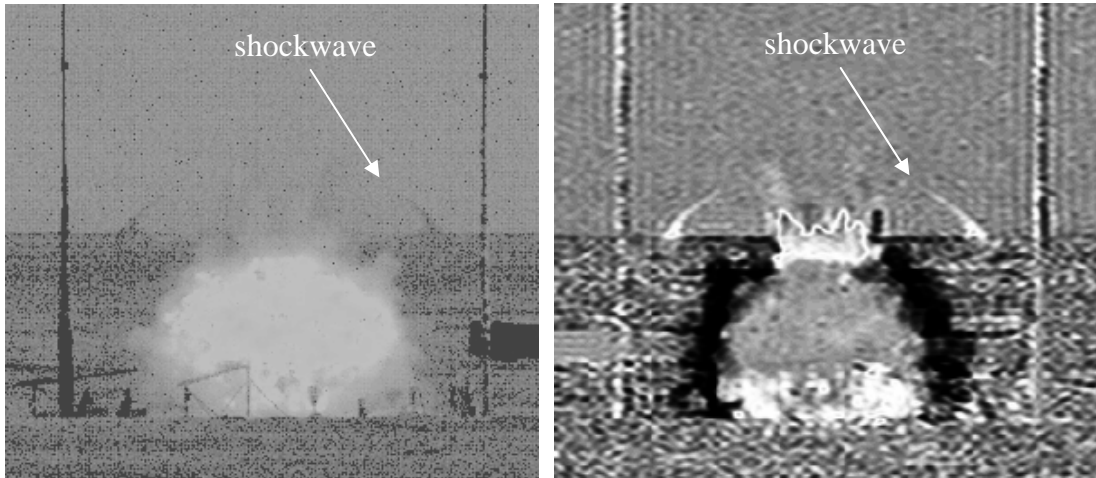


Figure 13: Static image of a Bronze Scorpio detonation with its shockwave (left) and the same image after image processing (right). The index change due to the shockwave is difficult to see in the original image, but with background subtraction and contrast adjustment, it can be seen as a nearly spherical shell propagating away from the detonation.

this amounted to six to ten data points. A late-time data point was obtained using the Canon video to determine the time of detonation and then listening for the boom as the shockwave reached the camera on the audio track.

There was an uncertainty of approximately 10 pixels in the measurement of the shockwave's position. This was due to the thickness of the shockwave and its faintness, both of which made it difficult to distinguish where its position could consistently be measured. Taking the IFOV of the Phantom camera into account, this translates into approximately half of a meter. The uncertainty in the late-time measurement of the shock position was approximately 0.3 seconds. This is an uncertainty of approximately ten percent, but it gave a rough approximation of the velocity of the shockwave at the measurement site (and thus the extent to which the shockwave had transformed to an acoustic wave).

Ideally, the shockwave would be spherically symmetric and measurements of the



shock position could be taken in any direction. In reality, the shock appeared elliptical at early times (although it approached spherical rather quickly) and so for consistency, the position of the shock was measured in the vertical direction. The position and time values were stored in an Excel spreadsheet that was accessible to both TableCurve 2D for curve fitting and Matlab for analysis.

### Data Processing

In general, the events being observed occupied only a fraction of the field of view of the instrument and an even smaller fraction of the total number of frames recorded. This inflated file sizes with useless data and made processing go much more slowly. To more efficiently handle data, the Matlab structures were truncated by eliminating all but a handful of background frames. Additionally, the event matrices were cropped on all sides to slightly larger than the event dimensions. This can be seen for the NIR imagery in Figure 14, which is representative of the cropping for all instruments and events.

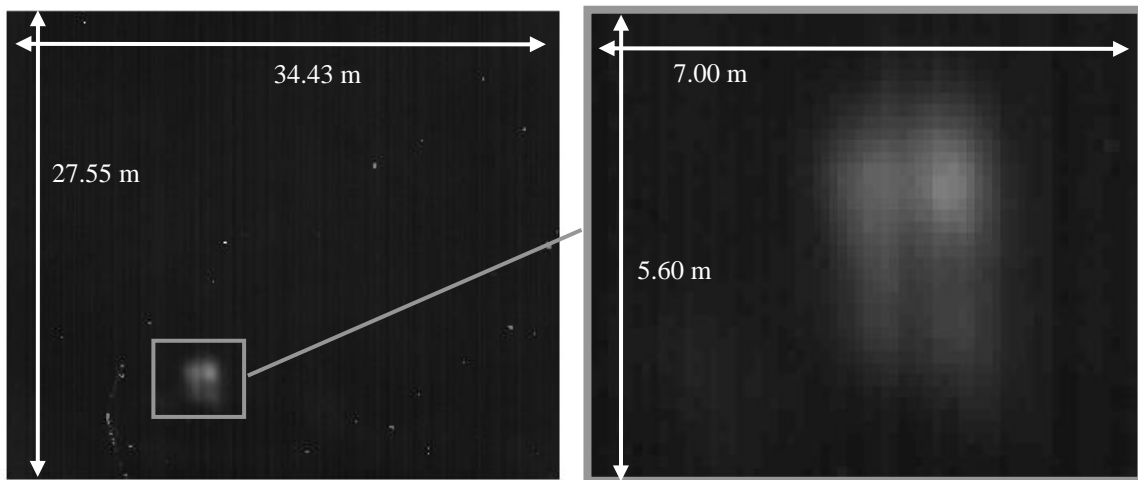


Figure 14: Detonation fireball as seen from the Indigo Alpha NIR imager's full field of view (left) and the cropped image (right).

The above processing did not alter the data from their raw format. In order to perform calculations for the fireballs in the Phantom's blue band, however, hot pixels – pixels with a DN above some threshold value – that were not associated with the fireball needed to be removed. This was because calculations of the fireball area were dependent on hot pixels, and non-fireball hot pixels would skew the result (the exact criteria for a pixel being hot are discussed in the *Area Profiles* section). These were pixels that viewed the smoke and debris cloud near to the ground and were saturated by reflected or emitted light in the blue band only (see Figure 15). Removing them was accomplished by applying a mask to each frame of the blue imagery so that only the region around the fireball remained. The mask was computed by identifying the hot pixels in the red band and defining a rectangular region with a ten pixel buffer to each side. Everything in the blue matrix outside of this mask was set to a digital number of zero.

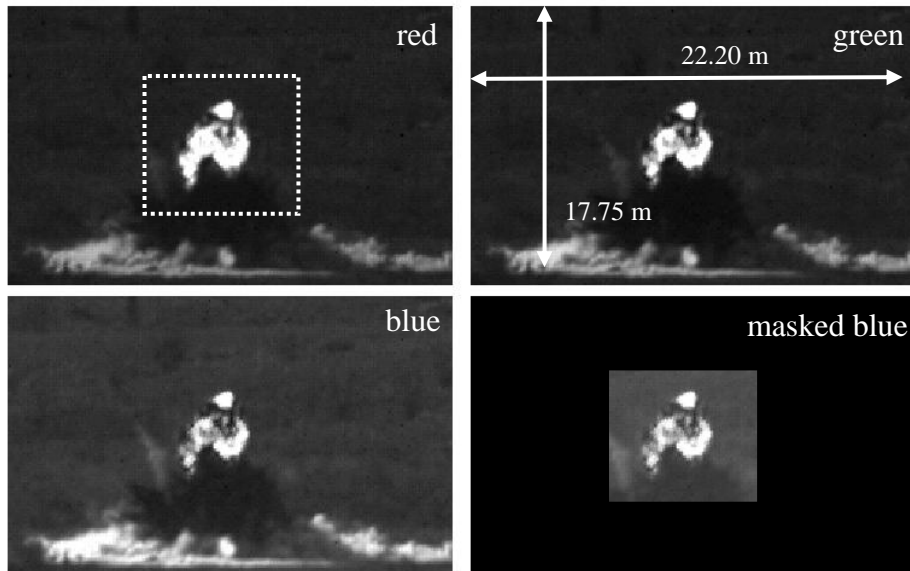


Figure 15: Detonation fireball as viewed by the Phantom camera in the red (upper left), green (upper right), and blue (lower left) bands. Due to the brightness of the smoke and debris in the blue band, the blue image was masked (lower right) so that only hot fireball pixels would be seen. The mask was based on hot pixels in the red band, with a ten pixel buffer on each side.

## Area Profiles

The simplest features of the fireball to extract from imagery were those relating to the size and duration of the fireball (missile plumes and muzzle flashes had many of the same features and, although not always explicitly mentioned, these types of combustion events are assumed to be included in descriptions of fireball feature extraction). To examine the fireballs' characteristics quantitatively, metrics had to be established that gauged the fireball's size and duration. The metrics used were taken from the histograms of the imagery as a function of time, as in Figure 16. In these temporal histograms, the numbers of pixels,  $N$ , as functions of digital number are plotted for each frame of imagery for a munition detonation in the MWIR (left) and a DTSS plume in the NIR (right). While the distribution of DN's was band dependent and varied for event type, the common characteristics included a spike in pixel number at low DN's corresponding to background, low pixel numbers in the mid DN's before and during the combustion event, and a smaller spike in the high DN's from pixels illuminated by combustion emissions.

Because of the bimodal distribution, the histograms provided an opportune way to determine fireball size – the spike in high DN's corresponds to fireball illuminated pixels. The size of the fireball (for each frame of the image) was calculated by summing over the number of pixels at each digital number in the histogram,  $N_i$ , that were above some threshold and then multiplying by the area viewed per pixel (Equation 25). From geometry, the area viewed per pixel,  $A_{px}$ , as a function of the IFOV of the instrument,  $\theta_{px}$ , and the distance from the event,  $d$ , is given in Equation 26.

This metric provides an area profile as a function of frame (but was converted to a function of time by dividing by the instrument's frame-rate) and is referred to as the

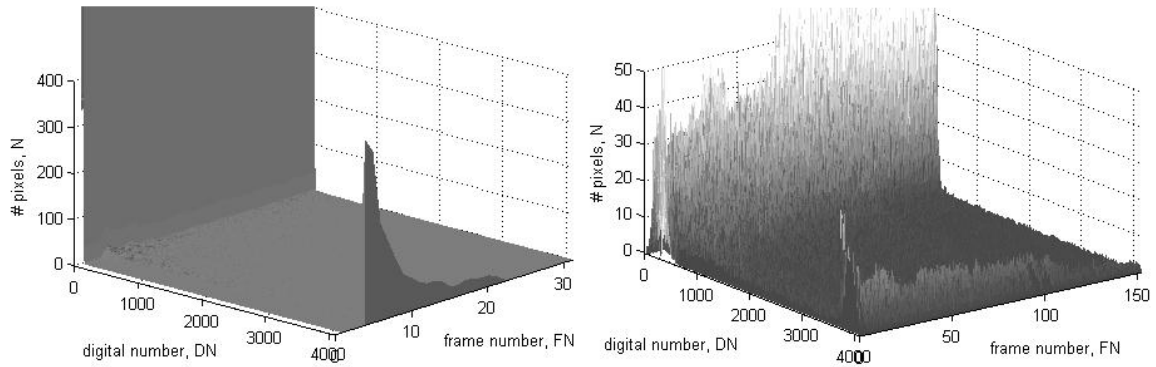


Figure 16: The MWIR histogram of a Bronze Scorpio detonation event (left), representative of all Bronze Scorpio events, shows excellent separation between dark pixels and hot pixels. The temporal histogram of a typical DTSS in the NIR (right) also exhibits separation between background and hot pixels, but the distributions are wider. This is indicative of a wide range of intensity levels in the combustion event, and can be attributed to reflection from gases and surroundings.

$$A_{th} = A_{px} \sum_{i=DN > DN_{th}}^{DN_{max}} N_i \quad (25)$$

$$A_{px} = (\theta_{px} d)^2 \quad (26)$$

threshold area,  $A_{th}$ . It is simply a sum of hot pixels in the instrument's field of view for each frame of the image, where hot pixels are defined as those pixels with a DN greater than a threshold digital number,  $DN_{th}$ , up to the maximum,  $DN_{max}$ . Where to set the threshold DN was somewhat arbitrary; it was set high enough that pixels illuminated by background and reflected light were not included in the summation. This is shown in Figure 17, where there is a clear minimum between the background and hot pixels.

This level changed based on which instrument was used and which type of combustion event was being observed. For each of the field tests, however, the threshold was maintained for all events of the field test so that the events would be relatively comparable. Table 5 indicates the threshold DN used for each instrument in the various field tests. In the Bronze Scorpio and DTSS tests, background and reflected light were a

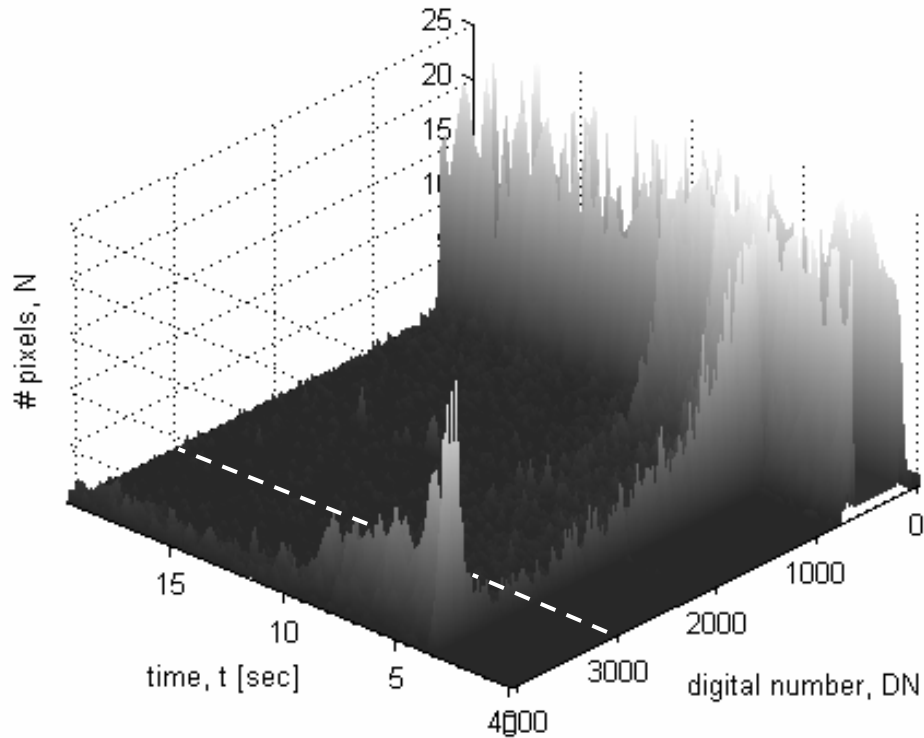


Figure 17: The histogram as a function of time shows a minima near DN 3000. Setting the threshold here (dashed line) assumes that all DNs above this level are due to combustion emissions and that all DNs below this are due to background or reflected light.

concern, so the threshold was set where there appeared to be a minimum in the histogram. In the Muzzle Flash test, however, all events occurred in the dark with a black background, so background and reflected light were not an issue. Because of this, all DNs above the background (calculated as the DNs above which the number of pixels,  $N$ , dropped below 1% of the maximum of the background spike) were considered muzzle flash areas. This level was variable, but was typically around DN 600 and was most likely due to light reflected from gases ejected from the muzzle. The area of the brightest part of the plume (the part thought to be emitting) was based on a threshold of DN 3800. Histograms, thresholds, and imagery of a single frame of each combustion event are shown in Figure 18.

Table 5: Threshold DN for each instrument used in the three field tests. In the Muzzle Flash test, there were two thresholds. The first measured everything above background and was variable for each event. It was set where the background DN spike drop below 1% of its maximum value, typically around DN 600. The second threshold quantized only the DNs of the bright flash and was fixed.

Instrument	$DN_{max}$	Bronze Scorpio $DN_{th}$	DTSS $DN_{th}$	Muzzle Flash $DN_{th}$
Phantom	255	254		
Indigo	4095	3276	3000	600* / 3800
Irris	4095	3276		

\* typical value

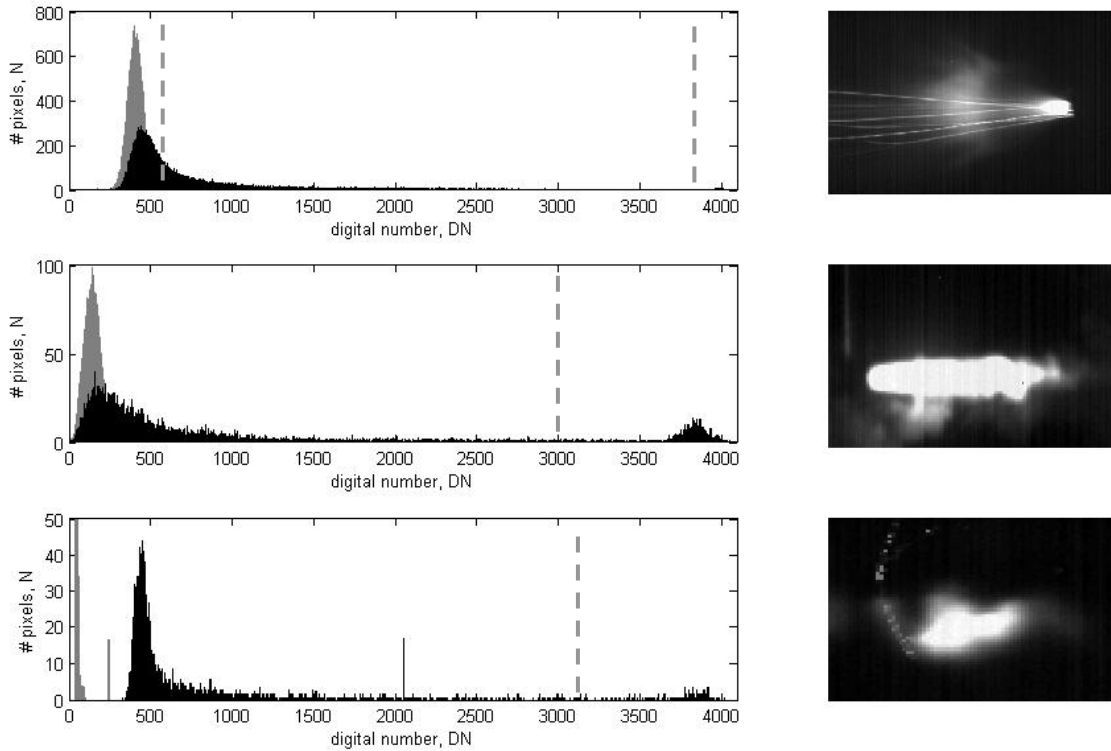


Figure 18: NIR histograms (left) for the corresponding frame of the combustion even (right). From top to bottom, the events are a muzzle flash, DTSS plume, and afterburn fireball. The gray shading in the histogram corresponds to the average background, and the black shading corresponds to the DNs of the event. The threshold levels are indicated with a dashed line.

As can be seen in the histograms, the value at which the threshold DN should be set was not always obvious – there was not always a clear minimum in the separation of background/reflected light and emitted light. Moving the threshold DN up or down, however, did not affect the threshold area profile as a function of time. If it had, determination of the threshold level would have been much more important because it

would have indicated new features were being included or discarded. Rather, changing the threshold merely changed the magnitude of the area profile, as is seen in Figure 19. Maintaining a consistent threshold level for all events in the test was more important to feature comparison than determining the absolute level (if one exists) at which DNs shifted from background and reflection to combustion emissions.

The threshold area was not the only area profile used to examine the size of the afterburn fireball. Four other methods were used to characterize the area profile as a function of time, all of which (erroneously) approximate the fireball as spherical. Two of these included finding the mean location of the hot pixels at the time of detonation, thus

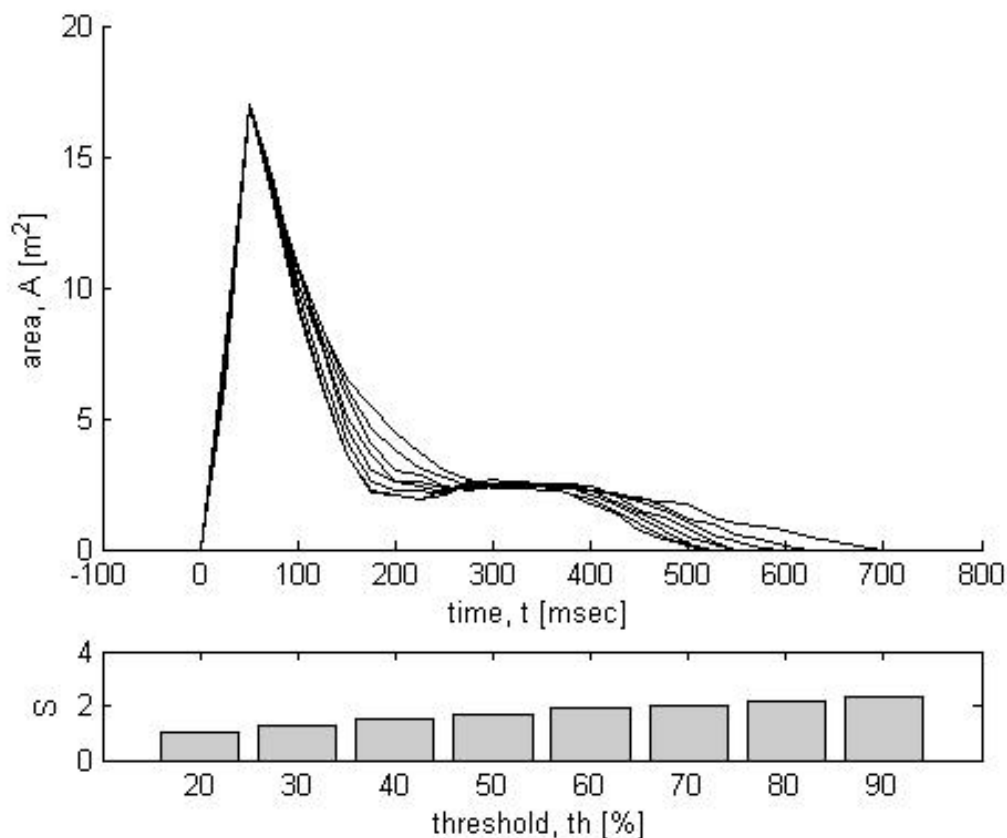


Figure 19: The MWIR area profile of Bronze Scorpio event 26 is relatively independent of the threshold level. Changing the threshold from 20% of the dynamic range through 90% changes only the magnitude of the area, but not its shape as a function of time. The scaling factors,  $S$ , for each threshold level,  $th$ , are indicated below the plots.

locating the detonation origin. The distance to the maximum hot pixel from the origin defined a radius, that when squared and multiplied by  $\pi$ , gave an area profile termed the maximum static area,  $A_{\max}^0$ . The maximum dynamic area,  $A_{\max}$ , was calculated in the same manner as  $A_{\max}^0$  except that the origin was calculated for each frame (under the assumption that the fireball translated as it evolved). Both of these metrics overestimated fireball size by assuming that cool pixels (those below threshold) closer to the origin than the maximum radius were fireball that was obscured by dirt, smoke, and other debris.

The remaining two area metrics also used the static and dynamic origin. In these, however, the standard deviation of the distance between the origin and all hot pixels in the image was found. This defined a statistical radius that assumed the obscured fireball was distributed normally and that the area determined by taking three times this radius (three standard deviations) encompassed 99% of the fireball. These area profiles were termed three sigma static area,  $A_{3\sigma}^0$ , and three sigma dynamic area,  $A_{3\sigma}$ .

The five area profiles of a munitions detonation are shown in Figure 20 for reference. Because of the range of magnitudes involved – less than ten to greater than one hundred square meters – the log of the areas are plotted as a function of time. It is clear that each profile is different, and thus each will have different features that can be extracted from it. In this research, however, time was limited and features were only extracted from the threshold area profile. The others are mentioned because they show potential for use in classification and phenomenology in future study. In the remainder of this paper, the terms *area* and *area profile* will refer to threshold area and threshold area profiles.



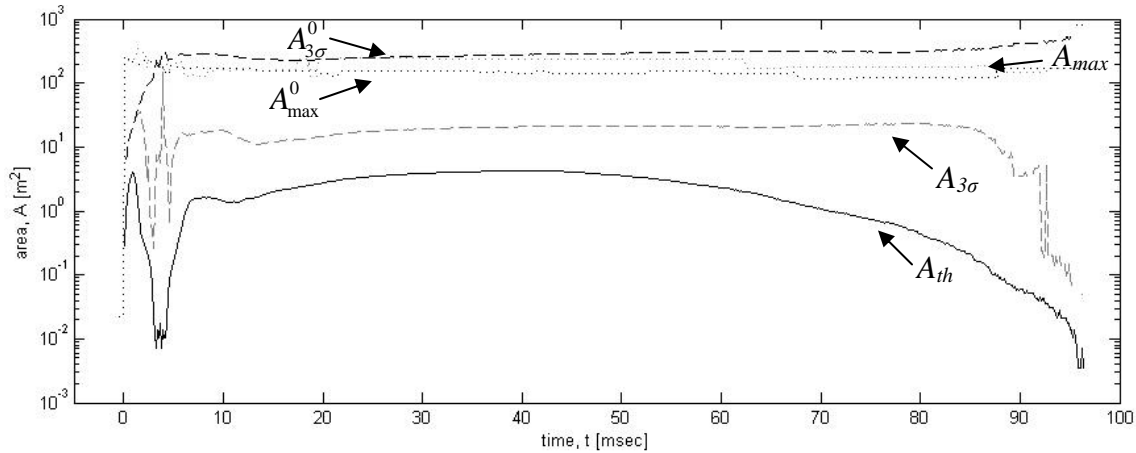


Figure 20: The five area profiles are plotted for a Bronze Scorpio event in the red band. Threshold area (solid dark line) is several orders of magnitude below the maximum static (dotted dark line) and maximum dynamic (dotted gray line) areas. The three sigma static profile (dashed dark line) predicts the largest area, but the three sigma dynamic area (dashed gray line) has a much lower magnitude.

## Combustion Features

By examining the area profile for a typical Bronze Scorpio detonation (Figure 21), several features are apparent. These include the sharp spike in the area profile due to the initial flash at detonation,  $A_{det}$ , the peak area of the afterburn fireball (or more generically, the peak area of the combustion event),  $A_{pk}$ , and the times after detonation that these peaks occur,  $t_{det}$  and  $t_{pk}$ . Three additional features relating to the duration of the fireball are the time at which its area falls below 50% and 10% of  $A_{pk}$ , denoted by  $t_{50}$  and  $t_{10}$ , and the time at which the area falls within three standard deviations of the average noise level,  $t_n$ . The total area under the curve,  $A_t$ , is found by integrating the area profile with respect to time.

With the exception of the detonation peak features, these features were valid for all of the imagers (the detonation features could not be extracted in the IR because the

instruments were too slow to resolve the initial spike). These features were also extracted from the DTSS plume, excluding the detonation spike (because there was no detonation flash in the missile plume). The muzzle flashes, however, were very short lived and occupied only a single frame of imagery. Because of this, there was no area profile, but rather a single (peak) area – the area of the muzzle flash,  $A_{pk}$ . The goal of these tests was to determine the visibility of the flash; thus  $A_{pk}$  includes everything above background, both from reflection and emission. A second feature that was extracted from the muzzle flash is the area of strong emission characterized by DNs near saturation. This is the flash (or saturation) area,  $A_{sat}$ , and as mentioned previously, includes DNs above 3800.

Finally, because of the extremely high temporal resolution of the Phantom camera, the area profiles in the red, green, and blue were used as features. This was accomplished by interpolating the area profiles for each event onto a uniform time axis ranging from zero (detonation) to 200 milliseconds (well after the fireball has decayed) in steps of 0.1 milliseconds. This interpolation was necessary for comparing the time dependent features, since a point by point comparison required all of the profiles to have

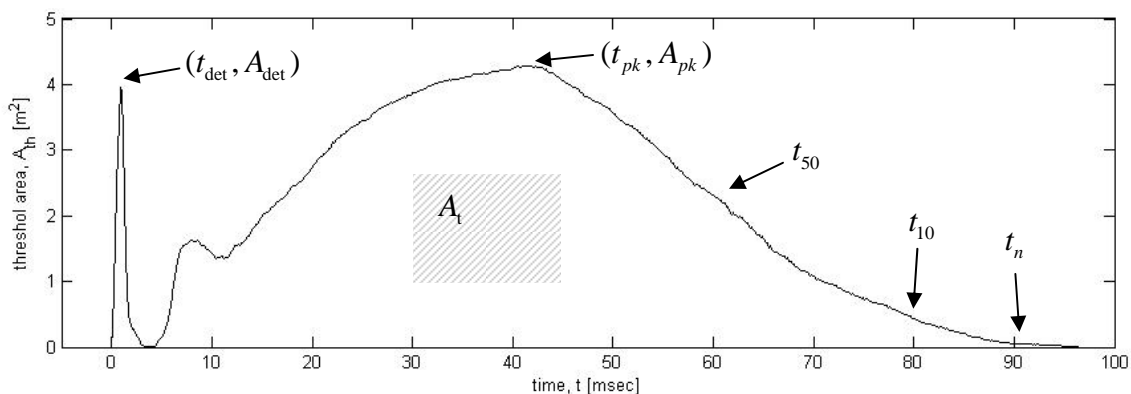


Figure 21: Threshold area profile as a function time for a Bronze Scorpio detonation in the red band. The features that may be extracted from the profile are indicated.

the same temporal sampling (the profiles all had to be mapped to the same axis). A tabulation of the features from the afterburn fireball (combustion event) that were examined is given in Table 6.

Table 6: Features extracted from the afterburn fireball in each band, denoted by an “x”.

feature	Red	Green	Blue	NIR	MWIR
$A_{det}^{**}$	x	x	x		
$A_{pk}^{**}$	x	x	x	x	x
$t_{det}$	x	x	x		
$t_{pk}$	x	x	x	x	x
$t_{50}$	x	x	x	x	x
$t_{10}$	x	x	x	x	x
$t_n$	x	x	x	x	x
$A_t$	x	x	x	x	x
$A_{sat}^*$				x	
$A_{th}(t)$	x	x	x		

\* Muzzle Flash test only

\*\* Bronze Scorpio only

## Shock Expansion Models

There were only a handful of data points collected for position as a function of time from the imagery of the shockwave. This, combined with the non-uniformity in time steps at which the positions were measured and the uncertainty of approximately one half of a meter in the measurements, made the data points themselves unsuitable for use as features. Instead, these data points were used to fit various shock expansion models. Once a functional form of the shockwave’s radius with time was obtained, features were extracted from it. The quality of the fit also provided information on which models worked best, which in turn provided information on phenomenology.

The first two models which were fit to the data are the drag and shock expansion models (Equations 11 and 21). Both of these models are only valid prior to the far-field, where the overpressure of the shock is much greater than ambient pressure. The shock

model is also not valid in the near-field, where the mass of the explosive is not negligible. The region where both models are valid is quantized by Equation 17. Inserting values of  $E_D$ , and  $m_0$  from the properties of TNT and Composition B, and assuming values of 1.4, 1.2 kg/m<sup>3</sup>, and 1 atm for  $\gamma$ ,  $\rho_0$ , and  $p_0$ , the limiting values of the mid-range for the munitions studied in the Bronze Scorpio tests were calculated and are shown in Table 7.

The values of detonation energy used for Composition B were not found in the literature and had to be approximated. By assuming the energies released by the TNT and the RDX in the initial detonation are independent of each other, the heat of detonation of Composition B can be assumed to scale in proportion to the mixture ratios (Equation 27). This estimates the energy released in the detonation of Composition B to be 5573 kJ/kg, which when multiplied by the mass of Composition B, is the value that was used for the energy released in the detonation,  $E_D$ , in the above table.

$$\Delta H_D^{CompB} = 0.39\Delta H_D^{TNT} + 0.6\Delta H_D^{RDX} = 0.39(4563) + 0.6(6322) = 5573 \quad (27)$$

Because the position of the shock was examined at distances extending well into the far-field (both from data points taken from the Phantom imagery and the late-time

Table 7: Material properties are shown for each munition in the Bronze Scorpio tests. These, along with the assumed atmospheric properties (also shown), allowed the near- and far-field radii to be calculated.

property	155mm TNT	105mm TNT	155mm Comp. B	2x155mm Comp. B
$E_D$ (J)	30298320	9536670	37004720	74009440
$p_0$ (Pa)	101325	101325	101325	101325
$\rho_0$ (kg/m <sup>3</sup> )	1.2	1.2	1.2	1.2
$m_0$ (kg)	6.64	2.09	6.64	13.28
$\gamma$	1.4	1.4	1.4	1.4
$\zeta_0$	1.165	1.165	1.165	1.165
near-field $R$ (m)	1.097	0.746	1.097	1.382
far-field $R$ (m)	2.426	1.650	2.593	3.267

point from the Canon audio), it was necessary to also use models which could take the late-time behavior of the shockwave into account. As stated previously, as the shock's overpressure and velocity decrease, it gradually transitions from a shockwave to an acoustic wave traveling at the speed of sound,  $c_0$ . A modification of the explosive model that approximates the mid-field and far-field behavior is the linear combination of the mid-field and far-field solutions (Equations 11 and 18). While this functional form causes deviation from the true model, it captures the basic growth of the fireball in both the mid-field and far-field. The  $t^{2/5}$  causes the mid-field term to dominate at early times but become negligible later, whereas the  $t$  makes the far-field term small at early times but more important at later times. The form shown in Equation 28 approximates the extent of the shockwave as a function of time in both regions.

$$R(t) = \xi_0 \left( \frac{E_D \cdot t^2}{\rho_0} \right)^{1/5} + c_0 t \quad (28)$$

The basic drag model also fails to capture the far-field approach to the speed of sound and instead has the shock approaching a zero final velocity. By modifying the equation of motion governing the shock's behavior, however, a functional form with a final velocity of  $c_0$  can be found. This is shown in Equation 29 where the deceleration is set proportional to the difference between shock's velocity and the speed of sound; when the shock's velocity reaches the speed of sound it stops decelerating. Solving for the shock velocity as a function of time (Equation 30) and then integrating with respect to time (and imposing the boundary condition of zero radius at detonation) yields Equation 31. This modified drag model captures the viscous deceleration of the drag model with the recognized asymptotic behavior of shockwaves at late times.

$$\frac{dD}{dt} = -\beta(D - c_0) \quad (29)$$

$$D(t) = D_0 e^{-\beta t} + c_0 \quad (30)$$

$$R(t) = \frac{D_0}{\beta} (1 - e^{-\beta t}) + c_0 t = R_{\max} (1 - e^{-\beta t}) + c_0 t \quad (31)$$

### Shock Expansion Fits

The four models given above were used to generate six fit functions of the time dependence of the shock's position,  $R(t)$ . All physical quantities that could be combined, such as  $\xi_0 (E_D / \rho_0)^{1/5}$ , were combined into single fit parameters  $a$ ,  $b$ , or  $c$ . These fit functions are shown in Equations 32 through 37. The first two are the explosive and drag models as functions of only two fit parameters,  $a$  and  $b$ . The second pair of fit functions consists of the modified explosive and modified drag models as functions of three fit parameters:  $a$ ,  $b$ , and  $c$ . In these functions, the final velocity of the shock (the speed of sound in air, represented by the  $c$  fit parameter) is left variable. The purpose of this was to improve the quality of the fit as well as to verify that the shock velocity did indeed approach the speed of sound – if fit parameter  $c$  took on values near  $c_0$  as a result of the best fit, it would be evidence that the shockwave did indeed transition to an acoustic wave. The final two equations are the modified explosive and drag models with the speed of sound fixed. This was to ensure that the modified shock and drag models did not fit the data better than their unmodified counterparts merely because they contained an additional fit parameter. The value used for  $c_0$  was 350 m/s, which corresponds to a temperature of 30.33°C. This was warm for November in Yuma, AZ; the actual range of

temperatures was 11°C to 26°C which corresponds to values of  $c_0$  ranging from 338.11 m/s to 347.26 m/s [30][31].

$$R(t) = a \cdot t^b \quad (32)$$

$$R(t) = a \cdot (1 - e^{-bt}) \quad (33)$$

$$R(t) = a \cdot t^b + c \cdot t \quad (34)$$

$$R(t) = a \cdot (1 - e^{-bt}) + c \cdot t \quad (35)$$

$$R(t) = a \cdot t^b + c_0 \cdot t \quad (36)$$

$$R(t) = a \cdot (1 - e^{-bt}) + c_0 \cdot t \quad (37)$$

The position as a function of time, excluding the late-time data point from the Canon camera, was imported into TableCurve 2D (the late-time data point was used to evaluate the quality of the fit at late times). TableCurve 2D uses least-squares fitting routines to fit the input data to user-defined functions. After fitting the functions to the data for each event, the fit parameters, their uncertainties, and the correlation coefficient between the fit and the data were exported into Matlab for feature extraction.

### Shockwave Features

Because the only shockwave information that was used was the position at various times, all of the extracted features were directly or indirectly related to its expansion. Because of how the features were compared (discussed in the *Feature Analysis* section), however, it was useful to transform the position fits to other physical quantities using known relations.

The first of these transformations was simply a determination of the velocity of

the shockwave as a function of time, accomplished by taking the derivative of the fit function with respect to time. This was put in terms of the Mach number,  $M$ . This is shown in Equation 38, where, for consistency the temperature was fixed at 30.33 °C and  $c_0$  was 350 m/s.

$$M(t) = \frac{D(t)}{c_0} = \frac{1}{c_0} \frac{dR}{dt} \quad (38)$$

With the Mach number known as a function of time, the pressure of the shockwave was found using Equation 7. Using the empirical relationship between overpressure and scaled distance, the shockwave's pressure could be related back to an initial release of energy in the detonation,  $E_D$ . An analytic approximation was determined, however, so that all calculations could remain analytic. The least-squares fit of the base 10 log of the scaled distance to the base 10 log of the pressure was found, with the base 10 logs used to more equally weight the data (because the data spanned several orders of magnitude). The approximation is shown in Equation 39 and had excellent correlation for the weighted data ( $r^2 = 0.988$ ) and agreement within 30% for the unweighted data.

$$s = \frac{P_0}{P_1^{3/5}} \quad (39)$$

If the detonation were truly ideal, all of the energy would have been released instantaneously and  $E_D$  would have been constant. Since real munitions detonations are not ideal, however, the apparent energy released became functionally dependent on the time at which the shockwave was examined. Substituting Equation 39 into Equation 10 provides this relationship, which is shown in Equation 40.



$$E_D(t) = \left( \frac{R(t)}{p_0} \right)^3 p_1(t)^{9/5} \Delta H_D^{TNT} \quad (40)$$

All of the above physical quantities,  $R(t)$ ,  $M(t)$ ,  $p_1(t)$ , and  $E_D(t)$ , as calculated from all six fit functions, were used as features of the shockwave. Since they all evolve with time, the function for each physical quantity was evaluated for all times between 0 and 200 milliseconds in steps of 0.1 milliseconds. This led to an enormous number of features that for small separations in time were very closely related. Because of this, only one time step of each feature was used (in comparisons to other features) – but all were evaluated to determine which time yielded the best results.

Another feature of the shockwave (for each fit function) was the efficiency of the detonation,  $f$ . This was calculated as a ratio of the detonation energy that was derived from experimental data to the theoretically determined energy of detonation, as shown in Equation 41. It was used as a feature to determine if there was a correlation between the fractions of energy released in the detonation to the variability in other extracted features. Like the other time-dependent shock features, it was sampled in 0.1 ms increments from 0 to 200 ms, but only one value was used per comparison.

$$f(t) = \frac{E_D(t)}{\Delta H_D m_0} \quad (41)$$

Finally, the fit parameters  $a$ ,  $b$ , and  $c$  for each of the fit functions were used as features of the shockwave. This brought the number of shockwave related features to a total of forty-four (five time dependent features for each of the six fit functions giving a total of thirty physical features, plus an additional fourteen fit parameters from the fit functions themselves).

## Feature Analysis

The primary questions to be answered in this research (which features of the shockwave, fireball, and explosive munitions are reproducible, provide distinguishability, and are correlated with other features?) guided this research in the final phase of data analysis. The first step in answering these questions was to specify how the combustion events were to be categorized. There were five different munitions used in the Bronze Scorpio field tests, detonated in nine total arrangements. Each of the unique arrangements was referred to as a *type*. Combinations of arrangements were referred to as a *group*, and categories of combustion events were referred to as a *class*. For example, 155 mm TNT was a group, but when specifying an orientation, such as 155 mm TNT erect, the unique arrangement was a type. DTSS plumes and muzzle flashes (along with detonations) were classes of combustion events. If all tests were included, the number of types of combustion events was brought up to fourteen. These types and their use in analysis are shown in Table 8.

Grouping these types together was necessary for two reasons. The primary need was the sparsity of the data set. There were a limited number of events of each type and an even fewer number of events acquired by all of the instruments for each type. If only a single type was examined, there were approximately half a dozen or fewer acquired events. By grouping the types, such as all TNT (types 1-4), the number of data points for any given feature increased and became more statistically meaningful. The second reason for grouping the types was to determine which features were unique to the group and which features were unique to the type. Some features were independent of weight but depended very strongly on explosive material, indicating they were features of the

explosive material group. On the other hand, a feature that did depend on the weight was a type feature. Grouping showed which features scaled with which properties of the group and type.

The groups that were examined are given in Table 9. The five munitions were examined individually, as well as in combination with other munitions of the same weight or explosive material. These small groups of one or two types provided information on reproducibility of features and the ability of these features to differentiate between other types or groups. Many of these did not contain enough data points to be

Table 8: Types used in analysis. “Y” indicates use as a stand-alone type, “X” indicated that the type was not analyzed separately but was used in groups with other types, and “N” indicates no analysis was performed on the type.

Type #	Field Test	Arrangement	Used in Analysis
1	Bronze Scorpio	155mm TNT erect	Y
2	Bronze Scorpio	155mm TNT prone	Y
3	Bronze Scorpio	105mm TNT erect	Y
4	Bronze Scorpio	105mm TNT prone	Y
5	Bronze Scorpio	3x1.25# C-4	X
6	Bronze Scorpio	10# C-4	X
7	Bronze Scorpio	155mm Composition B erect	Y
8	Bronze Scorpio	2x155mm Composition B erect	Y
9	Bronze Scorpio	155mm TNT / 30# C-4 / barrel	X
10	DTSS	Dual Thrust Smokey SAM	Y
11	Muzzle Flash	Conventional	Y
12	Muzzle Flash	Novel	Y
13	Muzzle Flash	Novel FMJ	Y
14	Muzzle Flash	Wolf	N

Table 9: Grouping of types for reproducibility, distinguishability, and correlation analysis

Group #	1	2	3	4	5	6	7	8
Types	1	2	3	4	1,2	3,4	1-4	8
Group #	9	10	11	12	13	14	15	16
Types	7,8	1-4,7,8	1-9	10	11	12	13	11-13

meaningful, but it was still useful to see if they produced any results that showed promise for further investigation. The broader groups, i.e. all explosive munitions (types 1-9), weren't particularly useful for reproducibility or distinguishability, but gave a large range of values in the feature sets to determine correlations.

The next step was to determine which features are reproducible. This was performed by calculating the coefficient of variation. Since the  $C_V$  is a statistical metric based on the mean and standard deviation of the feature set, differing which types of munitions were included in the set (group) changed its value. The  $C_V$  was calculated in Matlab for all extracted features in all bands for all groups. For features with time dependence, the  $C_V$  was calculated for each time step and the mean value used as a characterization of the feature's reproducibility. This generated an extensive list of values that were sorted from best to worst (lowest  $C_V$  to highest) for examination.

The Fisher Ratio was then determined by comparing two groups at a time to determine distinguishability. Instead of using all groups in these comparisons, the groups containing only a single munitions type were excluded. This was guided by the low number of data points for each feature in single type groups. While this was acceptable for calculating  $C_V$ , comparisons of two groups where one is not statistically significant would be meaningless for distinguishability. There were three sets of comparisons. The first was a comparison of each class of combustion events against the others – this demonstrated the ability to distinguish very dissimilar events and provided a baseline for how well distinguishability using the  $FR$  performed. The second comparison used only events from the Muzzle Flash test because these types contained features that are relatively simple and reproducible within types. The more complex problem of

distinguishing groups of munitions detonations based on extracted features was also examined. The groups that were compared are shown in Table 10. As with the  $C_V$ , these comparisons generated an extensive list of  $FR$  values that were sorted from best to worst (highest to lowest).

Finally, the correlation between shockwave, fireball, and munitions features in the Bronze Scorpio data set was evaluated based on their coefficient of determination,  $r^2$ . In these comparisons, the munitions features used were the mass,  $m_0$ ; energy released in the detonation,  $E_D$ ; energy released in the afterburn fireball due to combustion,  $E_A$ ; heat of detonation,  $\Delta H_D$ ; and the specific energy released in the afterburn fireball,  $\Delta H_A$ . The time dependent features of the shockwave and fireball were compared at all time steps and the one with the highest  $r^2$  was used as the feature. Since a wide range of feature values were necessary to compute correlation, the groups were all TNT (group 7), all TNT and Composition B (group 10), and all munitions (group 11).

The form of the correlation coefficient used here (Equation 24) determines the linear correlation between two sets of data. A more general form could have been used if other functional forms relating the two features were tested (such as exponential, inverse power, etc.) but in this research, only power laws were tested (with one exception, discussed in the *Analysis and Results: Efficiency* section). This was accomplished by

Table 10: The groups to be compared using the Fisher Ratio are shown for each set of comparisons. These include comparing groups of all combustion events, groups of muzzle flashes only, and groups of munitions detonations only.

Field Tests	Groups	Types
All	11,12,16	[1-9] [10] [11-13]
Muzzle Flash	13-15	[11] [12] [13]
Bronze Scorpio	5,6,7,9	[1,2] [3,4] [1-4] [7,8]

taking the square-root and cube-root of each of the fireball features and determining the linear correlation of these features with the shockwave and munitions features. This effectively determined whether the correlation with the fireball feature was best with a linear, quadratic, or cubic power of the shockwave and munitions features. This is also why all of the position-dependent shockwave features were used; even though the pressure, Mach number, and apparent energy released all depended on measurements of the shock's position as a function of time, they are not related in a linear fashion. Thus, when determining linear correlation, different forms of the same basic information proved to be more useful. Because of the large number of coefficients of determination, the values were sorted, and those features that were highly correlated were examined.

## **Summary**

Detonations of explosive munitions are anything but simple phenomena. Understanding them requires studying their behavior and trying to draw physically meaningful conclusions. This was attempted here, with the results of the process – experimentally observing fireballs and shockwaves in several bands of imagery, determining profiles of the fireball area and models of the shockwave's characteristics, extracting features from the fireball area and shockwave properties, and assessing these features for reproducibility, distinguishability, and correlation – providing a number of findings. The next step was to examine these findings to try to extract the aforementioned conclusions.

## IV. Analysis and Results

### Chapter Overview

This chapter attempts to answer the questions first posed in this research: which features of the shockwave and afterburn fireball are reproducible and provide distinguishability? Which of these features are correlated to characteristics of the explosive munitions? And which of the features of the shockwave are correlated to features of fireball?

Since reproducibility of features is dependent on only a single feature in a single group of munitions, it was the simplest metric to examine and is the first one looked at here. Next, the distinguishability of features was examined between different groups of munitions. Those features with the highest reproducibility are best suited for recognizing munitions types because they identify a consistent signature of an explosive munitions group. These were not always the best features for classification, however, because some features with low reproducibility still provided a high degree of classification, and vice versa. Those features with promise for classification are presented.

Finally, the correlation of features extracted from the shockwave, fireball, and munitions was examined. Those features that had the highest coefficients of determination were used to find scaling laws for to all detonations, detonations of explosives containing TNT, and pure TNT explosives. Also investigated were those features that had low reproducibility to determine if variability in one feature was correlated to variability in the other feature. A number of specific feature correlations were examined and are discussed throughout the analysis.

## Reproducibility of Area Profiles

Before examining which specific features are the most reproducible, looking at the reproducibility of the area profiles as a function of time is instructive. Figure 22 shows the area profiles for the six individual erect 155mm TNT detonations (thin lines), along with the mean profile (thick line) and the standard deviation (shaded region) of the set; the plots shown are for the red band, but the green and blue bands show very similar profiles. It is clear that even for events of the same weight, composition, and orientation there is a great deal of variability in the fireball size as a function of time – the peak fireball areas differ in both magnitude and time of occurrence, and the duration of the fireball varies by a factor of two. The most reproducible aspects of the detonation appear to occur at very early times (less than 10 milliseconds) and include the time and peak area of the detonation.

If all TNT (155mm erect, 155mm prone, 105mm erect, and 105mm prone) detonations are grouped together, the variability of the area profiles does not appreciably

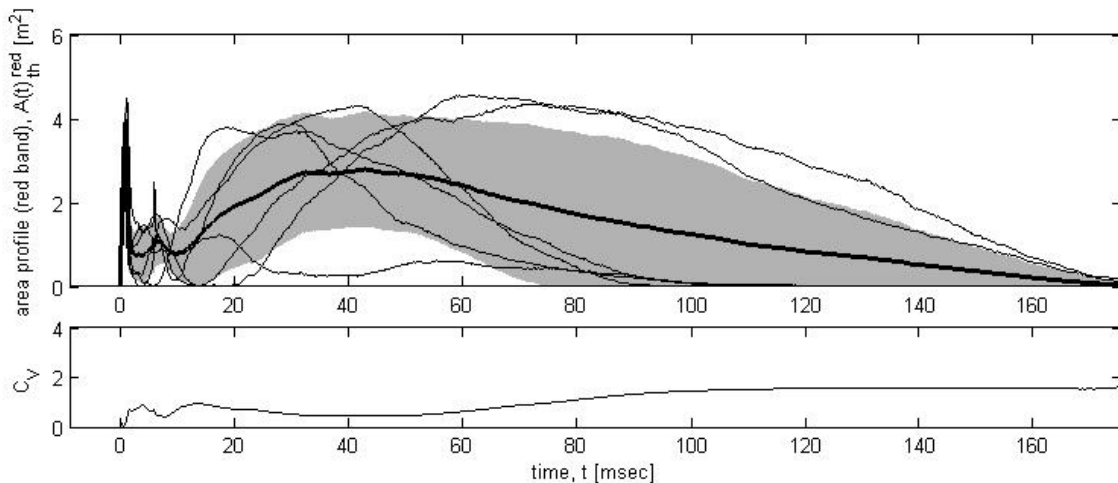


Figure 22: The area profiles for all erect 155mm TNT detonations are shown (thin line) with their mean (thick line) and standard deviation (shaded region) in the upper plot. The  $C_V$  as a function of time for the area profiles is shown on bottom. The mean  $C_V$  value for the six events of this type's feature is 1.22.



increase. This is evidenced in Figure 23 where the area profiles for all thirteen TNT events are plotted, again from the red band. The magnitude of the mean profile decreases for the afterburn fireball, but its shape remains nearly the same. The individual detonation profiles show that there is also as much variation in the afterburn area, time to afterburn peak, and duration as there was in the erect 155mm TNT. The conclusion that can be inferred is that the variability in the area profiles of a single type is nearly the same as it is for a group of munitions of the same composition, i.e. reproducibility is not affected by weight or orientation. The average  $C_V$  before the fireballs begin to decay (prior to ~40 milliseconds, on average) is approximately one, indicating that the variability in the area profile is of the same magnitude as the area itself.

The other explosives examined in this research were munitions containing Composition B. The red band area profiles for all Composition B detonation events are shown in Figure 24 (note that the timescale is different than for the TNT profiles). These detonations have a shape that is very reproducible – a sharp spike in area at detonation

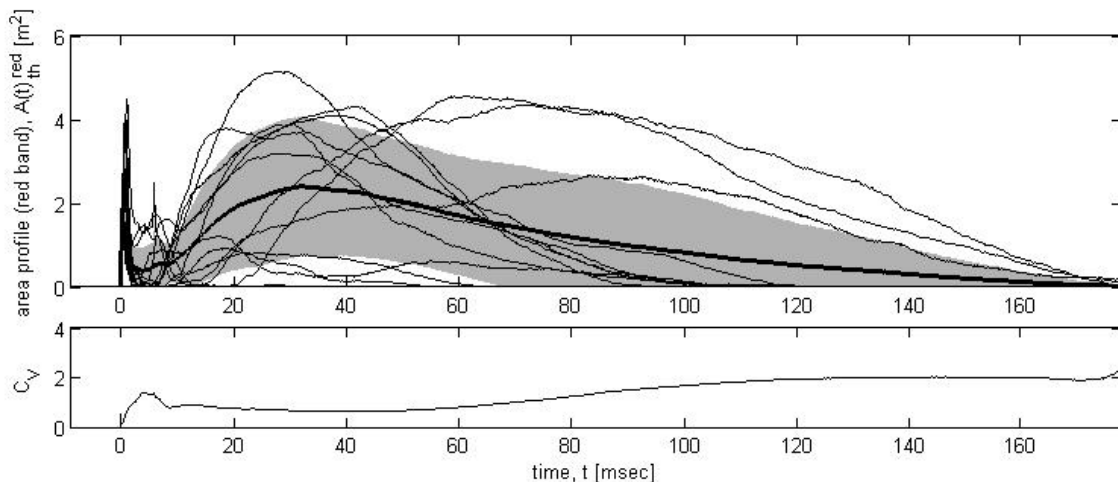


Figure 23: The area profiles for all TNT detonations are shown (thin line) with their mean (thick line) and standard deviation (shaded region) in the upper plot. The  $C_V$  as a function of time for the area profiles is shown on bottom. The mean  $C_V$  value for the thirteen events of this type's feature is 1.6.

and then a very small area in the afterburn. The reproducibility of the magnitudes and time to peak of the areas, however, is quite poor and has an average  $C_V$  of 1.58 (possibly due to obscuration, in which case a scaling factor accounting for this may improve reproducibility). Without correction, however, the Composition B detonations showed as much variability as the TNT detonations, indicating that the variability in observed area profiles was not a function of explosive composition in the Bronze Scorpio field tests.

Finally, although the result is easily anticipated, plotting the area profiles of all TNT and Composition B detonations shows greater variability for the combined group than for either single composition group alone. This is seen in Figure 25 where the average  $C_V$  value is 1.98. The least reproducible features are the area, time to peak, and duration of the afterburn fireball. Although the variability of the two groups of compositions is approximately the same, the reproducibility of the area profiles decreases when the two groups are combined into a single group. This is indicative that there are features in the area profile that show some distinguishability for the different explosive

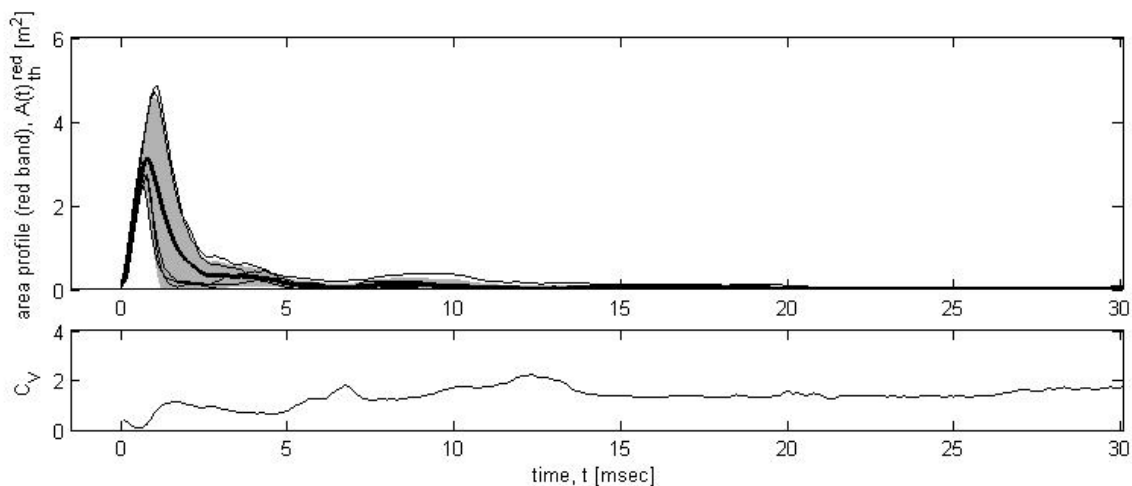


Figure 24: The area profiles for all Composition B detonations are shown (thin line) with their mean (thick line) and standard deviation (shaded region) in the upper plot. The  $C_V$  as a function of time for the area profiles is shown on bottom. The mean  $C_V$  value for the five events of this type's feature is 1.58.

compositions, and is a preview of characterizing distinguishability using the Fisher Ratio – the variability in the two groups are of the same magnitude, but the means of the groups are separated, leading to a greater variability when all feature values from both groups are examined as a single set.

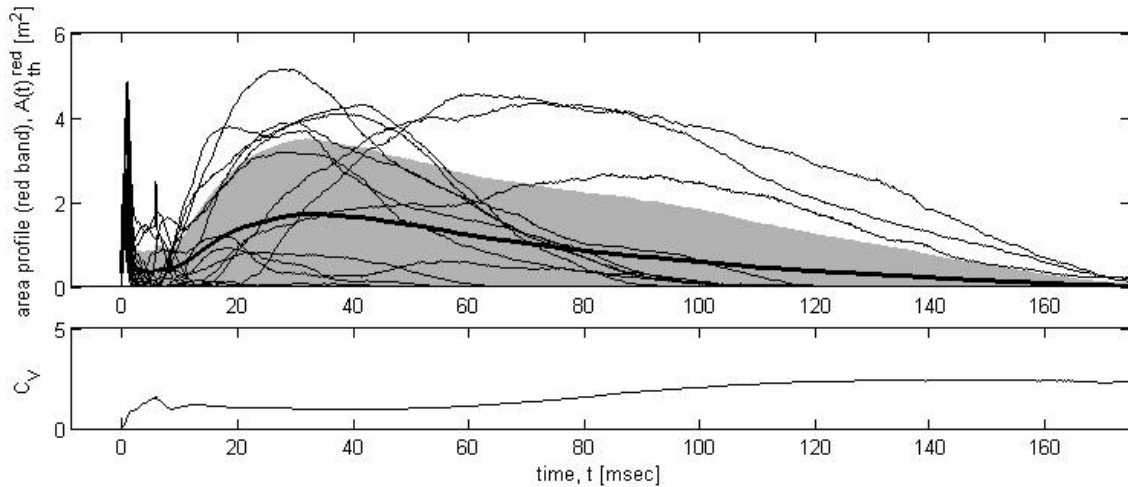


Figure 25: The area profiles for all TNT and Composition B detonations are shown (thin line) with their mean (thick line) and standard deviation (shaded region) in the upper plot. The  $C_V$  as a function of time for the area profiles is shown on bottom. The mean  $C_V$  value for the eighteen events of this type's feature is 1.98.

### Reproducibility of Fireball Features

There were an extremely large number of Coefficients of Variation calculated – nearly 500 for the afterburn fireball alone (all features for all groups of munitions in all bands) – so only those features that showed the least variation or that were particularly interesting are presented here. The three most reproducible features (and their  $C_V$  value) for each group of munitions, DTSS plume, and muzzle flash are presented in Table 11; in the case where the feature showed nearly the same reproducibility in the red, green, and blue bands, it was only listed for the band with the highest  $C_V$  value. The reproducible features tended to be the detonation area in one of the RGB bands (with blue providing

the most reproducibility by a small fraction),  $A_{det}^{blue}$ , the time to the peak detonation area in the RGB (with red typically providing the best reproducibility),  $t_{det}^{red}$ , or the duration of the afterburn in the near- and mid-infrared as characterized by the time to decay to the noise level,  $t_n^{NIR}$  and  $t_n^{MWIR}$ . For many of these features, the  $C_V$  is less than 0.2, signifying moderate reproducibility. Some of the groups even contain features with a  $C_V$  less than 0.1, indicating a very high degree of reproducibility.

Table 11: The most reproducible fireball features and the corresponding Coefficients of Variation are given for each group of combustion events.

group	types	feature	CV	feature	CV	feature	CV
1	155mm TNT erect	$A_{det}^{blue}$ *	0.142	$t_{det}^{red}$ *	0.156	$t_{50}^{MWIR}$	0.307
2	155mm TNT prone	$t_{det}^{blue}$	0.163	$A_{det}^{red}$	0.165	$A_{pk}^{MWIR}$	0.168
3	105mm TNT erect	$A_{det}^{blue}$ *	0.0658	$t_{pk}^{red}$	0.158	$t_{det}^{red}$	0.163
4	105mm TNT prone	$A_{pk}^{red}$	0.0819	$A_{det}^{blue}$ *	0.102	$t_n^{NIR}$	0.123
5	155mm TNT	$t_{det}^{red}$ *	0.165	$A_{det}^{green}$ *	0.23	$t_n^{NIR}$	0.356
6	105mm TNT	$A_{det}^{blue}$ *	0.0991	$t_{det}^{red}$ *	0.159	$t_{pk}^{green}$	0.264
7	all TNT	$t_{det}^{red}$ *	0.259	$t_n^{NIR}$	0.336	$t_n^{MWIR}$	0.432
8	2x155mm Comp. B	$A_t^{red}$	0.148	$t_{det}^{green}$	0.212	$t_{50}^{MWIR}$	0.247
9	all Comp. B	$A_{pk}^{NIR}$	0.136	$t_{pk}^{green}$	0.172	$A_t^{NIR}$	0.19
10	all TNT & Comp. B	$t_{det}^{red}$ *	0.243	$t_n^{NIR}$	0.355	$t_n^{MWIR}$	0.373
11	all munitions	$t_n^{NIR}$	0.349	$t_n^{MWIR}$	0.367	$t_{det}^{blue}$ *	0.379
12	DTSS	$A_t^{NIR}$	0.0908	$t_n^{NIR}$	0.145	$t_{10}^{NIR}$	0.18
13	conventional	$A_{pk}^{NIR}$	0.0747	$A_{sat}^{NIR}$	0.357		
14	novel	$A_{pk}^{NIR}$	0.079	$A_{sat}^{NIR}$	0.289		
15	novel FMJ	$A_{pk}^{NIR}$	0.0572	$A_{sat}^{NIR}$	0.955		
16	all muzzle flashes	$A_{pk}^{NIR}$	0.0745	$A_{sat}^{NIR}$	0.837		

\* feature had nearly the same  $C_V$  in the red, green, and blue bands

The most commonly reproducible feature across all groups of munitions was the time to the peak detonation area in the red band,  $t_{det}^{red}$ . The values of the features are shown by the thin bars in the upper plot of Figure 26, where each bar represents a single event from the group (thus the groups of multiple types had larger numbers of events). The wide bars indicate the mean time to the detonation's peak area for the group. The lower plot shows the  $C_V$  for the group. For all groups consisting of any combination of TNT and Composition B, the  $C_V$  is less than 0.25 (and is often lower) indicating that the time to the peak detonation area is a highly reproducible feature of munitions detonations in general. This was to be expected, however, because in the simple model of detonations, the detonation was assumed to be instantaneous. Although this assumption isn't true, it is often used because it captures one of the most basic aspects of detonations: the release of energy is so fast that it is effectively instantaneous and variations in munitions weight, orientation, and explosive composition become negligible. Further examination of this feature did little to aid in either phenomenology or classification because it merely verified a basic type-independent characteristic that is assumed in the simplest detonation models.

The next most common feature with high reproducibility is the magnitude of the detonation area in the blue band,  $A_{det}^{blue}$ . The areas of the individual events, the groups' means, and the  $C_V$  are shown in Figure 27. For groups consisting of a single type or multiple types of the same weight, the  $C_V$  is fairly low (ranging from 0.0658 to 0.165) and the feature is reproducible. When multiple weights or compositions are combined into one group, however, the variability increases. This is actually promising, because it

indicates that the feature may possibly be used for distinguishing between weights of TNT; when multiple weights are included in the group a high variability indicates a wide range of data, but since the variability decreases when only a single weight of munition is

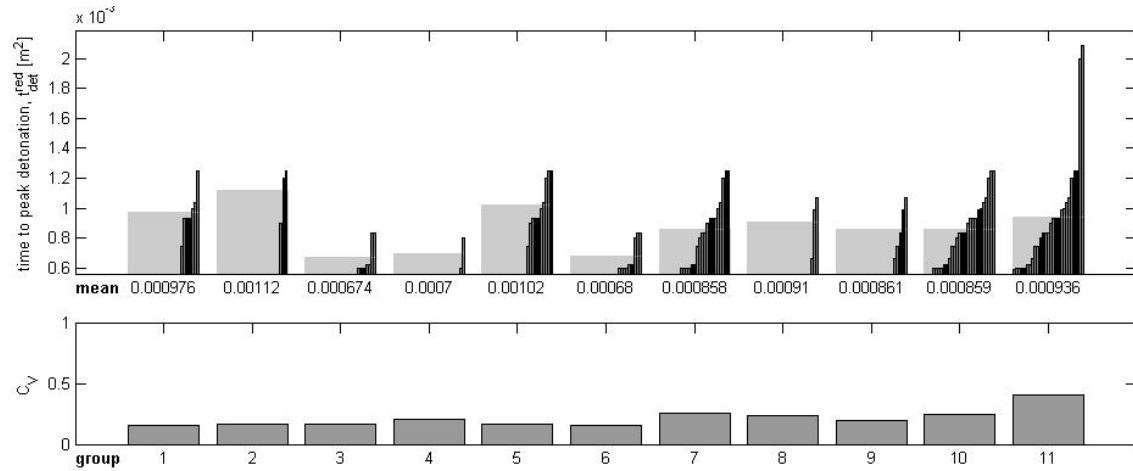


Figure 26: The time to the peak detonation area in the red band is shown for each event (thin bars) of the eleven munitions groups. The mean feature value is also shown for each group (wide bars) and the value is indicated below the top plot. The bottom plot shows the coefficient of variation for the feature in each group.  $t_{det}^{red}$  is a very reproducible feature for all groups, indicating it may be a feature common to explosives in general.

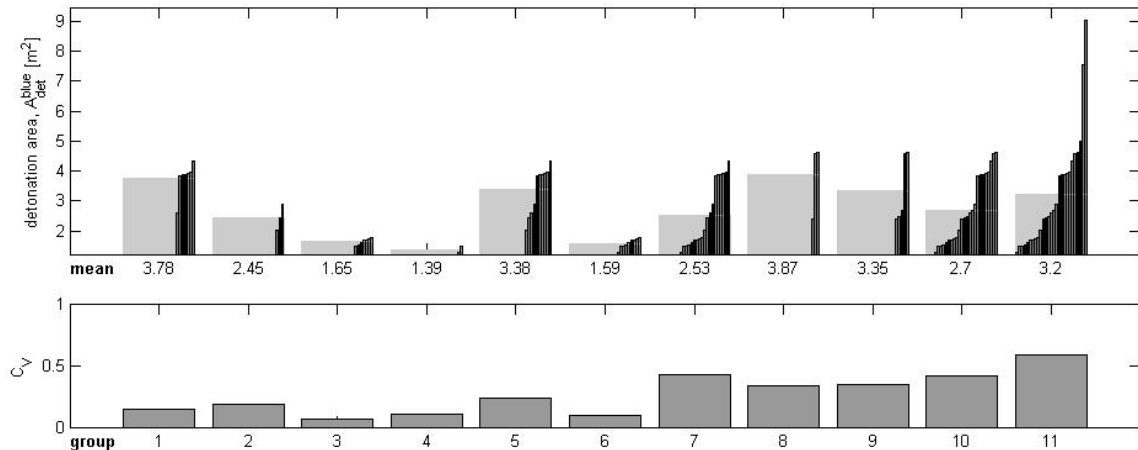


Figure 27: The peak detonation area in the blue band is shown for each event of the eleven munitions groups (thin bars). The mean feature value is also shown for each group (wide bars) and the value is indicated below the top plot. The bottom plot shows the coefficient of variation for the feature in each group. For TNT,  $A_{det}^{blue}$  shows correlation for a single weight and may be a good feature for classification.

examined, it means that the two weights' values are clustered. Clearly the size of the detonation can be related to the amount of material detonated. This is almost trivial, however, since a greater mass of explosive contains more total energy and when released instantaneously should result in stronger emissions. The extent of how useful the feature is for classification depends on how much the distributions overlap, which is examined in the *Distinguishability of Explosive Munitions* section.

The final features that are presented are the duration of the detonation event (afterburn fireball) in the NIR and MWIR. These two features show a much lower reproducibility than the two previously discussed, as can be seen in Figure 28 and Figure 29. The  $C_V$  across all groups in both bands is fairly high (with prone 105mm TNT in the NIR and prone 155mm TNT in the MWIR being the exceptions). This alone merely indicates that there is variation in the duration of the fireball in each group, but the fact that the  $C_V$  does not increase as more munitions types are included indicates that the variability in the durations for individual events (or types of events) is greater than the differences in durations between types. Physically, this may mean that the longevity of the afterburn fireball is less dependent on the weight and composition of the explosive than on some other factor not examined here.

To be complete, a brief comment on the DTSS and Muzzle Flash features is warranted. These two classes of combustion events both contain highly reproducible features that may be used as descriptors of their respective types. The most reproducible feature of the DTSS plume is its total integrated area,  $A_t^{NIR}$ , and its duration,  $t_n^{NIR}$ , both in the NIR. Both of these features have a  $C_V$  less than 0.15, indicating a high degree of reproducibility. The muzzle flashes have only a single highly reproducible extracted

feature: the total area of the flash in the NIR,  $A_{pk}^{NIR}$ . This feature is characteristic of all muzzle flashes, independent of round type. In addition, the longevity of the flash, which was not an extracted feature but is nonetheless useful for characterizing the combustion event, is less than 2 milliseconds for all flashes. These features are used later to demonstrate the feasibility of distinguishing between classes of combustion events.

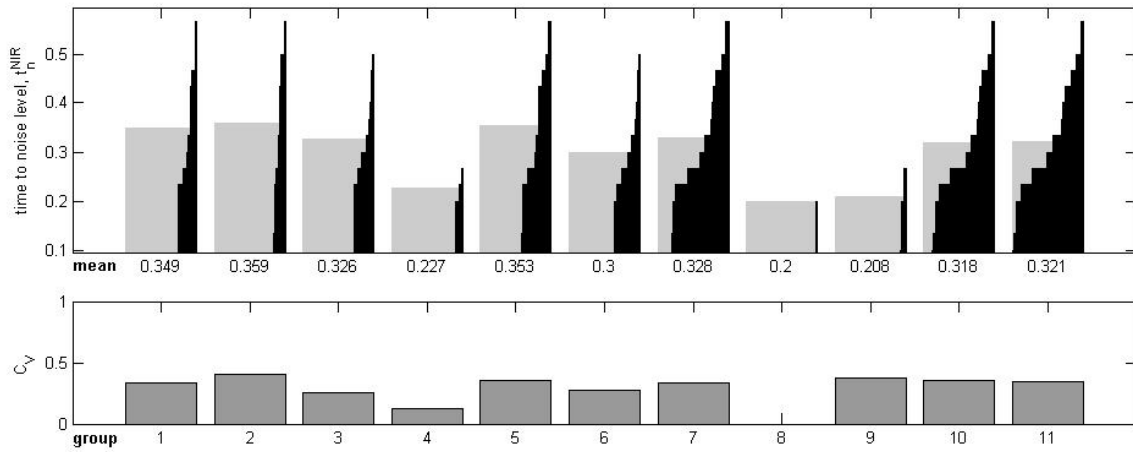


Figure 28: The time required for the fireball’s area to fall below the noise level in the NIR is shown for each event of the eleven munitions groups (thin bars). The mean feature value is also shown for each group (wide bars) and the value is indicated below the top plot. The bottom plot shows the coefficient of variation for the feature in each group.

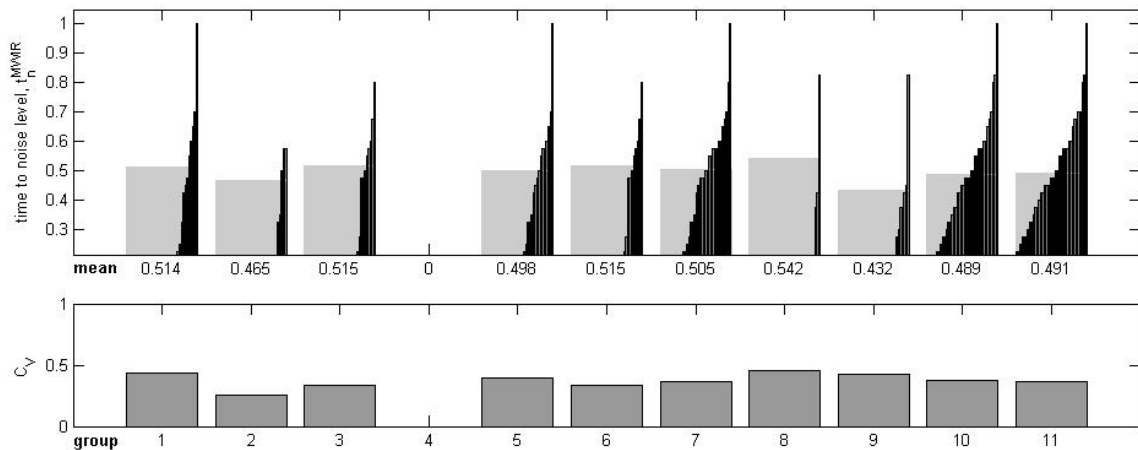


Figure 29: The time required for the fireball’s area to fall below the noise level in the MWIR is shown for each event of the eleven munitions groups (thin bars). The mean feature value is also shown for each group (wide bars) and the value is indicated below the top plot. The bottom plot shows the coefficient of variation for the feature in each group.



## Shockwave Fits

All of the features extracted for the shockwave are dependent on the function that was used to model the propagation of the shock over time. Because of this, understanding which fit functions provide the best representation of the experimental data guides the analysis of which features are most directly related to the actual shockwave. The three forms of the shock model are shown in Figure 30 for an erect 155mm TNT detonation, along with the observed positions at each time. All three models were fit to the Phantom data ( $t < 100$  msec, which encompasses the near-field, mid-field, and the beginning of the far-field), and show excellent agreement ( $\overline{r^2} > 0.99$ ); the modified shock and the shock 350 model are slightly more accurate than the basic shock model. The late-time data point and the fits' proximity to it are shown in the upper right region of the figure. This point was not used in determining the best fit, but was reserved to verify the predictions of the fit models at a time several orders of magnitude greater than the fit data. It is not surprising that the shock 350 model gives excellent agreement at late times, because this model had the final velocity of the shockwave fixed at 350 m/s (which would bring the fit function to within the error bounds of the data point for a large range of  $a$  and  $b$  fit parameters). Of much greater interest is that the modified shock model so accurately predicted the late time position of the shockwave. This is notable since the  $a$ ,  $b$ , and  $c$  fit parameters were all determined by the least-squares fit to the shockwave's position for times less than 50 milliseconds, yet were able to predict the position at  $\sim 3$ . It makes sense that the modified shock model provides a good fit to the early-time data, since it has three fit parameters for smoothly varying data. To provide such an accurate extrapolation at a time nearly two orders of magnitude later, however, indicates that the

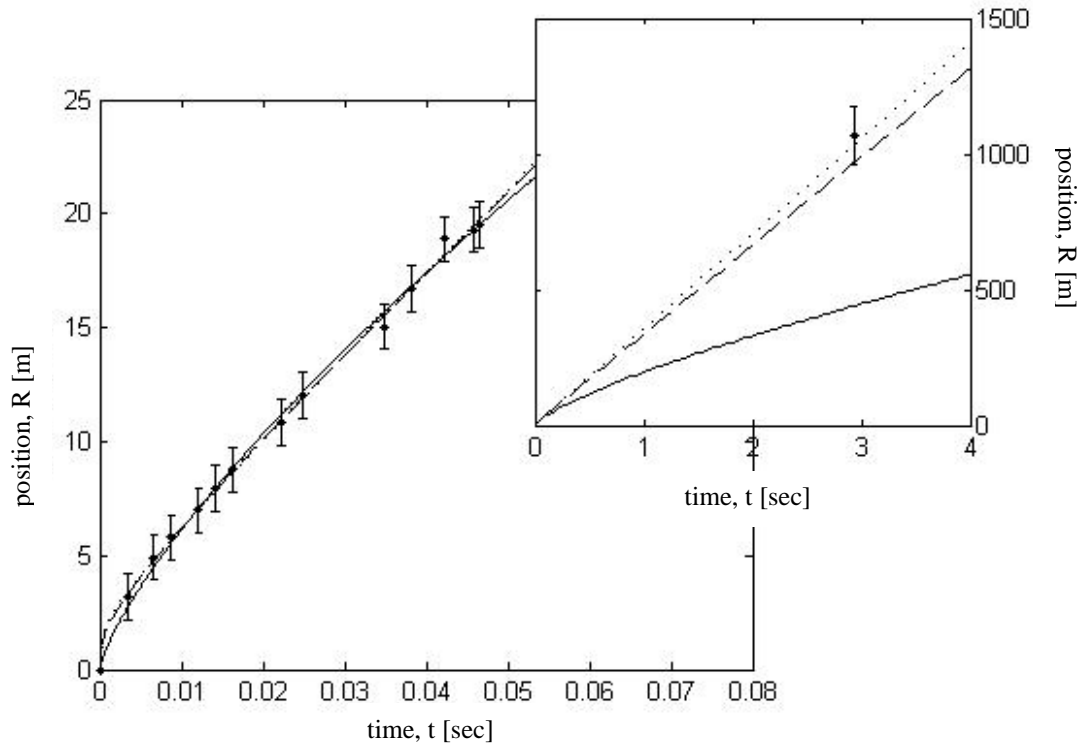


Figure 30: Position of the shockfront (•) is shown with its uncertainty for an erect 155mm TNT detonation. The shock fit (solid line), modified shock fit (dashed line), and shock 350 fit (dotted line) are also shown. The functions were fit to the early-time data (lower left) with the late-time data point used to evaluate the fits in the far-field (upper right).

model is representative of the shockwave physics over a much wider range of fields, and that the properties of the shock at early times are predictive of late-time behavior.

Figure 31 shows the fits of the three drag models to the same data. As with the shock models, the late-time data point was ignored for fitting purposes and used to evaluate which fits are accurate in the far-field. As expected, the drag model does not perform well at distances extending beyond the mid-field. Surprisingly, however, the basic drag model has the lowest quality of fit ( $\overline{r^2} = 0.989$  versus  $\overline{r^2} > 0.99$  for all other models) in the near- and mid-field region as well. The drag model is often presented in the literature as an excellent fit to shock expansions, and so its inaccuracy here is troublesome. The most probable explanation is that the data include points in the far-

field (beyond  $\sim 0.015$  seconds) which the model was not intended to account for. These points were included because initially the entire life of the fireball was to be examined in conjunction with the shockwave. This required extending the models into the far-field, but the basic models were kept as a reference for the modifications in the mid-field. It was only during the course of analysis that it was determined the most pertinent features of the detonation occur at very early times.

The modified drag and drag 350 models, however, give superior fits in all regions. Once again, it is remarkable that the fits provide such an accurate prediction of late-time behavior of the shockwave based on data that were collected at times two orders of

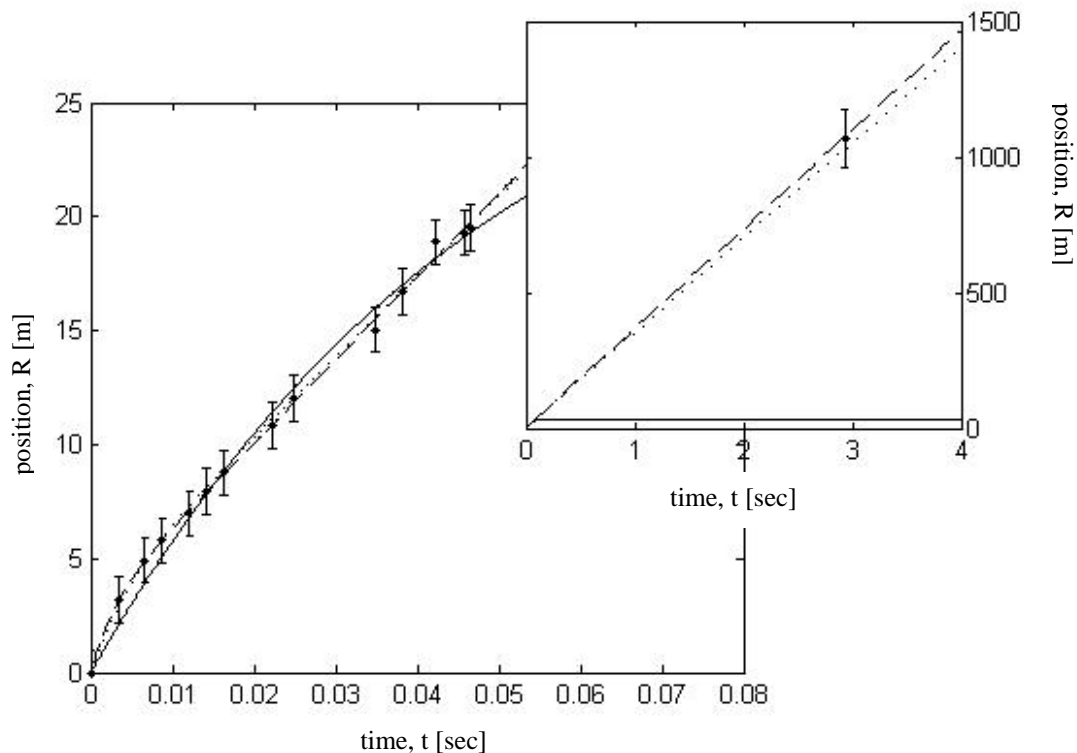


Figure 31: Position of the shockfront (•) is shown with its uncertainty for an erect 155mm TNT detonation. The drag fit (solid line), modified drag fit (dashed line), and drag 350 fit (dotted line) are also shown. The functions were fit to the early-time data (lower left) with the late-time data point used to evaluate the fits in the far-field (upper right).

magnitude prior. This is most likely due to the fact that although the timescales of the fit data are so small, the near- and mid-fields are so physically short that the fit data encompass the far-field as well, and thus the fit parameters capture the far-field behavior. This is useful to know, since if any features depend on field, it will be necessary to know on what timescales to look for them.

A quantitative look at the fits for all of the events examined is shown in Figure 32. In the upper plot of the figure, the coefficient of determination,  $r^2$ , for the quality of the fit to the data is shown for all events and all models. Clearly, all models provide very good agreement with the experimentally observed data at early times. Although good, the basic shock and drag models give slightly poorer results than the others, which can be accounted for by the fact that they are based on mid-field assumptions and the data used extends into the far-field. At late-times, however, there is no question that the modified drag, modified shock, drag 350, and shock 350 fit functions are superior. This is seen in the lower plot of the figure where the deviation of the shockwave's actual position from its predicted position is shown. The shock and drag models are nearly useless in this region, having deviations nearly as large as the shock's position itself. The models that extend into the far-field, however, all predict values that are within the uncertainty in the data point.

Due to the lack of significant improvement in the fits by using three fit parameters (modified drag and shock models) instead of only two (drag 350 and shock 350 models), the  $c$  fit parameter should be set to the ambient speed of sound so that artificial improvement is not introduced by having an additional fit parameter. This is because the fit parameter physically represents the speed of the shockwave when it has transitioned to

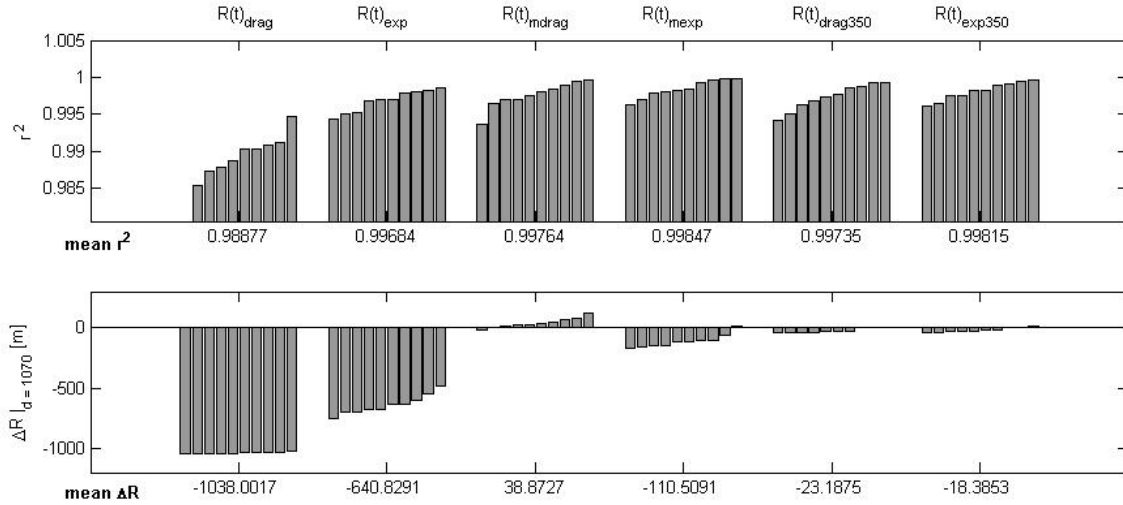


Figure 32: The coefficient of determination calculated from the near, mid, and early far-field shockwave positions, is shown for each fit function and all events (top). The deviation of the fit from the far-field data point is also shown (below). All of the fits show good correlation in early-time data, but in the far-field the shock 350 and drag 350 models show the best agreement with observations.

an acoustic wave (in the far-field). Since the ambient speed of sound is nearly constant, using a fixed value for  $c$  that is near  $c_0$  will result in a fit that differs inappreciably from leaving  $c$  free and allowing it to approach  $c_0$  as a result of least-square fitting. This can be seen in the upper plot of Figure 33, where the least-squares fit value of  $c$  is shown for each event of each munitions type for the modified drag (dark bars) and modified shock (light bars) models. The variation in the fit parameter is shown in the lower plot, which for TNT is very reproducible (types 1-4) in both models but for Composition B is only strongly reproducible for the modified drag model.

The modified drag model consistently overestimates the ambient speed of sound (the range of which is represented by the shaded region) while the modified shock model underestimates it. This result further indicates that these fit functions are not ideal for two reasons. The first, and perhaps most important for understanding the physics behind the fits, is that the fit functions are based on simple models that do not capture all of the

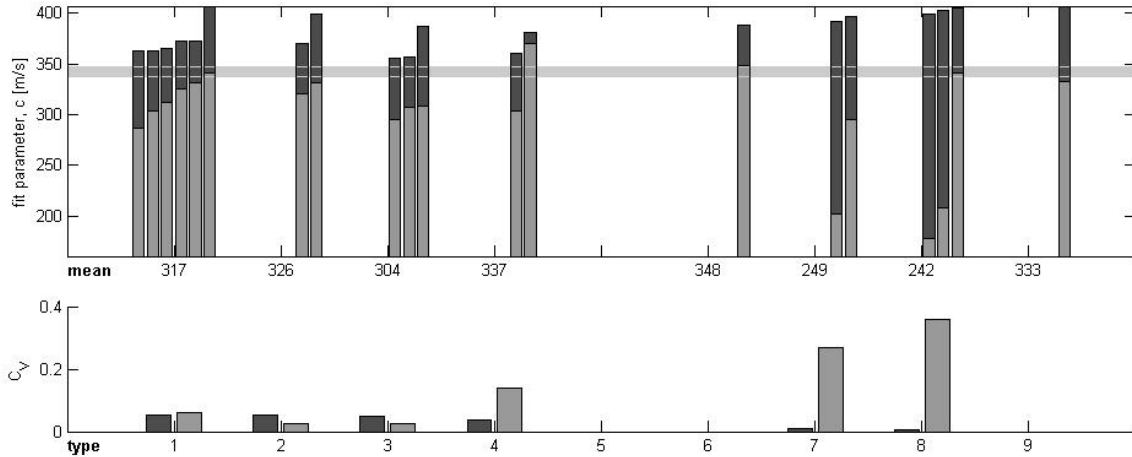


Figure 33: The speed of sound fit parameter for the modified drag (dark bars) and modified shock (light bars) fit functions are plotted for each event of each type in the upper plot. The shaded region was the average range of speeds of sound (based on the temperature) for the Bronze Scorpio field tests. On the lower plot, the Coefficients of Variation are plotted for the fit parameter by type. The modified drag best-fit speed of sound was consistently high whereas the modified shock best-fit speed of sound was consistently low.

complex thermodynamic and kinetic mechanisms involved in detonations and shockwave propagation. A number of simplifying assumptions were used, including a constant ratio of specific heats, an instantaneous release of energy, and a completely spherical shockwave. The second reason for the non-ideality of the fits is that they are based on data collected primarily in the near- and mid-fields but the speed of sound fit parameter,  $c$ , is most strongly dependent on far-field data. These reasons, combined with the uncertainty in the measurements, yielded the range of values for  $c$  that are given above. Even so, all of the values are fairly close to the actual speed of sound, and better still, provide a model of the shockwave that very accurately predicts its position in all fields.

### Reproducibility and Physicality of Shockwave Fit Parameters

To understand how the fit parameters translated to physical quantities, the accuracy and precision with which they represented the physical parameters needed to be

known. It was already seen that the speed of sound can be fixed (instead of being left a free fit parameter) without loss of fit quality. The remaining fit parameters from all models,  $a$  and  $b$ , are also related to physical characteristics of the shockwave.

Theoretically,  $a^{drag} \equiv R_{max}$  is the maximum radius of the shock, or rather is the maximum radius of the shock before the shock's pressure reaches ambient pressure – this is only an accurate description when the final speed of the shock is zero. Otherwise the shock will have propagated an additional distance  $c_0 t$  before its pressure reaches ambient, in which case,  $a^{mdrag}$  represents some other characteristic radius of the shock. In both the basic and modified drag models,  $b = \beta$ , which determines how quickly the shockwave will decay to an acoustic wave and is a measure of the viscosity of the atmosphere relative to the shock.

The meaning of the shock model's fit parameters is slightly more complex. The fit parameter  $a = \xi_0 (E_D / \rho_0)^{1/5}$  contains information about the detonation's geometry (in  $\xi_0$ ); energy release,  $E_D$ ; and the initial density of the explosive,  $\rho_0$ . All of these are dependent on munitions type, and thus determining  $a$ 's relationship to particular munitions is not trivial, especially with the known variability in the detonations. The  $b$  fit parameter is theoretically fixed at 2/5 from the model's derivation (for units to work out correctly), and so variation in this is most likely an indication of the non-ideality of the detonation and an imperfect fit to the data.

Since all of these fit parameters have some physical basis and can be used as extracted features, their reproducibility guides which ones may be useful for phenomenology or classification. Table 12 presents the three most reproducible features

from each group of munitions, along with their  $C_V$  (the values of all fit parameters and their uncertainties are shown in Appendix 2 for all groups). The  $c$  fit parameter in the modified drag model tends to be one of the most reproducible features for all groups, reinforcing that it represents a physical aspect of detonations in general. Other common, highly reproducible features include the  $b$  fit parameter from the shock model,  $b^{\text{exp}}$ , and the  $a$  fit parameter from the drag 350 model,  $a^{\text{drag350}}$ .

The characteristic radius fit parameter for the drag 350 model,  $a^{\text{drag350}}$ , shows very little variation for groups consisting of only 105mm TNT ( $C_V < 0.04$ ). Slightly more variation is introduced when 155mm TNT, Composition B, and groups of the different weights and compositions are examined, yet the  $C_V$  consistently remains less than 0.2. This is indicative of a highly reproducible feature for all groups, with the possibility for classification because the reproducibility decreases slightly when different weights and compounds are grouped together. Whether this feature correlates to features of the

Table 12: The most reproducible shockwave fit parameters and the corresponding Coefficients of Variation are given for each group of munitions.

group	types	feature	CV	feature	CV	feature	CV
1	155mm TNT erect	$c^{\text{mdrag}}$	0.0523	$c^{\text{mexp}}$	0.0626	$b^{\text{exp}}$	0.0687
2	155mm TNT prone	$c^{\text{mexp}}$	0.0239	$b^{\text{exp}}$	0.0444	$c^{\text{mdrag}}$	0.0533
3	105mm TNT erect	$c^{\text{mexp}}$	0.0239	$b^{\text{exp}}$	0.0239	$b^{\text{mexp}}$	0.0284
4	105mm TNT prone	$a^{\text{drag350}}$	0.0263	$b^{\text{exp}}$	0.031	$c^{\text{mdrag}}$	0.0392
5	155mm TNT	$c^{\text{mdrag}}$	0.0499	$c^{\text{mexp}}$	0.055	$b^{\text{exp}}$	0.0624
6	105mm TNT	$a^{\text{drag350}}$	0.036	$c^{\text{mdrag}}$	0.0396	$b^{\text{exp}}$	0.0576
7	all TNT	$c^{\text{mdrag}}$	0.0465	$b^{\text{exp}}$	0.0672	$c^{\text{mexp}}$	0.0692
8	2x155mm Comp. B	$c^{\text{mdrag}}$	0.00754	$b^{\text{exp}}$	0.0145	$a^{\text{exp}}$	0.0428
9	all Comp. B	$c^{\text{mdrag}}$	0.0127	$b^{\text{exp}}$	0.0664	$a^{\text{drag350}}$	0.0833
10	all TNT & Comp. B	$c^{\text{mdrag}}$	0.0494	$b^{\text{exp}}$	0.0756	$a^{\text{drag350}}$	0.0961
11	all munitions	$c^{\text{mdrag}}$	0.0542	$b^{\text{exp}}$	0.0889	$c^{\text{mexp}}$	0.0932



munitions type will be shown in the *Feature Correlation* section but can be previewed by examining the feature values and the group means in the upper plot of Figure 34. It is clear that groups of 155mm TNT have a much larger  $a^{drag350}$  value than those of 105mm TNT. Likewise, the Composition B groups have a value of  $a^{drag350}$  that tends to fall in the middle. What this characteristic radius describes in the modified model is not known, but it is identifiable as a reproducible characteristic of the munitions types.

The other common, reproducible feature from the fit functions is the exponent the time was raised to in the shock model,  $b^{exp}$ . Theoretically, this fit parameter should have a value of 0.4 but, as indicated in Figure 35, typical fit values were in the 0.64~0.8 range. The  $C_V$  for all groups is less than 0.1, indicating excellent reproducibility. This is not unexpected, however, since according to the model, the value should be a constant that is completely independent of munition characteristics. As with the  $c$  fit parameter, the

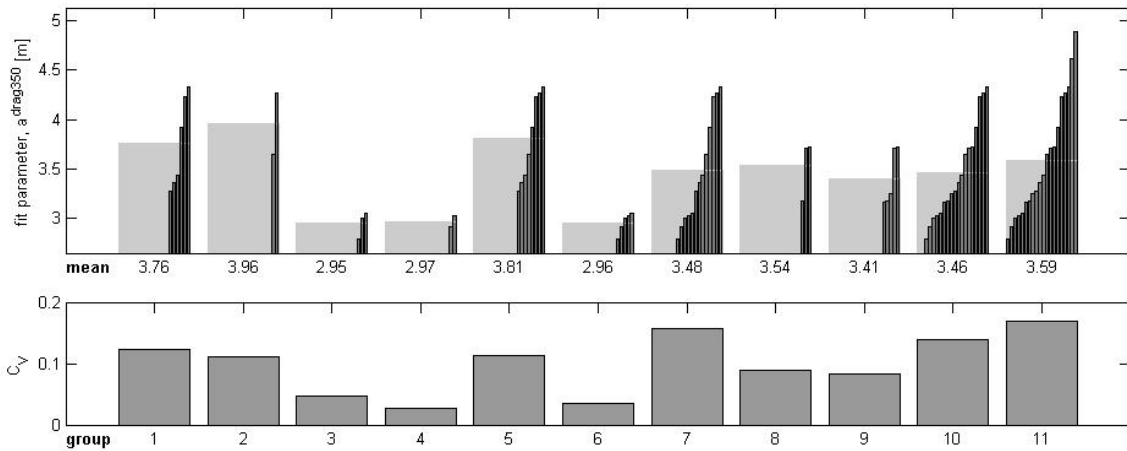


Figure 34: The characteristic radius from the drag 350 fit function is shown for each event of the eleven munitions groups (thin bars). The mean feature value is also shown for each group (wide bars) and the value is indicated below the top plot. The bottom plot shows the coefficient of variation for the feature in each group. The reproducibility of  $a^{drag350}$  for munitions types indicates that it is representative of a feature of the munitions, and perhaps will be useful in classification.

deviation from the expected value is evidence of the flaws in the model due to ideal detonation assumptions and using a mid-field model for data that extend into the far-field. Values closer to those expected were obtained with the modified shock model ( $b^{mexp}$  ranged from 0.3~0.43). The  $C_V$  value did increase (to a small extent) for groups of multiple types of munitions, indicating that although this feature is model dependent and should be type-independent, it may in fact provide distinguishability.

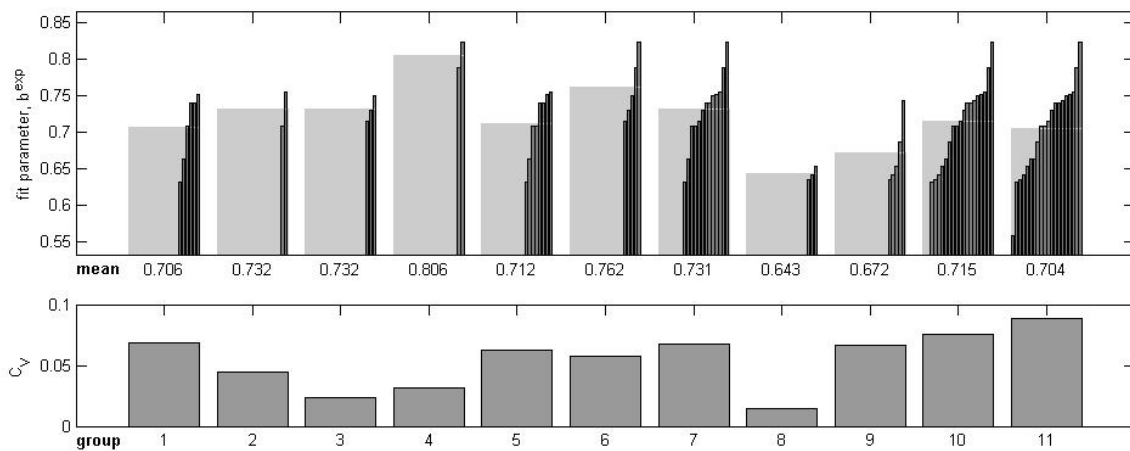


Figure 35: The time exponent fit parameter from the explosive fit function is shown for each event of the eleven munitions groups (thin bars). The mean feature value is also shown for each group (wide bars) and the value is indicated below the top plot. The bottom plot shows the coefficient of variation for the feature in each group. This feature is very reproducible for all groups yet increases for multiple munitions groups, indicating potential for classification.

### Reproducibility of Temporal Shockwave Features

Despite the existence of only five time-dependent physical quantities describing the shockwave, each of these quantities was calculated using the six fit functions with two thousand time steps each, yielding an exceptionally large number (60,000) of  $C_V$  values to examine. As with the fireball features, not all of the shockwave features were examined; only those that showed the best reproducibility or are of interest are shown.

Table 13 shows the three most reproducible features in each group (as indicated by the  $C_V$  value) and the time at which these features occurred. Because the shockwave decays to an acoustic wave in the far-field, the analysis of reproducible features was limited to the near- and mid-fields; since there is no hard boundary between the mid- and far-fields and the boundary region itself depends on munitions characteristics (detonation energy, initial density, etc.), the near- and mid-fields were approximated as the time of detonation until 30 milliseconds; in this time the shock propagated an average of 5-15 meters.

By far the most reproducible feature in this early-time region is the Mach number at average times from 10~15 milliseconds for all models. This is not surprising for two reasons. The first is that the detonation velocity is similar for all munitions types examined (6900-7800 m/s); it should be noted that in this early-time region, the speed of sound is negligible and its ambient value does not affect the Mach number of the

Table 13: The most reproducible shockwave features in the near-and mid-fields ( $0 \leq t \leq 30$  msec) and the corresponding Coefficients of Variation are given for each group of munitions. The time in milliseconds where the  $C_V$  was a minimum for the feature is indicated.

#	types	feature	CV	feature	CV	feature	CV
1	155mm TNT erect	$M^{mexp}  _{t=19.7}$	0.0194	$M^{mdrag}  _{t=9.4}$	0.0349	$R^{exp}  _{t=26.3}$	0.0417
2	155mm TNT prone	$R^{drag}  _{t=25.1}$	$4 \times 10^{-5}$	$R^{exp}  _{t=18.3}$	$5 \times 10^{-5}$	$M^{drag}  _{t=11.4}$	$7 \times 10^{-5}$
3	105mm TNT erect	$M^{exp}  _{t=11.6}$	$1 \times 10^{-3}$	$M^{drag}  _{t=15.7}$	0.001	$M^{mexp}  _{t=12.1}$	0.0013
4	105mm TNT prone	$f^{drag}  _{t=24.2}$	$2 \times 10^{-6}$	$R^{drag350}  _{t=18.6}$	$1 \times 10^{-5}$	$R^{exp350}  _{t=23.1}$	$2 \times 10^{-5}$
5	155mm TNT	$M^{mexp}  _{t=20.3}$	0.029	$R^{exp}  _{t=24.7}$	0.0357	$M^{mdrag}  _{t=9.4}$	0.0362
6	105mm TNT	$M^{exp}  _{t=10.3}$	0.0023	$M^{drag}  _{t=16.9}$	0.0025	$P_1^{exp}  _{t=10.3}$	0.005
7	all TNT	$M^{mexp}  _{t=17.4}$	0.031	$M^{mdrag}  _{t=10.3}$	0.0363	$M^{exp}  _{t=9.9}$	0.0399
8	2x155mm CompB	$M^{mexp}  _{t=14.6}$	$8 \times 10^{-4}$	$P_1^{mexp}  _{t=14.6}$	0.0019	$M^{drag}  _{t=10.1}$	0.0034
9	all Comp. B	$M^{mexp}  _{t=14.9}$	0.0057	$M^{mdrag}  _{t=12.5}$	0.0111	$P_1^{mexp}  _{t=14.9}$	0.0127
10	all TNT & CompB	$M^{mexp}  _{t=15.6}$	0.0264	$M^{mdrag}  _{t=9.8}$	0.034	$M^{exp}  _{t=7.6}$	0.0392
11	all munitions	$M^{mexp}  _{t=15.3}$	0.0285	$M^{mdrag}  _{t=9.4}$	0.0365	$M^{drag}  _{t=9.0}$	0.0615

shockwave to any appreciable extent – the shock velocity in this region is determined by the initial velocity of the shock as it breaches the munition’s casing and then by the near- and mid-field expansion models. Second, because all of the fit functions have excellent agreement with the observed data, all of the physical quantities derived from the fits have roughly the same variability. Thus, for the Mach number (and the other physical quantities), the functional form of the fit matters little in this early-time region. For this reason, only a single fit function is used to examine this region for the remainder of this section. The modified drag model was chosen because it has very good reproducibility in the near- and mid-fields, shows the best reproducibility in the far-field (although far field  $C_V$ s were not examined, seeing the behavior of the shock in this region is useful), and has a theoretical foundation.

The mean and standard deviation of the Mach number as a function of time,  $M(t)$ , for all TNT and Composition B is shown in Figure 36 for the first 15 seconds of the early-time region. It is clear that even for the wide range of munitions types included (two weights, two orientations, and two explosive compounds) the velocity of the shock approaches a uniform value very quickly – within the first five milliseconds (with the  $C_V$  decreasing by an order of magnitude over this range). By ten milliseconds, the Mach number has nearly approached unity, indicating that the shockwave has almost entirely transitioned to an acoustic wave. This is seen in Figure 37 where the pressure is plotted in the early-time region and shows much the same reproducibility as the Mach number profile. The pressure profile,  $p_I(t)$ , confirms that the shockwave transitions to an acoustic wave very quickly (~10 msec) despite the several munitions types included. The only place the munitions’ characteristics appear important is in the first 2-3 milliseconds of the

expansion, indicated by the  $C_V$  ranging from 0.5 to greater than 2; another possibility is that the physical quantities of the shock are highly variable immediately after detonation, independent of munition characteristics.

The remaining physical quantity determined by the fit functions is the energy of detonation,  $E_D(t)$ ; the efficiency of the detonation,  $f(t)$ , is merely  $E_D(t)$  scaled by the theoretically calculated energy of detonation,  $E_D$ , and thus the description of  $E_D(t)$  also

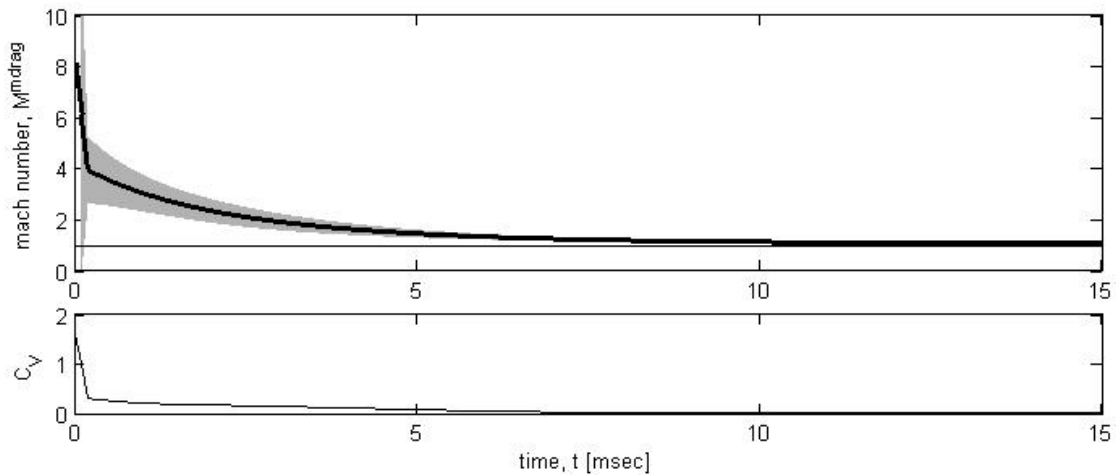


Figure 36: The mean Mach number as a function of time (solid line) with the corresponding standard deviation (shaded region) for the modified drag fit to the shockwave is shown in the upper plot for all TNT and Composition B events. The lower plot shows the coefficient of variation for each time step.

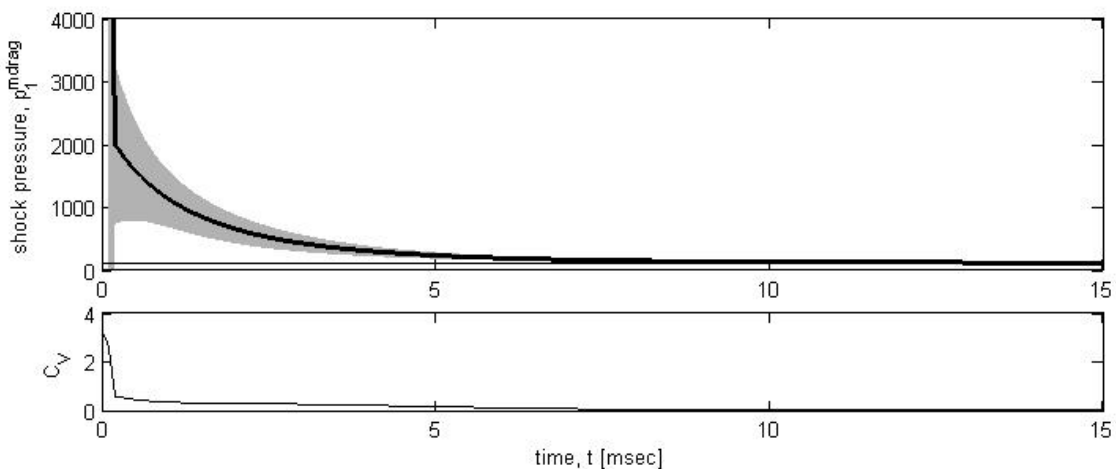


Figure 37: The mean shock pressure as a function of time (solid line) with the corresponding standard deviation (shaded region) for the modified drag fit to the shockwave is shown in the upper plot for all TNT and Composition B events. The lower plot shows the coefficient of variation for each time step.

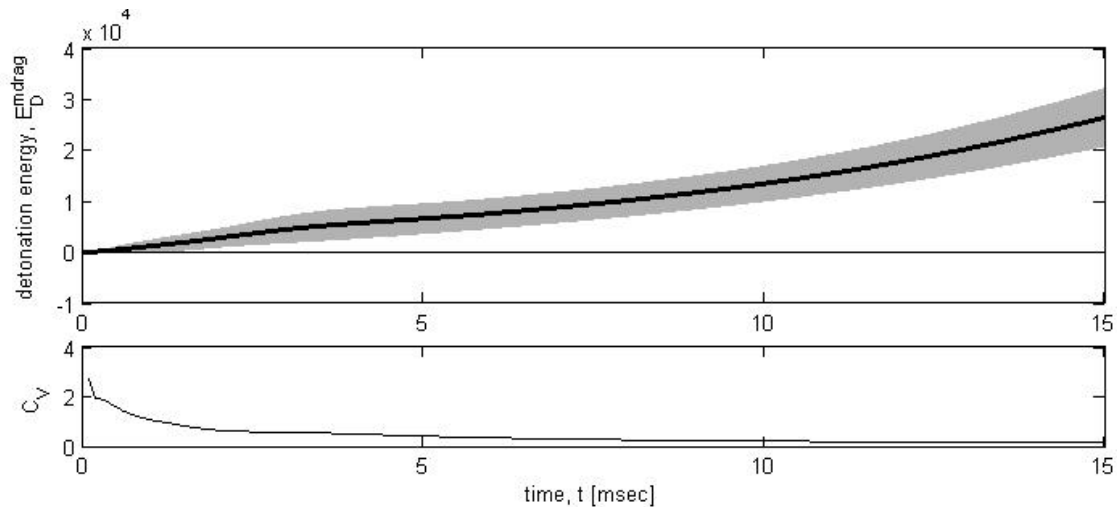


Figure 38: The mean detonation energy predicted at each time step (solid line) with the corresponding standard deviation (shaded region) for the modified drag fit to the shockwave is shown in the upper plot for all TNT and Composition B events. The lower plot shows the coefficient of variation for each time step.

pertains to it. The mean and standard deviation of  $E_D(t)$  is shown in Figure 38 for all TNT and Composition B events, but unlike the Mach number and pressure profiles, it shows greater variability for upwards of 10 milliseconds. This is expected, because the energy released depends directly on the composition and weight of the explosive.

If the assumptions of an ideal detonation were true,  $E_D(t)$  would be a constant. Because energy continues to be released as the shockwave propagates (in the continued burning of the afterburn fireball), however, the apparent initial release of energy continues to increase.  $E_D(t)$  might better be thought of as the total energy released by a time,  $t$ , even though its derivation relates all of this to an instantaneous energy released at the time of detonation,  $t = 0$ . The result of this is that the shockwave is sustained at higher pressures for longer than it normally would be (deduced because  $E_D$  is determined directly from the shock's overpressure). As the pressure of the shock approaches ambient pressure, however, the increase in the apparent energy released becomes more uncertain; this is because small deviations in shock pressure translate to increasingly large

deviations in scaled distance, from which detonation energy is calculated. Thus, the only values of  $E_D(t)$  that should be used as actual estimates of energy are those where the shock is still in fact a shockwave, i.e. at times less than ~5 milliseconds.

### Distinguishability of Combustion Classes and Simple Types

Having determined the most reproducible features of the fireball and shockwave, the next step was to evaluate these features for their classification potential.

Distinguishing between combustion events of the same class (i.e. specific munitions types from one another) is a complex problem that often requires robust techniques. The simpler problem is distinguishing between classes of combustion events. Distinguishing between explosive munition detonations, DTSS plumes, and muzzle flashes served as an introduction because they contained similar features with largely different values. These features and their separability (quantized by the Fisher Ratio) for each combination of combustion classes are presented in Table 14.

Table 14: The Fisher Ratios for all features used in comparing detonations, DTSS plumes, and muzzle flashes are shown for each combination of combustion event classes.

Feature	Group A #	Group A Class	Group #	Group B Class	FR
$A_{pk}^{NIR}$	11	all munitions	12	DTSS	1.03
$t_n^{NIR}$	11	all munitions	12	DTSS	41.06
$t_{10}^{NIR}$	11	all munitions	12	DTSS	27.88
$t_{50}^{NIR}$	11	all munitions	12	DTSS	0.16
$A_{pk}^{NIR}$	11	all munitions	16	all muzzle flashes	1.29
$t_n^{NIR}$	11	all munitions	16	all muzzle flashes	2.30
$A_{pk}^{NIR}$	12	DTSS	16	all muzzle flashes	10.08
$t_n^{NIR}$	12	DTSS	16	all muzzle flashes	47.57

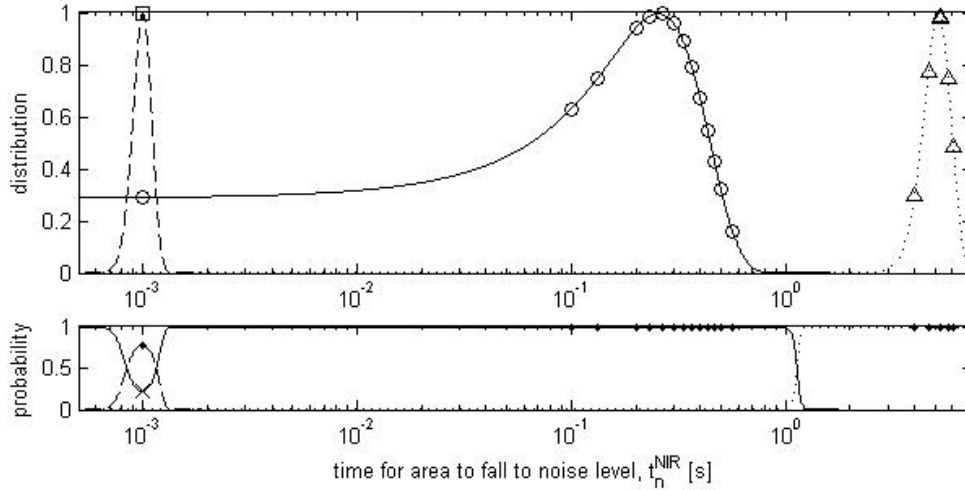


Figure 39: The time required for the area to fall to the noise level (in the NIR) is plotted for all detonations (○) DTSS plumes (△) and muzzle flashes (□). The upper plot shows the data points assuming normal distributions (detonations are represented by the solid line, plumes by the dotted line, and muzzle flashes by the dashed line). The lower plot represents the probability that a given time will be one of the three combustion classes, based on the normal distributions. Those events whose group has a higher probability are classified correctly (•) and those whose group has a lower probability are classified incorrectly (x).

For each combination (detonation-plume, detonation-muzzle flash, and plume-muzzle flash) the duration of the event, as quantized by the time required for the NIR emissive area to fall to the noise level,  $t_n^{NIR}$ , provides the highest distinguishability. The distributions of durations were assumed to be Gaussian and are shown in the upper plot of Figure 39 for all three classes. Requiring the total probability (sum of the normalized distributions) be unity, the events were classified simplistically by which probability was the highest for its feature value. Correct (•) and incorrect (x) classifications are shown in the lower plot. DTSS plumes are clearly separated from muzzle flashes, and with few exceptions munitions detonation and muzzle flash distributions have little overlap. In all cases, however, the three combustion events are clearly distinguishable from each other, even using this simplified classification scheme.

This is not so in the case of the peak emissive area in the NIR,  $A_{pk}^{NIR}$ , as can be



seen in Figure 40. The distribution of areas from munitions detonations overlaps with both the muzzle flashes' and the DTSS plumes'. This is because of the high variability in the detonations' areas, contributed to by obscuration of the fireball. The variability in the muzzle flashes and DTSS plumes are much lower, however, providing excellent classification potential.

With the promise for distinguishing between classes of combustion events fairly well evident – even with such a limited examination – the ability to distinguish highly reproducible events of a single combustion class was then examined. Muzzle flashes from several ammunition types were used because the features extracted from them showed very little variability within an ammunition type. The Fisher Ratios for the total emissive area,  $A_{pk}^{NIR}$ , and the bright flash at the barrel,  $A_{sat}^{NIR}$ , in the NIR are shown for each combination of ammunition types in Table 15. Clearly, the total emissive area is the

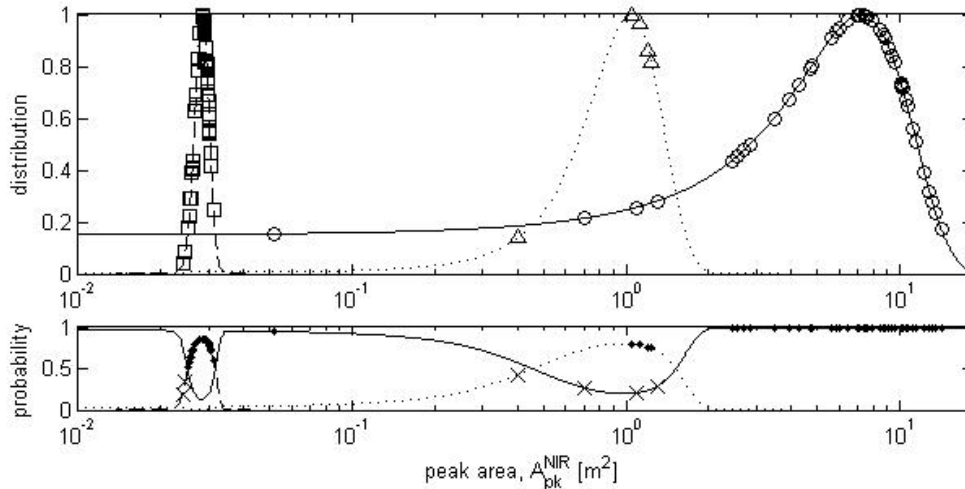


Figure 40: The peak area (in the NIR) is plotted for all detonations (○) DTSS plumes (Δ) and muzzle flashes (□). The upper plot shows the data points assuming normal distributions (detonations are represented by the solid line, plumes by the dotted line, and muzzle flashes by the dashed line). The lower plot represents the probability that a given area will be one of the three combustion classes, based on the normal distributions. Those events whose group has the highest probability are classified correctly (•) and those whose group has a lower probability are classified incorrectly (x).

most differentiating feature. This is shown in Figure 41 where novel FMJ is largely separated from conventional ammunition, and distinguishable from novel ammunition to a lesser extent. The bright flash area is very similar for all ammunition types and proves much less useful for classification.

The previous two sets of comparisons (distinguishing combustion events and distinguishing ammunition types) were undertaken to gain confidence in the methods used and to establish a baseline for how well differentiation could be achieved for events of different classes (detonations, plumes, muzzle flashes) or simple types (ammunitions). Both of these objectives were accomplished. Using the Fisher Ratio with assumed normal distributions did characterize the ability to distinguish between different types and classes – a high *FR* represents good separation and the best probability of correct classification. Features with excellent distinguishability had *FRs* of ten or higher, but *FRs* as low as two offer decent ability to classify. *FRs* lower than about two give uncertain distinctions between classes and much more robust classification techniques are a necessity for there to be any confidence in the results.

Table 15: The Fisher Ratios for all features used in comparing muzzle flashes are shown for each combination of ammunition types.

Feature	Group A #	Group A Type	Group #	Group B Type	FR
$A_{pk}^{NIR}$	13	conventional	14	novel	0.216
$A_{sat}^{NIR}$	13	conventional	14	novel	0.0182
$A_{pk}^{NIR}$	13	conventional	15	FMJ	10.877
$A_{sat}^{NIR}$	13	conventional	15	FMJ	0.0024
$A_{pk}^{NIR}$	14	novel	15	novel FMJ	3.975
$A_{sat}^{NIR}$	14	novel	15	novel FMJ	0.0073

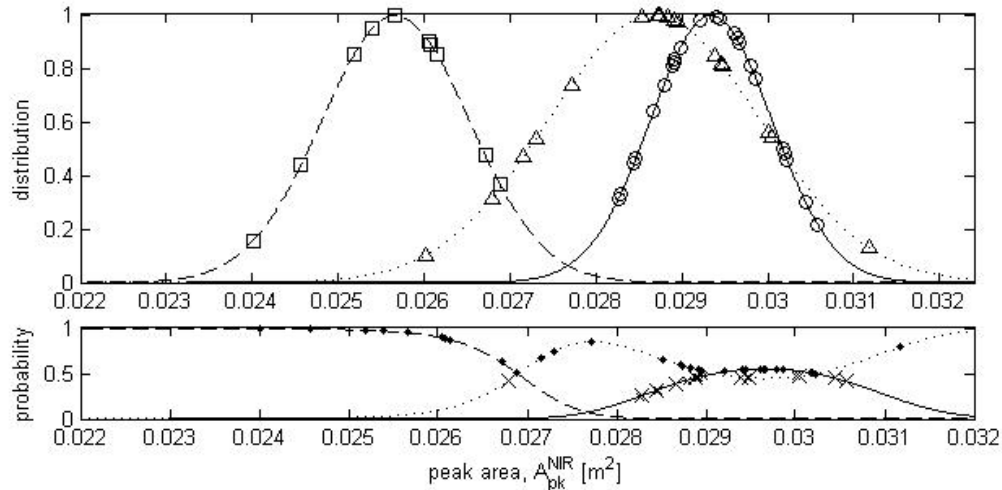


Figure 41: The peak area (in the NIR) is plotted for all conventional ( $\circ$ ) novel ( $\Delta$ ) and novel FMJ ( $\square$ ) muzzle flashes. The upper plot shows the data points assuming normal distributions (conventional are represented by the solid line, novel by the dotted line, and novel FMJ by the dashed line). The lower plot represents the probability that a given area will be one of the three muzzle flash types, based on the normal distributions. Those events whose group has the highest probability are classified correctly ( $\bullet$ ) and those whose group has a lower probability are classified incorrectly ( $\times$ ).

## Distinguishability of Explosive Munitions

This research then moved on to its primary distinguishability objective: differentiating munitions types using features extracted from the fireball and shockwave. Because of the thousands of comparisons (by band, model, group, and time) only a subset of the results are presented here. The first features examined were those that had the highest reproducibility, as determined by the coefficient of variation. These are shown in Table 16 for comparisons of 155mm TNT, 105mm TNT and all TNT munitions to all Composition B munitions. Additionally, 155mm TNT was compared to 105mm TNT to see if weight could be differentiated. All other munitions groups were excluded, either because there were too few events within the group (yielding too much uncertainty in the result) or because the comparisons would have involved events that showed up in both groups (such as 105mm TNT compared to all TNT).

In general, the features that have the highest  $C_V$  values are poor at distinguishing groups of munitions – indicated by the low  $FR$ s – especially for groups containing munitions of the same weight (155mm TNT and all TNT compared to Composition B). Distinguishing groups of differing weight (105mm TNT compared to 155mm TNT or Composition B), however, shows some promise using the peak detonation area,  $A_{det}^{blue}$ . This is useful to know because it indicates that most of the reproducible features are not specific to munitions types, but are characteristic of explosive detonations in general. Thus, they can be used to develop an understanding of the general properties of detonation fireballs and shockwaves. Those properties that show different abilities to distinguish (largely different  $FR$ s) for weight or composition, while perhaps not useful to classification, are useful for understanding correlation of munitions characteristics and fireball or shockwave features. These include  $A_{det}^{blue}$  and to a lesser extent  $t_{det}^{red}$  for

Table 16: Fisher Ratios for highly reproducible fireball and shockwave features are shown for comparisons of explosive type (TNT and Composition B) and weight (155mm and 105mm TNT).

Feature	$A_{det}^{blue}$	$t_{det}^{red}$	$t_n^{NIR}$	$t_n^{MWIR}$	$a^{mdrag}$	$b^{exp}$	$M^{mdrag}  _{t=1}$	$M^{mexp}  _{t=1}$
Groups	all TNT (group 7) and Composition B (group 9)							
FR	0.27	0.001	0.80	0.08	0.21	0.80	0.002	0.39
Groups	105mm TNT (group 6) and Composition B (group 9)							
FR	2.30	0.82	1.25	0.11	0.004	2.05	0.18	1.17
Groups	155mm TNT (group 7) and Composition B (group 9)							
FR	0.0003	0.44	0.61	0.06	0.69	0.41	0.15	0.13
Groups	155mm TNT (group 5) and 105mm TNT (group 6)							
FR	4.76	2.89	0.001	0.004	1.19	0.62	0.132	0.85

determining weight; and  $t_n^{NIR}$  for determining composition. The extent of the correlation between these features is further examined in the sections discussing correlation.

Because the reproducible features are not often useful for distinguishing munitions groups, all features (with the time-dependent shockwave features limited to the first 15 milliseconds after the detonation) were examined for distinguishability; while features with low reproducibility would seem not to be useful for classification, if the separation of their means is high enough then the extent of their irreproducibility may not be significant. Those features with the highest Fisher Ratio for each comparison of groups are shown in

Table 17. General observations are that it is easier to distinguish between groups containing different weights (105mm TNT compared to 155mm TNT and Composition B) than different explosive compositions (Composition B compared to all TNT and 155mm TNT), and that when both weight and composition are different the ability to differentiate is the highest. This is all indicated by the highest Fisher Ratios for groups of different weights, followed by composition.

In every case, the efficiency of detonation in nearly all of the models is the most distinguishing feature. This is shown in Figure 42 for 105mm TNT compared to Composition B at 14.8 milliseconds after detonation, using the modified drag model. The distributions are highly separated and allow the groups to be easily identified. Unfortunately, this feature cannot be used in classification because it requires scaling the observed release of energy by the theoretical detonation energy, the latter of which requires the explosive munition's mass and composition to be known.

A feature related to the efficiency that does not require information about the

munitions type is the observed detonation energy. Because no *a priori* information is included in this feature, its ability to differentiate munitions types is decreased nearly two orders of magnitude, as shown in Figure 43 for the same data. Thus requiring

Table 17: The highest Fisher Ratios for each comparison are shown. Only a single physical quantity of each model is shown because they are all transformations of the same data. When multiple bands or models had similar values, the one with the largest FR is given and indicated by \*. For time-dependent features, the time is given in milliseconds.

TNT & Composition B		105mm TNT & Composition B		155mm TNT & Composition B		155mm TNT & 105mm TNT	
feature	FR	feature	FR	feature	FR	feature	FR
$f^{mdrag}  _{t=6.2} *$	2.94	$f^{mdrag}  _{t=14.8} *$	103	$f^{mdrag}  _{t=11.7} *$	6.7	$f^{drag350}  _{t=10.1} *$	19.3
$t_{pk}^{green} *$	2.28	$t_{pk}^{green} *$	14.3	$P_1^{drag}  _{t=10.9}$	1.92	$M^{exp350}  _{t=0.3}$	9.55
$c^{mdrag}$	1.93	$A^{blue}  _{t=0.7} *$	6.98	$t_{pk}^{green} *$	1.79	$A^{red}  _{t=1.0} *$	6.58
$b^{drag}$	1.5	$M^{mexp}  _{t=12.7} *$	5.48	$t_t^{green}$	1.62	$E_D^{mdrag}  _{t=12.4}$	5.28
$a^{drag}$	1.36	$P_1^{mdrag}  _{t=12.8}$	4.91	$P_1^{exp}  _{t=9.9}$	1.47	$A_{det}^{red} *$	5.25
$R^{drag}  _{t=0.2}$	1.14	$P_1^{exp350}  _{t=0.4}$	4.13	$A^{red}  _{t=6.7} *$	1.3	$a^{drag350}$	3.62
$a^{mexp}$	1.11	$c^{mdrag}$	4.06	$c^{mdrag}$	1.21	$t_{det}^{red} *$	2.89

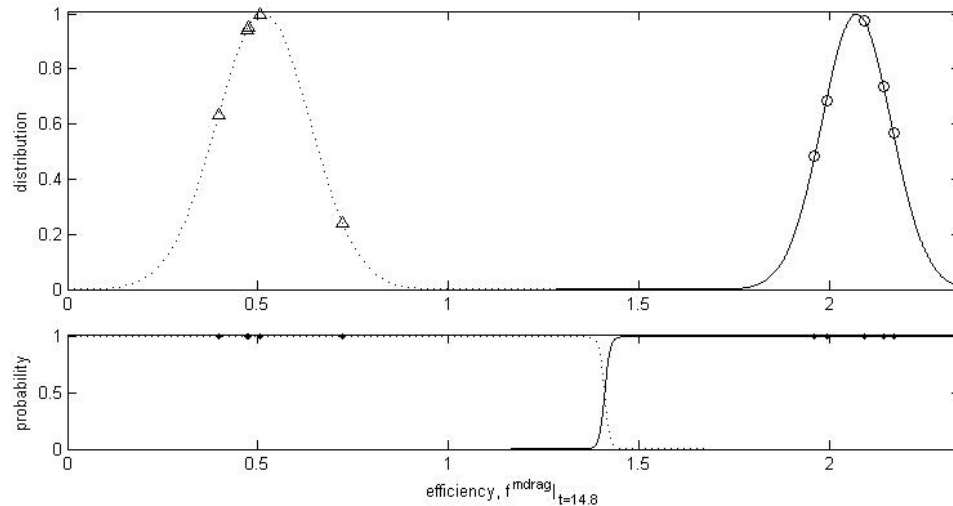


Figure 42: The efficiency of detonation at 14.8 msec (from the modified drag model) is plotted for all 105mm TNT ( $\circ$ ) and Composition B ( $\Delta$ ) detonations. The upper plot shows the data points assuming normal distributions, where 105mm TNT is represented by the solid line and Composition B by the dotted line. The lower plot represents the probability that a given efficiency will be one munitions group or the other, based on the normal distributions. Those events whose group has a higher probability are classified correctly ( $\bullet$ ) and those whose group has a lower probability are classified incorrectly ( $\times$ ). The *FR* is 103.

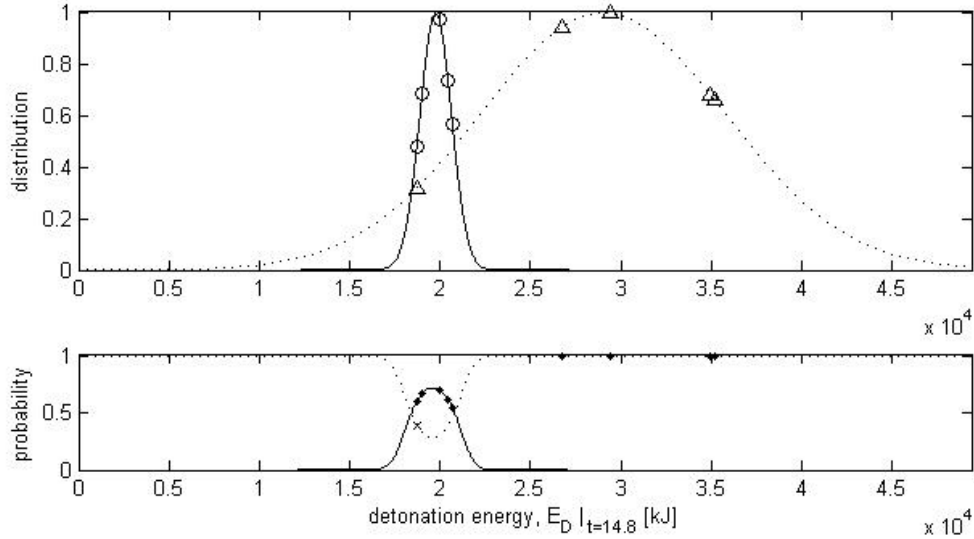


Figure 43: The energy of detonation at 14.8 msec (from the modified drag model) is plotted for all 105mm TNT ( $\circ$ ) and Composition B ( $\Delta$ ) detonations. The upper plot shows the data points assuming normal distributions, where 105mm TNT is represented by the solid line and Composition B by the dotted line. The lower plot represents the probability that a given efficiency will be one munitions group or the other, based on the normal distributions. Those events whose group has a higher probability are classified correctly ( $\bullet$ ) and those whose group has a lower probability are classified incorrectly ( $\times$ ). The  $FR$  is 1.8314.

knowledge of the munitions type in order to classify precludes the efficiency (as derived from the observed detonation energy), to be used as a classification feature, it does indicate dependence of the efficiency on munitions characteristics. This is explored further in the correlation sections.

The time to the peak area, particularly in the green band,  $t_{pk}^{green}$ , offers decent ability to distinguish between munitions of different explosive compositions, particularly if they are different weights. The feature distribution is shown for all TNT and Composition B detonations in Figure 44. The features show decent separation, which improves by nearly a factor of seven if only 105mm TNT and Composition B are plotted. From this, it appears that TNT's fireball area peaks several orders of magnitude later than Composition B's, but the number of events were limited and so whether this was a real characteristic of the explosive composition or was caused by obscuration of the fireball

during those events is unknown. If explosive composition does not vary and only weight is examined, this feature has poor distinguishability. This is indicated by the fact that the *FR* for comparison of 155mm and 105mm TNT is only 0.161 – the separation of the means of their distributions is much smaller than their widths. Thus the time to the peak fireball size does not appear to be a highly weight dependent property, but rather is primarily dependent on explosive composition.

A feature that does appear to have a dependence on the mass of the explosive is the peak detonation area,  $A_{det}^{red}$ . This feature shows good distinguishability in the RGB (but the red band is slightly better than the others). The feature distributions for 155mm and 105mm TNT detonations are shown in Figure 45, where it is clear that the reproducibility of the feature is not high, yet the mean areas are separated enough that the two weights of TNT can be distinguished. This feature’s ability to distinguish between weights is not limited to a single explosive composition – the *FRs* from comparing

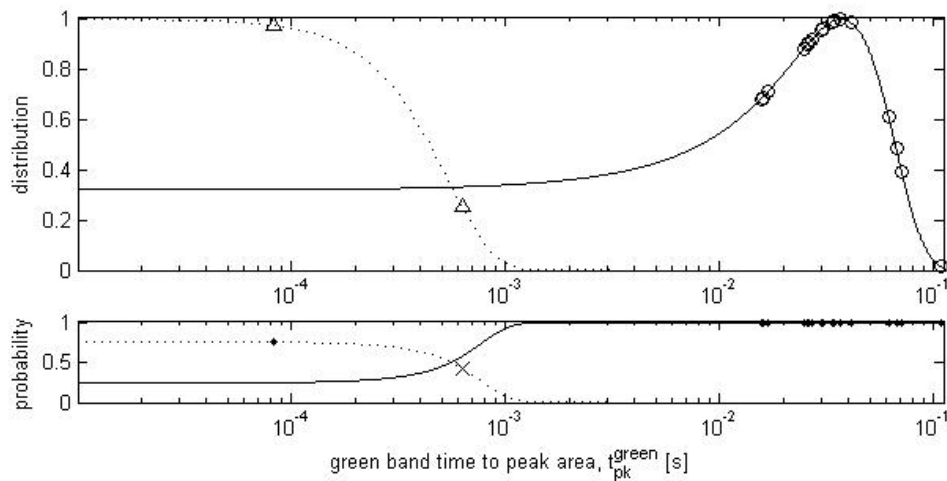


Figure 44: The time to the peak fireball area (in the green band) is plotted for all TNT (○) and Composition B (Δ) detonations. The upper plot shows the data points assuming normal distributions, where TNT is represented by the solid line and Composition B by the dotted line. The lower plot represents the probability that a given time will be one munitions group or the other, based on the normal distributions. Those events whose group has a higher probability are classified correctly (•) and those whose group has a lower probability are classified incorrectly (x). The *FR* is 2.28.



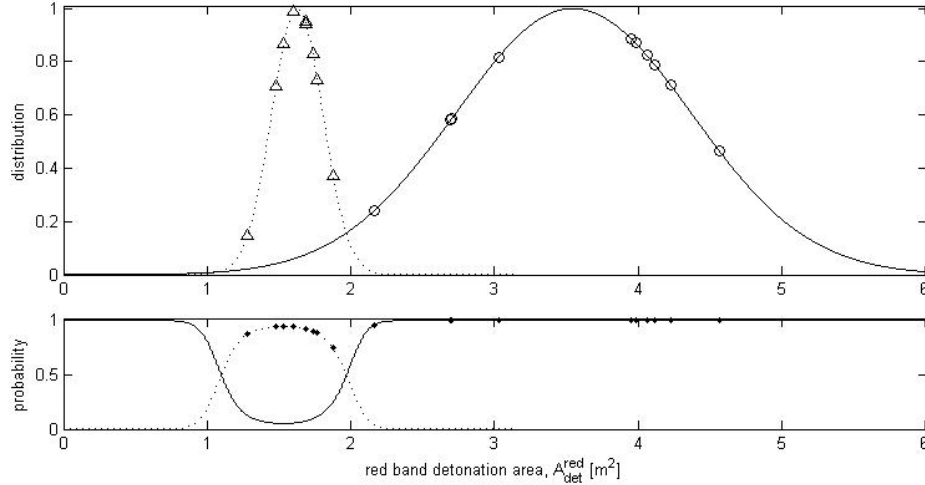


Figure 45: The detonation area (in the red band) is plotted for all 155mm TNT ( $\circ$ ) and 105mm TNT ( $\Delta$ ) detonations. The upper plot shows the data points assuming normal distributions, where 155mm TNT is represented by the solid line and 105mm TNT by the dotted line. The lower plot represents the probability that a given area will be one weight or the other, based on the normal distributions. Those events whose group has a higher probability are classified correctly ( $\bullet$ ) and those whose group has a lower probability are classified incorrectly ( $\times$ ). The  $FR$  is 5.25.

105mm TNT to Composition B was 2.6. When similar weights are compared, however, separation of the data is poor even with different explosive compositions. This is evidenced by 155mm TNT and all TNT having  $FR$ s of 0.000322 and 0.293 when compared to Composition B. It cannot be conclusively stated, however, that  $A_{det}^{red}$  is a weight dependent property. Rather, the most likely explanation is that it is an energy dependent property where different masses represent different initial releases of energy. Because of the variability of the detonation efficiency and the similarity of detonation energies in Composition B and TNT, further work needs to be done to fully understand the dependence of  $A_{det}^{red}$  on munitions characteristics.

Because of the extremely large number of feature comparisons, not all of the features were discussed. It can be seen from the values of the Fisher Ratios presented,

however, that those features with high reproducibility are rarely the best for classification – they tend to represent features of explosive detonations in general rather than specific types of munitions. Many features that have a moderate distribution of their values, however, perform well in differentiating the munitions groups because their means are highly separated. For true classification work, the features provided in the table give a starting point for more robust classification techniques. What was gathered here is an understanding that there are certain features which are highly separable for different groups of munitions, and that identifying which features are correlated to which munitions characteristics (and each other) is feasible.

### **Correlation of Munitions Characteristics with Extracted Features**

The correlation of munitions characteristics with shockwave and fireball features provides a great deal of insight into understanding explosive detonations. Because of the limited number of events of each type, all events were first used in determining correlations. This provided a more statistically meaningful sampling and allowed trends for detonations in general to be found. The results are shown in Table 18 for four munitions characteristics, although five are actually represented because  $H_A$  and  $H_D$  show the same correlations. Shockwave features appear much more highly correlated with the munitions characteristics than the fireball features, although this may be representative of the fact that the shockwave features were all derived from fits and thus have less variability (uncertainties in individual data points do not show up). Because of this, the ten shockwave features and the four fireball features with the highest coefficient of determination are shown.

Table 18: The coefficient of determination,  $r^2$ , is shown for the features of the shockwave (highest 10) and fireball (highest 4) that are most highly correlated with all of the munitions' afterburn energy, detonation energy, specific energy released in the afterburn, heat of detonation, and mass.  $H_A$  and  $H_D$  were found to be redundant and are shown together.

$r^2$	$E_A$	$r^2$	$E_D$	$r^2$	$H_A \& H_D$	$r^2$	$m$
0.828	$f^{drag350}_{ t=200}$	0.743	$f^{drag350}_{ t=10.7}$	0.567	$\sqrt[3]{t^{green}_{pk}}$	0.789	$f^{mexp}_{ t=22}$
0.825	$f^{exp350}_{ t=190.5}$	0.736	$f^{mexp}_{ t=22}$	0.542	$\sqrt[3]{t^{red}_{50}}$	0.783	$f^{drag350}_{ t=20.5}$
0.737	$f^{exp}_{ t=22.5}$	0.724	$f^{exp}_{ t=17.2}$	0.497	$f^{mdrag}_{ t=6.2}$	0.781	$f^{exp}_{ t=17.7}$
0.713	$f^{mexp}_{ t=27.6}$	0.701	$f^{exp350}_{ t=18.9}$	0.493	$f^{drag350}_{ t=7.8}$	0.763	$f^{exp350}_{ t=26.6}$
0.698	$f^{mdrag}_{ t=132.7}$	0.69	$f^{drag}_{ t=15.7}$	0.49	$a^{mexp}$	0.733	$f^{drag}_{ t=15.8}$
0.677	$f^{drag}_{ t=27.8}$	0.687	$f^{mdrag}_{ t=11.9}$	0.466	$f^{exp350}_{ t=6.2}$	0.722	$f^{mdrag}_{ t=15.3}$
0.583	$M^{exp350}_{ t=0.5}$	0.482	$M^{drag}_{ t=51.2}$	0.454	$c^{mexp}$	0.469	$M^{mdrag}_{ t=62.6}$
0.557	$R^{exp350}_{ t=40.6}$	0.479	$b^{drag}$	0.424	$f^{exp}_{ t=9.2}$	0.466	$b^{drag}$
0.547	$R^{mdrag}_{ t=26.9}$	0.478	$R^{drag}_{ t=130}$	0.417	$R^{drag}_{ t=37.2}$	0.461	$R^{drag}_{ t=200}$
0.524	$p_1^{exp350}_{ t=0.7}$	0.466	$a^{drag}$	0.415	$M^{mexp}_{ t=200}$	0.459	$a^{drag}$
0.518	$\sqrt[3]{A^{red}_{det}}$	0.402	$\sqrt[3]{t^{green}_{pk}}$	0.414	$f^{drag}_{ t=12.9}$	0.33	$\sqrt[3]{t^{green}_{pk}}$
0.337	$\sqrt[3]{t^{blue}_{det}}$	0.267	$\sqrt[3]{t^{red}_{50}}$	0.412	$f^{mexp}_{ t=14.2}$	0.292	$\sqrt[3]{A^{red}_{det}}$
0.226	$\sqrt[3]{t^{NIR}_{50}}$	0.237	$\sqrt[3]{t^{MWIR}_n}$	0.401	$\sqrt[3]{A^{red}_t}$	0.232	$\sqrt[3]{t^{MWIR}_n}$
0.2	$\sqrt[3]{A^{NIR}_t}$	0.214	$\sqrt[3]{A^{red}_{det}}$	0.269	$\sqrt[3]{t^{NIR}_n}$	0.227	$\sqrt[3]{t^{MWIR}_{10}}$

Several of these features are plotted in order to examine the correlations more closely. Because there are up to nine types of munitions included in the plots, each munitions type was assigned a marker. These are indicated in Table 19 and are used to show the distribution of feature values for each munitions type.

With the exception of a handful of outliers, the efficiency of the detonation (ratio of experimentally calculated detonation energy to theoretical detonation energy),  $f$ , scales well with the afterburn energy,  $E_A$ , and detonation energy,  $E_D$ , for all models (upper plots of Figure 46). This implies that the value of the detonation energy determined by the shockwave (from pressures and scaled distances) is not independent of the energy

Table 19: The markers used to designate munitions type in Figure 46 through Figure 52 are shown below. All types containing C-4 are designated with the same marker because these types were not independently examined.

Type #	Arrangement	Marker
1	155mm TNT erect	+
2	155mm TNT prone	x
3	105mm TNT erect	□
4	105mm TNT prone	◇
5	3x1.25# C-4	•
6	10# C-4	•
7	155mm Composition B erect	☆
8	2x155mm Composition B erect	△
9	155mm TNT / 30# C-4 / barrel	•

released after detonation; i.e. the properties of the shockwave are not dependent only on the initial detonation, but are also dependent on the continuing evolution of the afterburn fireball. As more energy is released in the ongoing combustion, the pressure decays more slowly than expected (efficiencies greater than one), and the calculated release of energy at  $t = 0$  continues to increase. This is the equivalent energy that would have been released in an instantaneous detonation to generate the shockwave that is now sustained by release of energy in the fireball.

The correlation between the theoretical afterburn energy and the efficiency indicates that as the amount of energy released in the afterburn increases, the efficiency decreases. Whether this is because the detonation energy is also increasing (due to greater mass in the explosive) or the shockwave is sustained to a lesser extent (with increasing energy release in the afterburn) can be examined by looking at the dependence of the efficiency on mass and specific energies. According to Equation 41, the efficiency is proportional to the observed release of energy and inversely proportional to the heat of detonation and the initial mass. The observed release of energy is also dependent on the heat of detonation and initial mass, as well as the specific energy of the afterburn.

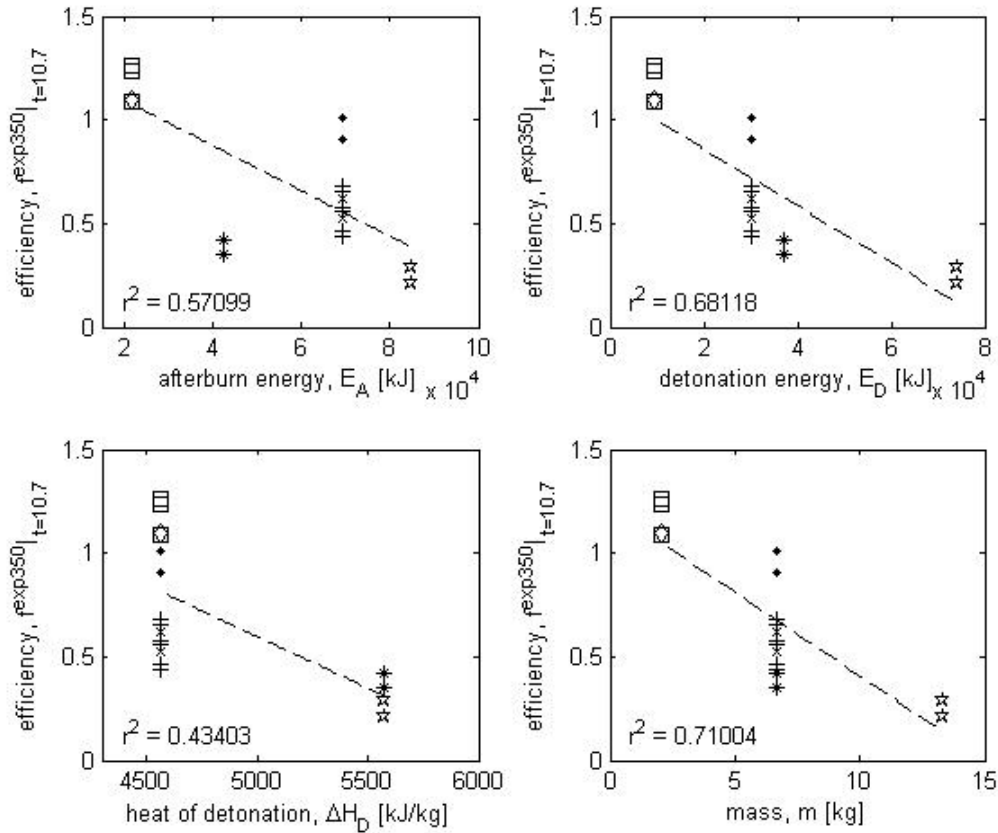


Figure 46: Detonation efficiency is plotted against the afterburn and detonation energies in the upper plots, heat of detonation (which follows the same correlation as the specific afterburn energy) initial mass in the lower plots. As all quantities increase, the efficiency decreases.

Theoretically, the energy released should be linearly dependent on these quantities, but because detonations are non-ideal, the relationship between increasing any of the dependencies and the observed energy released may not be linear. However, an increase in mass or specific energy necessitates an increase in observed energy. By holding mass constant (ignoring all but 155mm munitions in the lower left plot of the figure) the efficiency is seen to decrease to a small degree with increasing heat of detonation. When holding the heat of detonation constant, the efficiency decreases significantly with increasing mass. The conclusion that can be drawn from this is that the efficiency of the detonation is fairly independent of the specific energies of the explosive

compound and depends primarily on the mass of the munition – either higher mass munitions' afterburns contribute less to the shockwave than those of lower mass, or the overpressure generated by the higher mass detonation is not as great as the simple theory of detonations predicts. The latter of these is reasonably explained in that larger masses deviate from the assumptions used to a greater extent, i.e. masses are not point masses and energy is released over a longer duration.

After the efficiency is examined, the correlation of shockwave and fireball features with munitions characteristics decreases significantly (although efficiency was never a highly correlated feature of the specific energies). The next highest feature correlated with mass and energies is the Mach number,  $M$ , shortly after detonation; the highest correlation with the specific energies is the cube root of the time to the peak fireball area in the green band,  $\sqrt[3]{t_{pk}^{green}}$ . These are shown in Figure 47.

The correlation for each pair of features is low, but there are definite trends: Mach number increases with increasing mass and afterburn energy. The Mach number shows a decrease with detonation energy; the opposite should be true. This is due to the use of the drag model at a time that is well beyond the mid-field. This makes the important point that although the features show a high degree of correlation, they may not be meaningful physically if examined outside of the field allowed by the assumptions used.

The other trend is for the time to the peak fireball area (shown in the green band but accurate for all RGB bands) to decrease as the third power of the heat of detonation. As higher energies are released in the detonation, it takes less time for the fireball to peak. This is probably indicative of higher initial energies causing the explosive compound to be consumed more quickly in the afterburn and peak early, then as the fuel

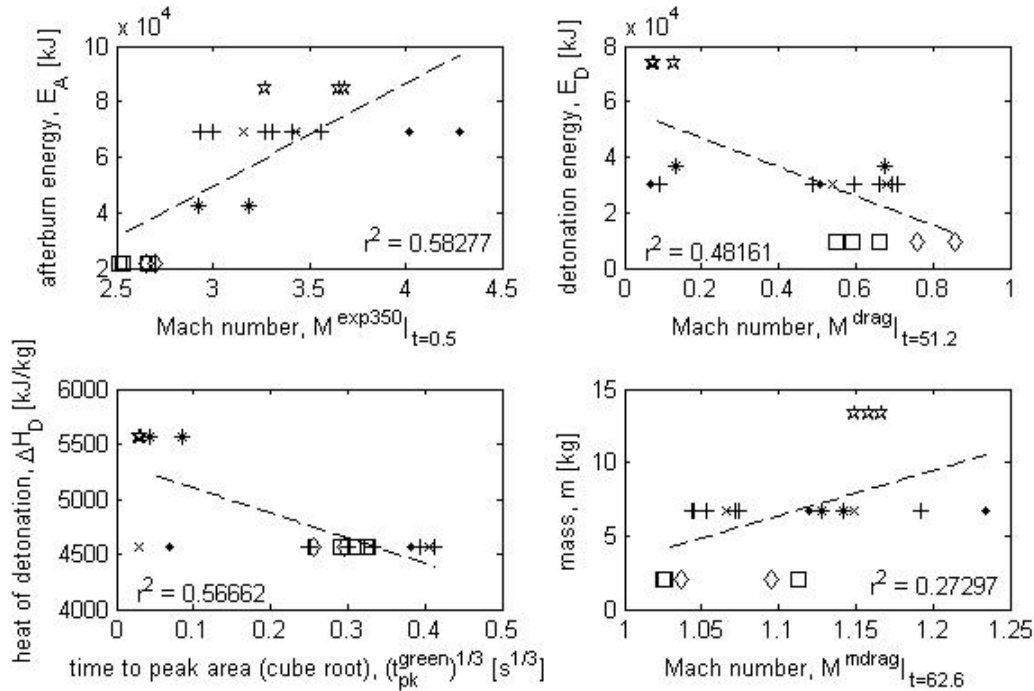


Figure 47: The highest non-efficiency correlations are shown for each munition characteristic. The Mach number tends to increase with mass and afterburn energy, although correlation is poor. The decrease in Mach number with detonation energy is due to the use of the drag model outside of its intended field and is not physically accurate. The time to the peak fireball area increases with the third power of the heat of detonation, neglecting the outliers.

is used up the fireball will begin to decay. Evidence to support this is that as the heat of detonation increases, the duration of the fireball (in all bands) decreases. More observations of a larger number of munition weights and compositions are required to verify this.

The remaining features all show a decreasing degree of correlation with munitions characteristics. This is not to say that they aren't correlated. Rather, the detonations have a high degree of variability, contributed to by obscuration of the fireball by soot, dirt, and smoke. Despite the irreproducibility in the data, certain trends are apparent: Mach number, pressure, and peak detonation area all increase with increasing mass and detonation energy; increased afterburn energy and specific energy results in greater

fireball areas and less time to the peak fireball area; and detonation efficiency decreases with increasing initial mass.

Since C-4 was not studied in this research, it was useful to remove the groups to which it belonged when finding correlations. This allowed it to be determined whether or not the general trends observed using all munitions were representative of detonations in general or specific to TNT and Composition B (because Composition B contains TNT). The coefficients of determination for the TNT and Composition B group are shown in Table 20.

Table 20: The coefficient of determination,  $r^2$ , is shown for the features of the shockwave (highest 10) and fireball (highest 4) that are most highly correlated with all of the TNT and Composition B munitions' afterburn energy, detonation energy, specific energy released in the afterburn, heat of detonation, and mass.  $H_A$  and  $H_D$  were found to be redundant and are shown together.

$r^2$	$E_A$	$r^2$	$E_D$	$r^2$	$H_A \& H_D$	$r^2$	$m$
0.826	$f^{\text{exp350}} _{t=190.5}$	0.762	$f^{\text{drag350}} _{t=9.4}$	0.668	$\sqrt[3]{t^{\text{green}}_{pk}}$	0.802	$f^{\text{drag350}} _{t=10.1}$
0.826	$f^{\text{drag350}} _{t=200}$	0.737	$f^{\text{mexp}} _{t=22}$	0.634	$\sqrt[3]{t^{\text{red}}_{50}}$	0.798	$f^{\text{mexp}} _{t=22}$
0.821	$M^{\text{exp350}} _{t=0.3}$	0.737	$f^{\text{exp}} _{t=18.3}$	0.503	$\sqrt[3]{A_t^{\text{red}}}$	0.795	$f^{\text{exp}} _{t=18.3}$
0.798	$P_1^{\text{exp350}} _{t=0.3}$	0.724	$f^{\text{exp350}} _{t=10.4}$	0.499	$R^{\text{drag}} _{t=46.8}$	0.779	$f^{\text{exp350}} _{t=13}$
0.769	$f^{\text{mdrag}} _{t=36.6}$	0.722	$f^{\text{drag}} _{t=21.3}$	0.498	$P_1^{\text{drag}} _{t=19.5}$	0.767	$f^{\text{drag}} _{t=23.1}$
0.765	$f^{\text{mexp}} _{t=22.4}$	0.712	$f^{\text{mdrag}} _{t=12.6}$	0.496	$M^{\text{drag}} _{t=19.2}$	0.766	$f^{\text{mdrag}} _{t=14.2}$
0.759	$f^{\text{exp}} _{t=21.5}$	0.657	$P_1^{\text{drag}} _{t=0.9}$	0.495	$E_D^{\text{drag}} _{t=27.2}$	0.678	$M^{\text{exp350}} _{t=0.6}$
0.736	$R^{\text{mdrag}} _{t=29.7}$	0.657	$E_D^{\text{drag}} _{t=3.4}$	0.483	$f^{\text{mdrag}} _{t=6.2}$	0.677	$P_1^{\text{exp350}} _{t=0.6}$
0.722	$R^{\text{exp350}} _{t=24.6}$	0.652	$R^{\text{drag}} _{t=0.2}$	0.479	$f^{\text{drag350}} _{t=7.8}$	0.651	$P_1^{\text{drag}} _{t=3}$
0.711	$E_D^{\text{mdrag}} _{t=15.4}$	0.652	$M^{\text{drag}} _{t=0.8}$	0.478	$a^{\text{mexp}}$	0.649	$E_D^{\text{drag}} _{t=6}$
0.689	$\sqrt[3]{A_{\text{det}}^{\text{red}}}$	0.459	$\sqrt[3]{t^{\text{green}}_{pk}}$	0.462	$f^{\text{exp350}} _{t=4}$	0.507	$\sqrt[3]{A_{\text{det}}^{\text{red}}}$
0.492	$\sqrt[3]{t_{\text{det}}^{\text{blue}}}$	0.418	$\sqrt[3]{A_{\text{det}}^{\text{red}}}$	0.462	$b^{\text{drag}}$	0.376	$\sqrt[3]{t^{\text{green}}_{pk}}$
0.222	$\sqrt{t_{50}^{\text{NIR}}}$	0.297	$\sqrt[3]{t_{50}^{\text{red}}}$	0.434	$c^{\text{mexp}}$	0.223	$\sqrt[3]{t_{50}^{\text{red}}}$
0.202	$\sqrt{t_{10}^{\text{MWIR}}}$	0.23	$\sqrt[3]{A_t^{\text{red}}}$	0.256	$\sqrt[3]{t_n^{\text{NIR}}}$	0.205	$\sqrt{t_{10}^{\text{MWIR}}}$



The most correlated features in the TNT and Composition B group contain many of the same features as those for all munitions, except that the correlation is much higher for just TNT and Composition B. This is evident through examination of the features in this group that were looked at previously for all munitions (Figure 48). Once again, the efficiency is one of the most highly correlated features, but now some of the other physical quantities (Mach number, pressure, and radius) show high correlation for times immediately after detonation. This is indicative of commonality in the detonation of TNT and Composition B that is not present in C-4. This is most likely due to the fact that Composition B contains TNT, and it may be possible to differentiate such explosive compositions from C-4 based on these features. Because C-4 was not examined in this research, this objective remains to be completed in future work.

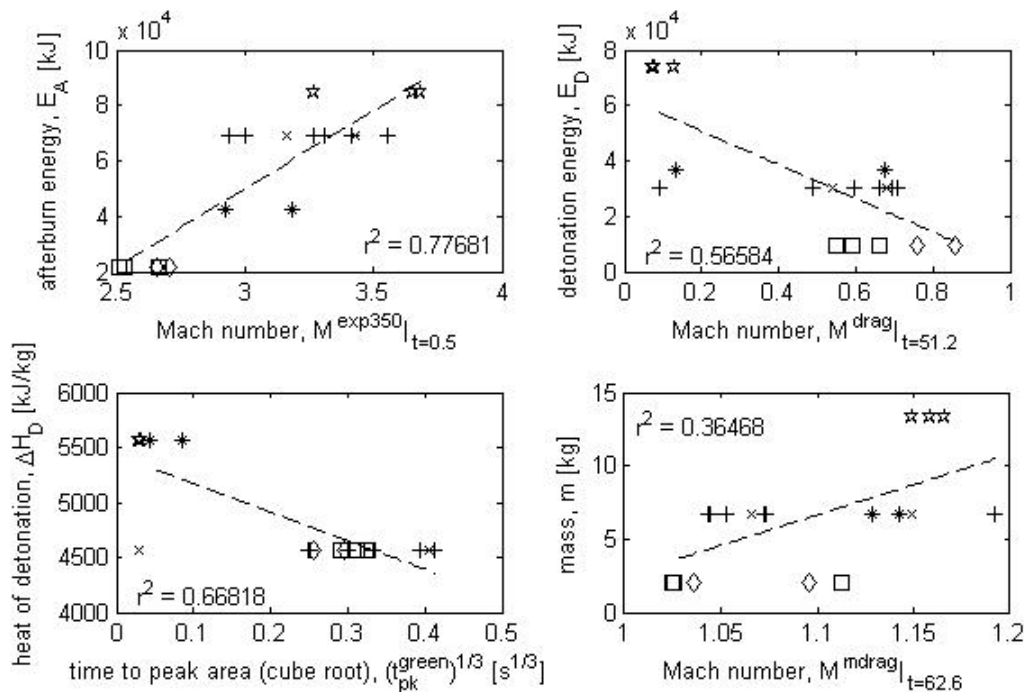


Figure 48: The highest non-efficiency correlations are shown for each TNT and Composition B characteristic. The Mach number tends to increase with mass and afterburn energy, although correlation is poor. The decrease in Mach number with detonation energy is due to the use of the drag model outside of its intended field and is not physically accurate. The time to the peak fireball area increases with the third power of the heat of detonation, neglecting the outliers.

Moving away from general correlations in explosive detonations, the correlations in TNT were then examined. Because there were only two munitions types, the correlation was based on those properties that were different between the two:  $E_A$ ,  $E_D$ , and  $m$ . Correlation of fireball and shockwave features with all of these munitions features is redundant, and so all are grouped together. The specific energy released in the afterburn and the heat of detonation were ignored because they did not change with weight. Thus, it may be concluded that the features of the shockwave and fireball are effectively correlated with mass. The values of the correlation are shown in Table 21. Once again, the efficiency of the detonation is the most highly correlated feature, and for the two masses of TNT, it shows nearly perfect agreement. Likewise, the physical quantities (Mach number, pressure, and radius) shortly after detonation also show a high degree of correlation with the mass. The fireball features show less correlation than the shockwave features, but still have a definite trend: the features increase and the mass increases. The efficiency as a function of mass is shown in Figure 49. Because there are

Table 21: The coefficient of determination,  $r^2$ , is shown for the features of the shockwave (highest 10) and fireball (highest 4) that are most highly correlated with all of the TNT munitions' afterburn energy, detonation energy, specific energy released in the afterburn, heat of detonation, and mass.

$r^2$	$E_A, E_D, \& m$	$r^2$	$E_A, E_D, \& m$
0.994	$f^{\text{exp350}}_{ t=186.6}$	0.766	$\sqrt[3]{A_{\text{det}}^{\text{red}}}$
0.979	$f^{\text{mexp}}_{ t=23.4}$	0.747	$R^{\text{mdrag}}_{ t=23.8}$
0.962	$f^{\text{mdrag}}_{ t=15.3}$	0.736	$R^{\text{mexp}}_{ t=37.4}$
0.955	$f^{\text{exp}}_{ t=19.2}$	0.729	$R^{\text{exp350}}_{ t=29.4}$
0.889	$f^{\text{drag}}_{ t=24.8}$	0.67	$\sqrt[3]{t_{\text{det}}^{\text{red}}}$
0.815	$M^{\text{exp350}}_{ t=0.3}$	0.412	$\sqrt[3]{t_{50}^{\text{NIR}}}$
0.784	$P_1^{\text{exp350}}_{ t=0.3}$	0.395	$\sqrt[3]{t_{10}^{\text{NIR}}}$

only two values for mass, measure of the linear correlation between the features isn't very meaningful other than to show that there is a scaling relationship. Greater samplings of feature values are required to determine the form of the trend.

In all groups, the correlation between the features and the munitions characteristics indicates that mass and energy have a direct relationship with the characteristics of the fireball and shockwave. The relationship is not surprising: fireball size and shockwave pressure, velocity, and energy all increase with increasing munitions mass and energy. Additionally, the efficiency of the explosive decreases with increased mass. The principal correlations are summarized in Table 22.

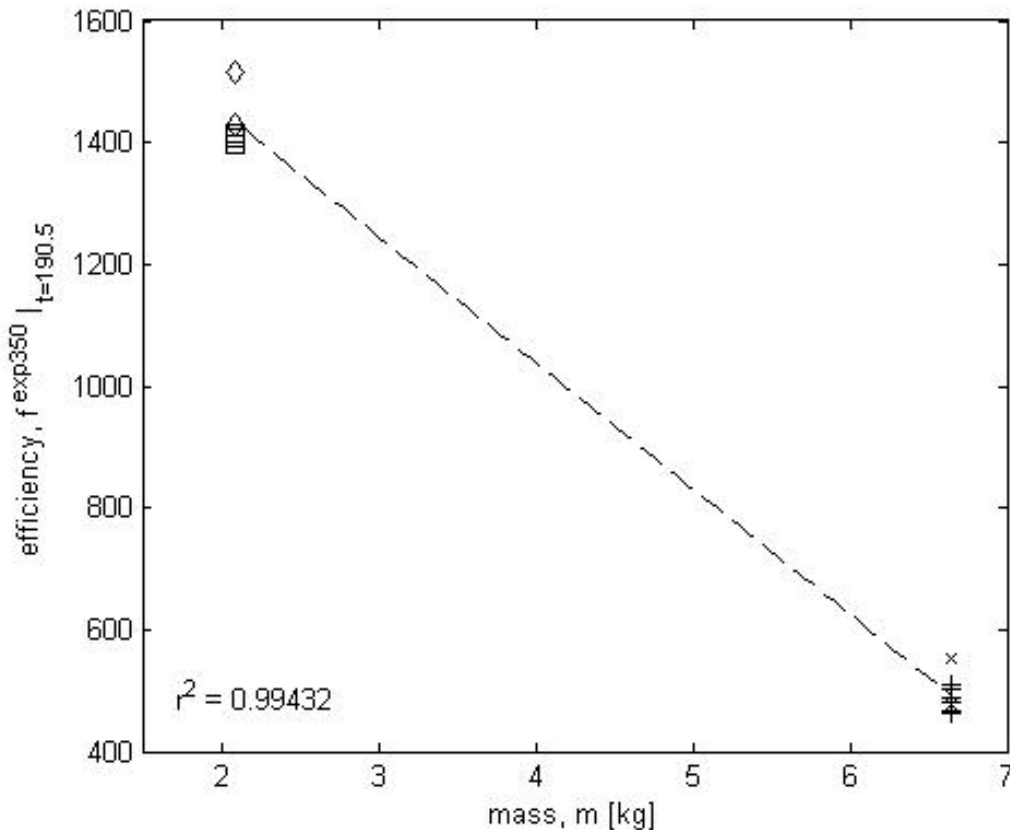


Figure 49: Efficiency is plotted against the two masses of TNT and the correlation is shown. Because there were only two weights of TNT, this plot indicate separation of the data more than correlation. However, the trend is apparent and can be used as a scaling rule of thumb.

Table 22: The shockwave and fireball features that showed a moderate or greater degree of correlation with munitions characteristics are shown. The typical range of  $r^2$  values are given, with all munitions representing the lower end and TNT representing the upper. The trend indicates how the feature behaves with increases in the munitions characteristic.

Feature	Strongest Dependencies	Typical $r^2$	Trend
detonation area, $A_{det}$ RGB	afterburn energy, $E_A$ detonation energy, $E_D$ mass, $m$	0.3~0.766	increases cubically
peak area, $A_{pk}$ RGB	specific energies, $H_A$ & $H_D$	0.3~0.445	increases cubically
efficiency, $f$	mass, $m$	0.7~0.99	decreases linearly
Mach number, $M$	afterburn energy, $E_A$ detonation energy, $E_D$ mass, $m$	0.482~0.815	increases linearly
overpressure, $p_l$	afterburn energy, $E_A$ detonation energy, $E_D$ mass, $m$	0.4~0.784	increases linearly
shock radius, $R$	afterburn energy, $E_A$ detonation energy, $E_D$ mass, $m$	0.56~0.784	increases linearly
time to decay 50%, $t_{50}$ RGB, NIR	specific energies, $H_A$ & $H_D$	0.222~0.634	increases cubically
time to detonation, $t_{det}$ RGB	mass, $m$	0.67~0.77	increases cubically
time to peak, $t_{pk}$ RGB	specific energies, $H_A$ & $H_D$	0.4~0.668	decreases cubically
maximum radius, $a^{drag}$	detonation energy, $E_D$ mass, $m$	0.156~0.459	decreases linearly
characteristics radius, $a^{drag350}$	detonation energy, $E_D$ mass, $m$	0.1~0.62	increases linearly
drag coefficient, $b^{drag}$	detonation energy, $E_D$ mass, $m$	0.129~0.467	decreases linearly

### Correlation of Fireball Features with Shockwave Features

Having found features of the shockwave and fireball that were highly correlated with munitions characteristics (and the trends associated with them), the correlation between the fireball and shockwave features themselves were examined. There were thousands of comparisons, hundreds of which showed high correlation ( $r^2 > 0.7$ ). Many of these were redundant (all RGB bands of a single fireball feature showed similar correlation with many features of the shockwave at evaluations of the same time and with

several models). To reduce the redundancy of the data, only the most highly correlated shockwave feature in each group is shown in

Table 23 for each fireball feature (in one RGB band). Likewise, because linear, quadratic, and cubic correlation was determined for many of the fireball features, only the power that had the largest coefficient of determination is given.

Table 23: For each fireball feature, the most correlated shockwave feature from each group (all munitions, TNT and Composition B, and TNT) is shown. The time at which temporal features were evaluated is indicated in milliseconds.

Fireball	Shockwave (all munitions)	$r^2$	Shockwave (TNT & CompB)	$r^2$	Shockwave (TNT)	$r^2$
$A(t)^{red}$ *	$E_D^{mexp}  _{t=0.3}$	0.773	$b^{exp350}  _{t=34.9}$	0.645	$b^{exp350}  _{t=35}$	0.653
$A_t^{MWIR}$	$E_D^{drag}  _{t=81.8}$	0.724	$E_D^{drag}  _{t=81.8}$	0.74	$a^{drag350}$	0.918
$A_{pk}^{MWIR}$	$E_D^{drag}  _{t=81.8}$	0.758	$E_D^{drag}  _{t=81.8}$	0.766	$a^{drag350}$	0.864
$t_{10}^{MWIR}$	$f^{exp350}  _{t=113.6}$	0.195	$p_1^{mexp}  _{t=113.6}$	0.299	$a^{drag350}$	0.899
$t_{50}^{MWIR}$	$R^{mdrag}  _{t=0.4}$	0.773	$R^{mdrag}  _{t=0.5}$	0.802	$f^{mexp}  _{t=0.2}$	0.5
$\sqrt[3]{t_n^{MWIR}}$	$f^{drag}  _{t=5.6}$	0.373	$f^{drag}  _{t=8}$	0.385	$a^{drag350}$	0.975
$\sqrt[3]{A_t^{NIR}}$	$R^{mexp}  _{t=0.9}$	0.522	$R^{mexp}  _{t=1.1}$	0.282	$f^{drag}  _{t=31.9}$	0.599
$A_{pk}^{NIR}$	$f^{mdrag}  _{t=1}$	0.881	$R^{mexp}  _{t=1}$	0.606	$R^{drag350}  _{t=1.8}$	0.714
$\sqrt[3]{t_{10}^{NIR}}$	$E_D^{mexp}  _{t=33.9}$	0.259	$E_D^{mexp}  _{t=32}$	0.277	$f^{mdrag}  _{t=8.6}$	0.536
$\sqrt[3]{t_{50}^{NIR}}$	$E_D^{mexp}  _{t=38.1}$	0.261	$E_D^{mexp}  _{t=32}$	0.331	$f^{mdrag}  _{t=7.4}$	0.629
$\sqrt{t_n^{NIR}}$	$E_D^{mexp}  _{t=45.8}$	0.309	$E_D^{mexp}  _{t=45.8}$	0.278	$f^{mdrag}  _{t=7}$	0.393
$A_{pk}^{blue}$	$f^{exp350}  _{t=0.5}$	0.709	$R^{mexp}  _{t=0.5}$	0.449	$b^{exp350}$	0.68
$\sqrt[3]{A_{det}^{red}}$	$E_D^{drag350}  _{t=6.7}$	0.741	$f^{mdrag}  _{t=71.8}$	0.689	$f^{mexp}  _{t=32.1}$	0.825
$\sqrt[3]{A_t^{blue}}$	$E_D^{drag}  _{t=17.7}$	0.529	$p_1^{mdrag}  _{t=16}$	0.567	$b^{exp350}$	0.566
$\sqrt[3]{t_{pk}^{blue}}$	$c^{mdrag}$	0.634	$p_1^{mdrag}  _{t=21.3}$	0.699	$b^{exp350}$	0.538
$\sqrt[3]{t_{det}^{green}}$	$E_D^{exp}  _{t=18.3}$	0.549	$E_D^{drag350}  _{t=9.4}$	0.46	$f^{mdrag}  _{t=12.5}$	0.745
$\sqrt[3]{t_{50}^{red}}$	$b^{exp350}$	0.501	$a^{exp}$	0.05	$p_1^{exp350}  _{t=200}$	0.493

\* evaluated at the time indicated in the shockwave feature

The fireball and shockwave features show a much higher degree of correlation with each other than with the munitions characteristics. This makes sense because the high degree of variability in the features causes a decrease in the overall correlation with the unchanging munitions characteristics. When comparing fireball and shockwave features, the variability is removed to some extent; for example, a larger fireball in the NIR is generally indicative of a more efficient detonation. This is significant because although there are large variations in the shockwave and fireballs produced from similar explosives, the variability is consistent in features of both. This is shown in Figure 50 for some of the more highly correlated features using all munitions events.

There is little diversity in the shockwave features that are most highly correlated with the fireball features. The detonation energy as a function of time is the most common shockwave feature for all munitions and the group of TNT and Composition B, typically at early to mid times after detonation (when the shockwave is in the early part of the far-field). The radius of the shock at early times (less than 2 milliseconds) and the efficiency in the mid-field are also highly correlated with features of the fireball, but for all groups of munitions. These three features are represented in Figure 50, along with the shock 350 model's  $b$  fit parameter for all munitions detonations.

Much of what is shown in the figure is straightforward: at a given time, the larger the radius of the shock, the longer it takes for the fireball to decay to 50% of its maximum area (upper right plot). Both of these features are indicative of a higher energy detonation, where the energy in the shock contributes to velocity (thus greater radius) and energy in the fireball contributes to a longer duration. The same phenomenon is observed when comparing the energy of the shock with the fireball area (lower left plot). The

trend isn't nearly as clear, but higher energy does correlate with a larger fireball.

When C-4 is excluded from the comparisons, the correlation is not largely affected. Some of the fireball features are more highly correlated with other shockwave features or are correlated at different times, but overall the exclusion of C-4 has little impact, which is in contrast to the effect of removing C-4 from comparisons of features with munitions characteristics. This indicates that although C-4 has some properties that affect the fireball and shock features differently than TNT and Composition B do, the relationship between the fireball and shockwave is fairly independent of whether C-4 is

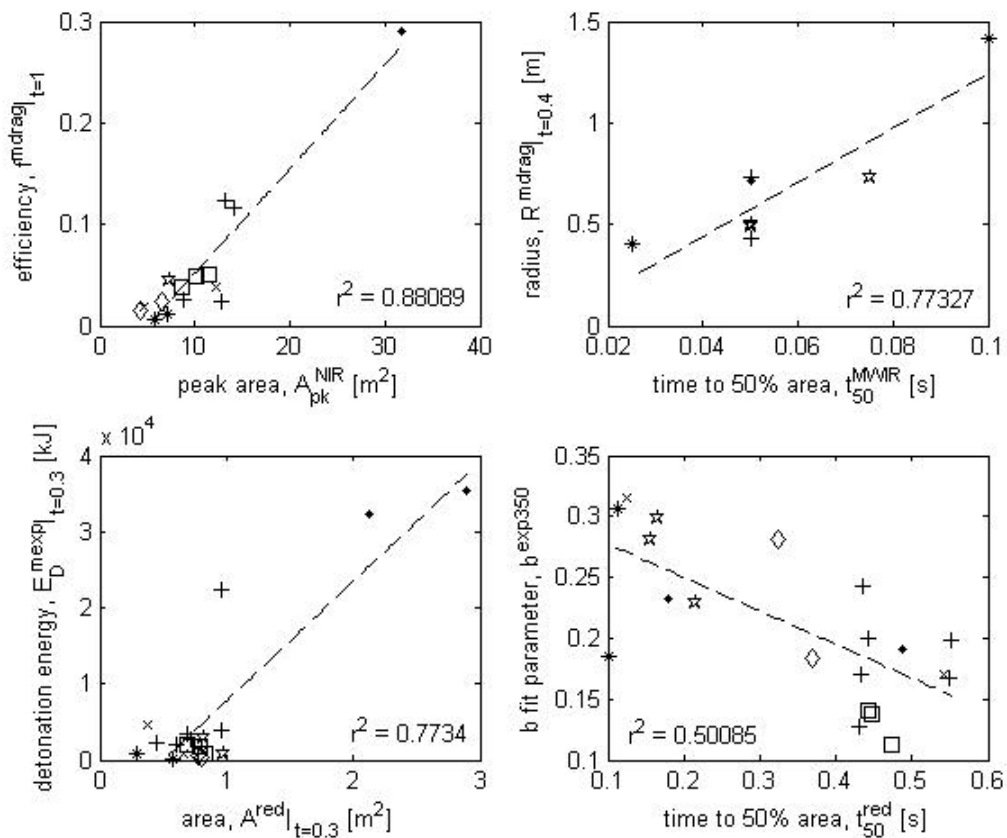


Figure 50: Selected comparisons of fireball and shockwave features are shown for detonations of all munitions. In general, the fireball and shockwave features have a greater degree of correlation with each other than with munitions characteristics, as indicated by the higher coefficients of determination. The trends in the data are also fairly evident.

included. Several of these feature comparisons are shown in Figure 51 for TNT and Composition B events, with the trends previously discussed remaining unaltered.

In contrast to excluding C-4, it is evident that shockwave and fireball features have the strongest correlation when only TNT is examined. For these comparisons, the detonation energy as a function of time does not appear as one of the most correlated features. This does not imply that the correlation of the detonation energy with the fireball features decreased – it is still one of the most highly correlated features – but it was often replaced by the drag 350 model’s  $a$  fit parameter or the efficiency as the most highly correlated feature. For  $a^{drag350}$ , this is largely due to the poor overlap in the

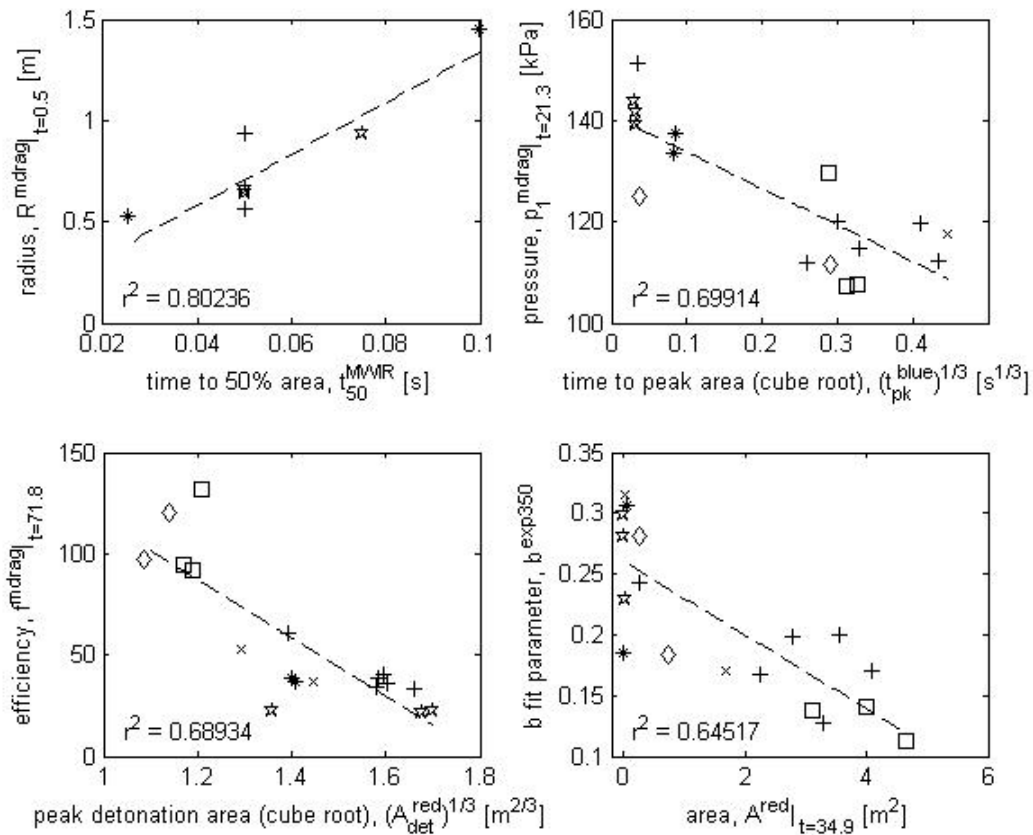


Figure 51: Selected comparisons of fireball and shockwave features are shown for detonations of TNT and Composition B munitions. The degree of correlation is not significantly affected by excluding C-4, indicating that the relationship between the fireball and shockwave is explosive composition independent.



acquisition of events by the MWIR and RGB instruments, which resulted in only three events being able to be compared. This can be seen in Figure 52, along with other highly correlated features. There is a definite trend, but more data points are required to make any conclusions regarding correlation between features in the MWIR and shockwave features.

Looking at the efficiencies, 155mm TNT is clustered at low efficiencies with high peak detonation areas (in contrast to 105mm being clustered at high efficiencies and low detonation areas, in the lower left plot). This is further evidence that these two features relate to the initial mass of the explosive. While this is necessarily true for all correlated

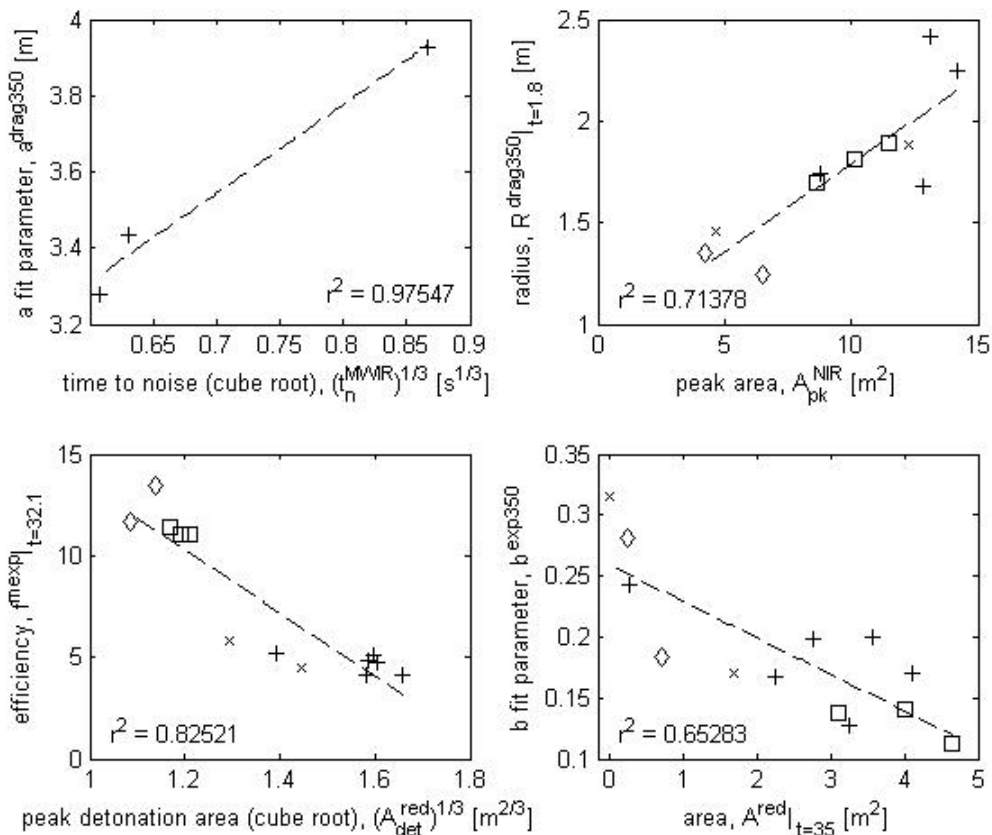


Figure 52: Selected comparisons of fireball and shockwave features are shown for TNT detonations only. The correlation between the features is the highest when only a single explosive composition is used and there are very clear trends.

fireball and shockwave features (because the features are dependent on the originating explosive material) it is especially clear in this case that the correlation is more than a result of variability in the detonations. The peak detonation area being large when efficiency is small is not independent of munitions weight; both area and efficiency depend on the mass of the explosive. This is in contrast to the peak area in the NIR's correlation to the drag 350 model's radius at 1.8 milliseconds (upper right plot).

Although both features depend on the munitions characteristics, the munitions types show a range of values and the relationship of the features is largely due to variations in the detonation.

### **Summary**

Fireball area profiles and extracted features show a great deal of variation, even for detonations of the same weight, orientation, and explosive composition. Despite this, a number of moderately reproducible features are present. These are primarily at times within the first ten milliseconds after detonation and include the detonation area and time to the peak detonation area in the RGB bands. Even though reproducibility isn't high, it decreases further as different types of munitions are examined together, indicating that there is separation that may be exploited for classification.

The shockwave fits and features behave in the opposite manner: reproducibility is lowest at early times and increases as the shock propagates. This is true of all the shockwave fit functions (from which the shockwave features were derived). The basic drag and shock models are fairly accurate initially, and although precise, are inaccurate in their late time predications. The modified drag and shock models are the best

representations of the true propagation of the shockwave at all times. They accurately predict the far-field transition to an acoustic wave that is similar for all munitions detonations, making features extracted at late times poor for classification.

Distinguishability was first attempted on broad classes of combustion events that were markedly different (munitions detonations, DTSS plumes, and muzzle flashes) followed by simple events of different types within a class (muzzle flashes). While the method used is not a robust classification technique, it does demonstrate the ability to distinguish type based on separability in the feature values. This is more complex for munitions groups, yet proves highly effective when using the detonation efficiency. Although not as discriminating, detonation area, initial Mach number, and the time to the peak detonation area are useful for separating weight; distinguishing between explosive compositions shows promise using the peak fireball area and mid-field shockwave pressure.

Finally, by examining correlations amongst the fireball, shockwave, and munitions features, a number of trends were found. Higher mass and specific energy in the explosive causes the shockwave pressure and velocity to increase, while increasing mass causes a decrease in detonation efficiency. Many of the correlations between fireball and shockwave features are related directly to the aforementioned munitions features on which they depend. Trends that do not depend on munition characteristics to any appreciable extent, however, are those that relate variability in the fireball to variability in the shockwave. Correlated features just as often indicate that when one feature value changes, the other changes in a consistent manner, independent of munitions type.

## V. Conclusions and Recommendations

### Chapter Overview

The predictions based on the simple theory of an ideal detonation are remarkably different than the effects generated by a real-world munitions detonation. Even under the best of circumstances, military and improvised explosives are highly irreproducible. Factor in situational effects like atmosphere, terrain, target, etc. and the task of identifying an explosive munition based on its fireball or shockwave characteristics seems insurmountable. However, this is not necessarily the case; the problem is difficult because detonations of high explosives are highly irreproducible, but there are a number of features that show promise. By identifying and studying these features, insight into what seems a complex phenomenon is reduced to the realm of academia. A complete understanding of the physics behind detonations is far from achieved, but by asking the right question, progress has been made.

This work asked and attempted to answer three questions regarding detonations:

1. Which features are reproducible for munitions of the same type, yet different for munitions of dissimilar types?
2. Which features of the shockwave and fireball are highly correlated with characteristics of the explosive material?
3. How are features of the shockwave related to features of the afterburn fireball?

The following sections summarize previous and ongoing efforts, what has been learned in this endeavor, and what is left to be explored.

## Previous Work

The ability to identify combustion events from remotely sensed emissions is limited. Classes of events – such as detonations, missile plumes, or muzzle flashes – can be distinguished with a high degree of confidence because they are phenomenologically very different. Distinguishing between types within the same class, however, is much more challenging and requires an understanding of phenomenology to ascertain which features are unique to particular characteristics of the type. There is good understanding of shockwaves resulting from high explosive detonations – accurate models were developed nearly forty years ago and are still in use. While this provides a number of features for use in identifying munitions types, shockwaves are difficult to monitor remotely. Hence, it is the fireball resulting from a high explosive detonation that has the best potential for observation and classification.

Unfortunately, fireball phenomenology has been little studied and less understood. Hydrodynamic models of fireballs have been developed [32], but there are no corresponding models of the emissions. The Air Force began investigating classification of munitions detonations in the early 1990s, with the result being a limited understanding of fireball emissions in the infrared [33][34][35]. Ongoing work by Kevin Gross at the Air Force Institute of Technology has characterized cased munitions detonation fireballs as Planckian, gray-body radiators with a number of CO<sub>2</sub> spectral emissions [36]. Major Andy Dills and Kevin Gross have investigated using spectral and imagery features based on these emissions for robustly classifying munitions detonations [14][37]. This research expands the current understanding of detonation events and contributes to the classification of munitions detonations.

## Conclusions

A number of conclusions can be made regarding the characteristics and features of afterburn fireballs and shockwaves resulting from explosive munitions detonations.

These are summarized below:

1. Classification using the current visible imagery techniques is best accomplished very shortly after detonation (1-10 milliseconds).
2. Mass may be best differentiated using the visible detonation area, initial Mach number, or time to the peak detonation area.
3. Composition may be best differentiated using the time to the peak fireball area in the visible or drag model fit parameters.
4. Fireball and shockwave features show a high degree of correlation, independent of variability in the detonation.
5. Classical drag and shock models may be accurately extended into the far-field by adding a constant velocity (ambient speed of sound) term.

Detonations of a specific type of munition under similar conditions have highly variable results. This is evidenced in the area profiles having nearly the same amount of variability within a single type as for entire groups of munitions – the individual types' characteristics may have a direct relationship to the effects they produce, but the variability in these effects is greater than the differences in these effects between types. Despite this, there are certain aspects of the fireball imagery that are reproducible and do show promise for classification. These are primarily in the first ten milliseconds and involve the features of the detonation emissions, such as total area ( $C_V < 0.2$ ) or time to peak ( $C_V < 0.25$ ), as opposed to features of the afterburn fireball ( $C_V > 0.5$ ).

In contrast to the fireball, the shockwave characteristics are highly reproducible and become more reproducible as time progresses ( $C_V < 0.05$  after 10 milliseconds). This is true even for groups containing many munitions weights, orientations and compositions because the shockwave decays very quickly to an acoustic wave that lacks identifiable characteristics of the detonation that caused it. While this late-time shockwave has excellent reproducibility, it is nearly useless for developing a phenomenology because it cannot be correlated with any particular characteristics of its originating munition. Thus, like features extracted from the fireball, it is the early-time behavior that provides the most direct link to munitions features.

The fact that the most reproducible and distinguishable features of the shockwave and the fireball occur at early times is not surprising. Shortly after detonation, reaction byproducts begin to mix with the atmosphere in seemingly chaotic ways – governed by turbulence, temperature gradients, and other irreproducible processes. These atmospheric effects are the most likely (although not the only) cause of variability in the mid-to late-time behavior of the fireball and shockwave. Acquiring detonation features shortly after detonation (1-10 milliseconds) – while the features are still fairly consistent for a type of munition – offers the best promise for classification.

Because of the limited number of detonations of each type of munition, it is premature to say which of the extracted features are ideal for classification. It can be said, however, that a number of features show a good deal of promise. Depending on the extent of *a priori* information available, features can be chosen that show good separation for different weights of explosives, such as detonation area ( $FR < 7$ ), initial Mach number or pressure ( $FR < 10$ ), or time to the peak detonation area ( $FR < 3$ ). TNT and

Composition B may be distinguished using the time to the peak fireball area in the visible ( $FR < 2$ ), or several of the fit parameters:  $b^{drag}$  ( $FR \sim 1.5$ ),  $a^{drag}$  ( $FR \sim 1.36$ ), and  $a^{mexp}$  ( $FR \sim 1.1$ ). These features showed a definite correlation with characteristics of the explosive munition, and it is continuing to identify these correlations that will guide which features should be chosen. Furthermore, knowing which features of the fireball and shockwave are correlated to each other guides which feature should not be used together (because correlated features are both representative of the same munitions characteristic, thus providing redundant information).

In general, detonations didn't show a high degree of correlation between munitions characteristics and features of the fireball and shockwave (with the exception of efficiency). It is likely that this was because of the variability in the detonations themselves and the uncertainties in the measurements as opposed to lack of correlation, evidenced by the trends clearly seen in the data ( $r^2 < 0.6$ ). Furthermore, correlation improved as C-4 was excluded, although most of the same trends were present ( $r^2 < 0.7$ ). This increase in correlation was indicative that the C-4 detonations had properties that were noticeably different, and it may be possible to explore these for use in distinguishing between explosives containing TNT (such as Composition B) and C-4. When only TNT was examined, correlation improved even more. This was largely due to the fact that there were only two samples of munitions features in this group (the two weights of TNT) which provided less information on feature correlation than it did on separability.

Many of the correlations found amongst features of the fireball, shockwave, and munitions were what would be expected from theory: Detonation velocity and shock



pressure increased with the total energy released (linear  $r^2 \sim 0.5-0.8$ ), detonation areas and duration increased with detonation and afterburn energies (cubic  $r^2 \sim 0.3-0.8$ ), and the characteristic radius of the shockwave increased with detonation energy and mass (linear  $r^2 \sim 0.1-0.6$ ). Less obvious correlations were also found: Time to the peak fireball area decreased with increasing heat of detonation (cubic  $r^2 \sim 0.4-0.7$ ), and detonation efficiency decreased with increasing mass (linear  $r^2 \sim 0.7-0.99$ ). The first of these signifies that as more energy is released in the initial detonation, the reactants are consumed at a greater rate and the combustion process causes the area to peak more quickly. Hypotheses for this include higher temperatures inducing faster rates of reaction or a greater fraction of the energy (reactant material) being consumed in the detonation as opposed to the fireball. This does not affect the fireball's duration; however, in general the fireball burns longer when detonation energies are higher, even if it does peak more quickly.

The latter is indicative that as the mass increases, the detonation becomes less ideal – the assumptions of a point mass and instantaneous detonation become less accurate – and that a non-ideality not covered in the theory is that larger masses do not detonate as efficiently. This results in a lower overpressure shock than would be expected, and in turn the calculated efficiency is lower. Two possible explanations for this are the expulsion of uncombusted reactants due to explosive forces, or energy being released on a longer timescale (due to the extended dimension of the mass).

Alternatively, the efficiency could decrease with mass because larger masses generate greater energies, which drives the shockwave away from the munitions more quickly. If the afterburn energy is sustaining the shockwave, it will do so to a lesser extent in higher

mass detonations because the shockwave' proximity to the fireball will decrease more quickly. More observations of a greater number of events are required to verify these, however.

When compared with each other, the fireball and shockwave features generally had greater correlation than either did with munitions characteristics ( $r^2 \sim 0.5-0.9$ ). This is most likely due to the fact that all of the fireball and shockwave features are dependent on the same munitions characteristics, and so the fireball and shockwave should be nearly as correlated with each other as they are with the munitions characteristics on which they depend. Correlation is further improved, however, because variability is removed. As the fireball and shockwave differ from detonation to detonation, they vary in the same manner – a less efficient (or lower energy) detonation will consequently have a lower energy shockwave and fireball, for example – and so the features themselves are correlated independent of variations in the detonation.

Additionally, correlation between the extracted features extends beyond the early-times that were important for reproducibility of fireball features and distinguishability of shockwave features. Even though fireballs are highly irreproducible and lose many of their identifying characteristics in mid to late times, and shockwaves all tend towards fairly indistinguishable acoustic waves in the same timescale, the rate at which these transitions occur and their feature values shows definite trends: as mid-time pressure increases the cube root of the time to the peak fireball area in the NIR decreases, as near-field shock radius increases the size and duration of the fireball in the MWIR increases, etc. While inadequate for classification, these trends provide insight into the relationship between fireball and shockwave dynamics.

While not the focus of this research, modeling the shockwave's position as a function of time beyond the mid-field was accomplished by adding a constant velocity term to the drag and shock models of the shock's velocity. The value of this term was the ambient speed of sound because the velocity of the shockwave asymptotically approaches the speed of sound rather than zero at long times. Although the classical models were derived for the near and mid-fields, the modification used here gave excellent agreement with experimental observations ( $r^2 > 0.997$  in the near- and mid-fields, less than 10% error in the far-field).

### **Recommendations for Future Work**

Although sixty-five detonation events were examined, they were divided across nine arrangements of munitions. Combined with the fact that approximately half of the detonations were not recorded in the MWIR and RGB (and that with a handful of exceptions those that were recorded did not overlap), this yielded an incredibly sparse sampling of values for the majority of the features used. While comparisons were made and conclusions were drawn, they should be treated with care. A much larger sampling of feature values is required before any of the trends, scaling rules, or distinguishing features are accepted as an accurate assessment of detonation phenomena.

Furthermore, the only comparisons made were between features of the fireball, shockwave, and munitions. While this provided information on munitions dependencies and allowed trends to be seen – which is useful to the classification problem – it did not provide information on spectral dependencies of detonation fireballs, i.e. how the fireball's appearance in one band related to the appearance in other bands. It would be

particularly interesting, and useful to developing a phenomenology of fireball emissions, to see how the sizes, peak times, and durations were correlated amongst the RGB, NIR, and MWIR bands.

The functions used to model the propagation of the shockwave as a function of time – both the originals and modifications of the originals– accurately fit the observed data in the near and mid-fields. Because the fit data include far-field data as well, however, the functions from the literature did not perform as well as the modified functions presented here, presumably because the literature’s functions were based solely on near-and mid-field approximations. The excellent agreement between the modified forms and all of the data – near-, mid-, and orders of magnitude of far-fields – indicate that the physical assumptions used as the foundation for these modifications are valid, and that the models may be used to predict shockwave propagation in all fields. To validate this, however, shockwave positions as a function of time should be acquired with much greater accuracy at much higher sampling to determine exactly how well the various models agree in all fields, or, alternatively, which models give the best agreement in which fields. This is feasible with existing data sets and simply requires a more in-depth study.

A wider variety of correlation functions should also be employed. Correlation between the munitions and shockwave features was only calculated assuming a linear relationship, and correlation of these features with the fireball was based on linearity with the fireball features and their second and third roots. Since physical behavior is rarely governed simply by linear, quadratic, and cubic relationships, other correlations should be examined. These may reveal a high degree of correlation.

Of the features for which the reproducibility, distinguishability, and correlation were calculated for, only a small fraction of them were examined, and even fewer were studied in detail. There is a lot that can be learned about the phenomenology of detonations – especially the scaling of fireball and shockwave characteristics with munitions characteristics – by taking a closer look at the physicality of the features and their correlations. This would require choosing specific features to examine and developing a theoretical understanding using a more statistically meaningful sampling of values. The work presented here is the first step, since it guides which features show promise, but a much more in-depth analysis is necessary.

Once further analysis of promising features from this research is exhausted, additional features can be extracted from the imagery. These include identifying the magnitude of the smaller peak in the RGB area profile and its time of occurrence, the total integrated area of portions of the profile (such as the primary and secondary peaks), or investigating the use of the other area profiles presented. There are a multitude of additional features in the data, many of which may prove to be more useful than those examined here. These should be explored for their correlation to munitions characteristics.

Finally, for this work to be of practical use, the features that show promise for classification should be analyzed in a more rigorous way. The method employed here was simplistic: it assumed normally distributed feature values and only compared two munitions groups using a single extracted feature. Classification techniques that have been previously developed should be applied so that feature distinguishability for explosive detonations does not remain at an academic level but becomes feasible.

To summarize, the following remains to be completed:

1. additional tests with a larger sampling of feature values
2. compare features across multiple bands to determine spectral dependences
3. verify shockwave fit functions with more accurate measurements
4. test additional functional forms of the correlation between features
5. develop theoretical foundation for correlations seen in the data
6. identify and analyze additional features
7. employ more rigorous classification techniques to promising features

## Summary

All characteristics of the shockwave and fireball are directly related to the characteristics of the originating explosive munition. These characteristics, while highly variable based on variations in the detonation ( $C_V > 0.5$  typical), show the same degree of variability; i.e. fireball features scale with shockwave features independent of munition type ( $r^2 \sim 0.5-0.9$ ). Furthermore, despite the range of feature values obtained even for munitions of the same type, many of the features show a high degree of separation between types ( $FR > 2$ ). This is primarily at early times – within the first ten milliseconds – before the shockwave decays to an indistinguishable acoustic wave and the fireball is affected by atmospheric effects which obscure its originating distinctiveness. Systems used to obtain information for the classification of munitions detonations should be engineered so that they can acquire these early-time features.

Most of the observed phenomenology was not surprising. As the mass or specific energy of the explosive munition increased (and thus energy released), the resulting

shockwave had higher pressure and velocity ( $r^2 \sim 0.4-0.8$ ); the afterburn fireball was larger and had a longer duration ( $r^2 \sim 0.2-0.7$ ). These relations were fairly consistent across all bands. Not so obvious were that as the heat of detonation increased, the time to the peak fireball area decreased ( $r^2 \sim 0.4-0.65$ ); as mass increased the efficiency of energy transferred to the shockwave decreased ( $r^2 \sim 0.7-0.99$ ). Phenomenological models of fireball emissions were not developed, but definite trends in fireball features with munitions and shockwave characteristics were observed. These trends should be noted so that correlated features are not used together in classification, yet are connected in development of the underlying physics.

This research effort, while not identifying definitive classification features or developing predictive, physics based phenomenological models (although the modifications to the basic shockwave propagation models do show utility), has identified a number of features with decent reproducibility and high separation. Trends were evident and, with care, may be used to approximate how changing munitions characteristics will affect the resulting fireball and shockwave. All of these show promise and, in addition to contributing to current understanding, will point the way towards a deeper understanding of detonation physics in future research.

## Appendix 1: Instrument Settings

This section contains selected instrument settings for the Bronze Scorpio, Dual Thrust Smokey SAM, and Muzzle Flash field tests.

### Bronze Scorpio: Cincinnati Electronics IRRIS 256 IR Imager

Detector	InSb
Band	3-5 $\mu\text{m}$
Frame-rate	40 Hz
Pixel dimension	30 $\mu\text{m}$
Focal length	50 mm
Distance	1076 m
Resolution	256 x 256
Dynamic Range	12-bit
IFOV	0.6 mrad
FFOV	8.80 x 8.80 deg 165.28 x 165.28 m

### Bronze Scorpio: Phantom Camera

Detector	SR-CMOS
Band	RGB (proprietary bandpass)
Pixel dimension	22 $\mu\text{m}$
Focal length	400 mm
Distance	1076 m
Dynamic Range	24-bit (8-bit in 3 channels)



IFOV

55  $\mu$ rad

Table 24: The Phantom camera's resolution, full field of view, integration time, and framerate are given for each detonation event in the Bronze Scorpio tests.

Event	Resolution	FFOV (deg)	FFOV (m)	Integration Time ( $\mu$ s)	Frame-rate (Hz)
1	512 x 384	1.61 x 1.21	30.30 x 22.73	121	7500
3	512 x 384	1.61 x 1.21	30.30 x 22.73	121	7500
5	512 x 384	1.61 x 1.21	30.30 x 22.73	121	7500
7	512 x 384	1.61 x 1.21	30.30 x 22.73	121	7500
9	512 x 384	1.61 x 1.21	30.30 x 22.73	90	10000
11	512 x 384	1.61 x 1.21	30.30 x 22.73	90	10000
13	512 x 384	1.61 x 1.21	30.30 x 22.73	90	10000
15	512 x 384	1.61 x 1.21	30.30 x 22.73	90	10000
17	512 x 384	1.61 x 1.21	30.30 x 22.73	90	10000
19	512 x 384	1.61 x 1.21	30.30 x 22.73	90	10000
21	512 x 384	1.61 x 1.21	30.30 x 22.73	90	10000
23	512 x 384	1.61 x 1.21	30.30 x 22.73	90	10000
27	800 x 600	2.52 x 1.89	47.34 x 35.51	192	4800
29	800 x 600	2.52 x 1.89	47.34 x 35.51	192	4800
33	800 x 600	2.52 x 1.89	47.34 x 35.51	192	4800
35	800 x 600	2.52 x 1.89	47.34 x 35.51	192	4800
39	800 x 600	2.52 x 1.89	47.34 x 35.51	192	4800
42	800 x 600	2.52 x 1.89	47.34 x 35.51	192	4800
43	800 x 600	2.52 x 1.89	47.34 x 35.51	192	4800
46	800 x 600	2.52 x 1.89	47.34 x 35.51	192	4800
47	800 x 600	2.52 x 1.89	47.34 x 35.51	192	4800
52	320 x 240	1.00 x 0.76	18.94 x 14.20	36	24200
53	640 x 480	2.02 x 1.51	37.88 x 28.41	36	7270
54	800 x 600	2.52 x 1.89	47.34 x 35.51	36	4800
56	320 x 240	1.00 x 0.76	18.94 x 14.20	36	24200
57	320 x 240	1.00 x 0.76	18.94 x 14.20	36	24200
59	320 x 240	1.00 x 0.76	18.94 x 14.20	36	24200
61	256 x 256	0.81 x 0.81	15.15 x 15.15	32	26900
65	256 x 256	0.81 x 0.81	15.15 x 15.15	13	26900

**Bronze Scorpio: Indigo Alpha NIR Imager**

Detector	InGaAs
Band	900-1700 nm
Frame-rate	~30 Hz
Pixel dimension	30 $\mu$ m
Distance	1076 m

Resolution	320 x 256
Dynamic Range	12-bit

Table 25: The Indigo imager's instantaneous field of view, focal length, and full field of view are given for each detonation event in the Bronze Scorpio tests.

Event	I FOV (mrad)	Focal Length (mm)	FFOV (deg)	FFOV (m)
1-24	0.1	300	1.83 x 1.47	34.43 x 27.55
25-26	0.12	250	2.20 x 1.76	41.32 x 33.05
27-65	0.15	200	2.75 x 2.20	51.65 x 41.32

### Dual Thrust Smokey SAM: Indigo Alpha NIR Imager

Detector	InGaAs
Band	900-1700 nm
Frame-rate	~18 Hz
Integration Time	100 $\mu$ s
F/#	1.8
Pixel dimension	30 $\mu$ m
Focal Length	75 mm
Distance	42.38 m
Resolution	320 x 256
Dynamic Range	12-bit
I FOV	0.4 mrad
FFOV	7.33 x 5.87 deg 5.42 x 4.34 m

### Muzzle Flash: Indigo Alpha NIR Imager (perpendicular view)

Detector	InGaAs
Band	900-1700 nm

Frame-rate	11~18 Hz
Integration Time	33 ms
F/#	8
Pixel dimension	30 $\mu$ m
Focal Length	75 mm
Distance	181 cm
Resolution	320 x 256
Dynamic Range	12-bit
I FOV	0.4 mrad
FFOV	7.33 x 5.87 deg
	23.17 x 18.53 cm

## Appendix 2: Fit Parameters

The mean and standard deviation of the fit parameters and their uncertainties are shown for each group of munitions and each model. The types of munitions in each group are shown in Table 26.

Table 26: Munitions groups

Munitions types	Group
155mm TNT erect	1
155mm TNT prone	2
105mm TNT erect	3
105mm TNT prone	4
155mm TNT	5
105mm TNT	6
all TNT	7
2x155mm Comp. B	8
all Comp. B	9
all TNT & Comp. B	10
all munitions	11

### Drag Model

The mean fit parameters and uncertainties are shown for the drag model,

$$R(t) = a \cdot (1 - e^{-bt}), \text{ in Table 27.}$$

Table 27: Drag model fit parameters and uncertainties.

Group	$a$	$\sigma_a$	$b$	$\sigma_b$
1	28.249 ±7.529	3.028 ±0.705	29.723 ±18.581	5.601 ±5.260
2	27.990 ±7.600	3.276 ±0.905	30.126 ±18.428	5.934 ±5.109
3	28.291 ±7.459	3.290 ±0.761	28.463 ±18.865	5.607 ±5.232
4	32.452 ±10.728	4.690 ±3.172	25.605 ±20.460	5.357 ±5.377
5	28.694 ±6.586	3.222 ±0.793	28.112 ±16.060	5.264 ±4.494
6	30.786 ±9.292	4.354 ±2.792	25.773 ±17.209	5.222 ±4.512
7	30.900 ±7.344	3.923 ±2.230	24.449 ±13.528	4.550 ±3.591
8	29.816 ±8.601	3.862 ±2.342	26.926 ±16.300	4.868 ±3.621
9	25.905 ±10.665	3.391 ±2.598	37.160 ±23.437	6.404 ±4.163
10	27.343 ±9.407	3.347 ±2.200	33.041 ±20.965	5.590 ±3.771
11	26.707 ±9.326	3.258 ±2.103	35.045 ±22.081	6.307 ±4.867

## Modified Drag Model

The mean fit parameters and uncertainties are shown for the modified drag model,

$$R(t) = a \cdot (1 - e^{-bt}) + c \cdot t, \text{ in Table 28.}$$

Table 28: Modified drag model fit parameters and uncertainties.

Group	$a$	$\sigma_a$	$b$	$\sigma_b$	$c$	$\sigma_c$
1	3.01 ±0.54	0.19 ±0.11	487.12 ±274.81	98.12 ±50.16	375.33 ±19.63	6.48 ±3.08
2	2.91 ±0.52	0.16 ±0.09	518.18 ±258.26	96.57 ±57.34	380.53 ±21.33	5.98 ±3.44
3	2.53 ±0.45	0.20 ±0.15	5.4E7 ±1.3E8	115.96 ±75.96	374.98 ±22.51	7.50 ±5.55
4	2.52 ±0.46	0.20 ±0.12	487.85 ±278.64	140.80 ±123.91	374.65 ±21.38	6.74 ±3.45
5	2.95 ±0.48	0.19 ±0.10	472.91 ±233.96	99.29 ±48.79	377.73 ±18.84	6.670 ±3.36
6	2.37 ±0.41	0.25 ±0.13	4.1E7 ±1.2E8	156.46 ±103.77	378.05 ±21.32	8.80 ±4.47
7	2.68 ±0.57	0.23 ±0.12	2.5E7 ±9.1E7	127.94 ±90.078	374.01 ±17.38	7.83 ±4.14
8	2.49 ±0.64	0.24 ±0.14	2.5E7 ±9.1E7	141.94 ±109.09	377.88 ±18.75	8.48 ±4.87
9	2.34 ±0.48	0.23 ±0.14	2.5E7 ±9.1E7	150.40 ±107.71	386.17 ±19.70	9.38 ±4.31
10	2.57 ±0.59	0.22 ±0.13	1.8E7 ±7.7E7	131.48 ±97.32	380.99 ±18.81	8.52 ±4.23
11	2.66 ±0.63	0.22 ±0.13	1.6E7 ±7.3E7	143.73 ±118.17	383.78 ±20.79	8.61 ±4.52

## Drag350 Model

The mean fit parameters and uncertainties are shown for the drag350 model,

$$R(t) = a \cdot (1 - e^{-bt}) + c_0 \cdot t, \text{ Table 29.}$$

Table 29: Drag350 model fit parameters and uncertainties.

Group	$a$	$\sigma_a$	$b$	$\sigma_b$
1	3.760 ±0.462	0.112 ±0.033	262.142 ±91.996	41.584 ±22.277
2	3.798 ±0.412	0.125 ±0.062	262.797 ±99.093	41.041 ±22.544
3	3.249 ±0.400	0.094 ±0.038	297.134 ±73.493	44.797 ±24.222
4	3.264 ±0.378	0.126 ±0.060	246.605 ±99.576	44.911 ±24.896
5	3.809 ±0.434	0.127 ±0.053	245.109 ±90.129	38.820 ±19.608
6	3.248 ±0.487	0.134 ±0.069	255.375 ±98.192	43.690 ±20.503
7	3.482 ±0.547	0.123 ±0.058	246.506 ±84.041	39.870 ±18.003
8	3.385 ±0.491	0.114 ±0.060	254.749 ±80.525	38.819 ±18.607
9	3.309 ±0.415	0.117 ±0.058	267.815 ±81.825	40.429 ±19.526
10	3.461 ±0.481	0.114 ±0.052	257.954 ±76.896	38.576 ±17.788
11	3.589 ±0.604	0.125 ±0.067	262.228 ±74.670	44.315 ±30.514

## Explosive Model

The mean fit parameters and uncertainties are shown for the explosive model,

$$R(t) = a \cdot t^b, \text{ in Table 30.}$$

Table 30: Explosive model fit parameters and uncertainties.

Group	$a$	$\sigma_a$	$b$	$\sigma_b$
1	172.574 ±28.925	10.570 ±1.344	0.706 ±0.049	0.018 ±0.004
2	173.567 ±31.121	11.037 ±2.194	0.706 ±0.049	0.018 ±0.004
3	174.051 ±26.569	10.311 ±2.481	0.718 ±0.044	0.017 ±0.005
4	190.195 ±39.726	13.040 ±5.944	0.742 ±0.065	0.020 ±0.007
5	176.998 ±27.422	11.007 ±1.903	0.712 ±0.044	0.018 ±0.003
6	186.984 ±35.503	12.637 ±5.383	0.738 ±0.057	0.019 ±0.006
7	185.246 ±29.060	11.706 ±4.341	0.731 ±0.049	0.018 ±0.005
8	182.464 ±30.554	11.030 ±4.863	0.729 ±0.050	0.017 ±0.006
9	171.328 ±37.062	10.370 ±5.410	0.713 ±0.061	0.016 ±0.007
10	174.422 ±32.701	10.327 ±4.580	0.715 ±0.054	0.016 ±0.006
11	170.148 ±34.860	10.628 ±4.511	0.704 ±0.063	0.017 ±0.007

## Modified Explosive Model

The mean fit parameters and uncertainties are shown for the modified explosive

model,  $R(t) = a \cdot t^b + c \cdot t$ , in Table 31.

Table 31: Modified explosive model fit parameters and uncertainties.

Group	$a$	$\sigma_a$	$b$	$\sigma_b$	$c$	$\sigma_c$
1	13.97 ±4.97	6.46 ±5.12	0.30 ±0.05	0.08 ±0.05	316.97 ±19.83	26.12 ±15.56
2	13.03 ±2.46	4.89 ±3.98	0.29 ±0.04	0.06 ±0.04	323.75 ±13.98	21.05 ±13.90
3	12.49 ±1.63	4.18 ±3.25	0.30 ±0.03	0.06 ±0.05	316.14 ±17.16	18.14 ±13.05
4	11.40 ±4.50	5.75 ±3.95	0.28 ±0.08	0.11 ±0.09	327.77 ±25.52	24.91 ±13.83
5	14.07 ±4.41	6.64 ±5.06	0.30 ±0.05	0.08 ±0.04	319.34 ±17.58	26.34 ±15.83
6	12.45 ±4.31	6.20 ±4.20	0.30 ±0.08	0.10 ±0.08	322.43 ±24.67	25.62 ±14.47
7	13.33 ±4.58	6.64 ±4.43	0.30 ±0.06	0.10 ±0.07	318.42 ±22.03	26.64 ±14.60
8	15.96 ±10.98	6.02 ±4.02	0.32 ±0.09	0.08 ±0.07	309.60 ±38.63	23.53 ±13.30
9	21.25 ±16.83	7.23 ±4.72	0.35 ±0.11	0.08 ±0.07	292.60 ±59.42	26.76 ±13.78
10	19.44 ±14.67	7.26 ±4.70	0.34 ±0.10	0.08 ±0.06	298.00 ±51.43	27.18 ±14.05
11	18.68 ±14.08	6.82 ±4.66	0.33 ±0.10	0.08 ±0.06	302.24 ±50.43	26.66 ±13.94

## Explosive350 Model

The mean fit parameters and uncertainties are shown for the explosive350 model,

$$R(t) = a \cdot t^b + c_0 \cdot t, \text{ Table 32.}$$

Table 32: Explosive350 model fit parameters and uncertainties.

Group	$a$	$\sigma_a$	$b$	$\sigma_b$
1	7.236 ±1.303	0.631 ±0.274	0.184 ±0.039	0.023 ±0.011
2	8.021 ±2.392	0.653 ±0.492	0.204 ±0.067	0.019 ±0.010
3	6.048 ±1.901	0.488 ±0.216	0.167 ±0.047	0.022 ±0.013
4	6.684 ±1.627	0.785 ±0.619	0.202 ±0.052	0.032 ±0.024
5	7.795 ±2.168	0.719 ±0.439	0.199 ±0.057	0.023 ±0.010
6	6.796 ±2.797	0.833 ±0.629	0.198 ±0.074	0.031 ±0.020
7	6.823 ±2.220	0.775 ±0.511	0.188 ±0.060	0.029 ±0.016
8	7.016 ±2.435	0.753 ±0.513	0.198 ±0.068	0.027 ±0.016
9	7.975 ±3.075	0.844 ±0.517	0.222 ±0.071	0.027 ±0.017
10	7.667 ±2.682	0.799 ±0.460	0.208 ±0.065	0.026 ±0.015
11	7.975 ±2.732	0.783 ±0.449	0.209 ±0.062	0.025 ±0.014

## Bibliography

1. Marvin E. Bauer. "Spectral Inputs to Crop Identification and Condition Assessment," Proceeding of the IEEE. 73 (6), 1071-1085 (1985).
2. Theodore Saunders, Jay Feuquay, and John A. Kelmelis. "The U.S. Geological Survey Land Remote Sensing Program," *Mark Cartography and Geographic Information Science*. 30 (2), 211-215 (2003).
3. Martin Herald, Margaret E. Gardner, and Dar A. Roberts. "Spectral Resolution Requirements for Mapping Urban Areas," *IEEE Transaction on Geoscience and Remote Sending*. 41 (9), 1907-1919 (2003).
4. S. R. Falke, R. B. Husar and B. A. Schichtel, "Fusion of SeaWiFS and TOMS satellite data with surface observations and topographic data during extreme aerosol events," *J.Air Waste Manag.Assoc*. 51 (11), 1579-1585 (2001).
5. C. C. Goillot, "Airborne thermography or infrared remote sensing," *Bibl.Radiol*. (6) (6), 237-248 (1975).
6. Tahir Husain and Suhail M. Khan, "Impact assessment and forecasting of soot from Kuwaiti oil fires using a modeling approach," *Atmos.EnvIRON*. 28 (13), 2175-2196 (1994).
7. Jeffery T. McQueen and Roland R. Draxler, "Evaluation of model back trajectories of the Kuwait oil fires smoke plume using digital satellite data," *Atmos.EnvIRON*. 28 (13), 2159-2174 (1994).
8. C. Morisset, D. Schaerer, et al. "Mid-IR Observations of Galactic H II Regions: Constraining Ionizing Spectra of Massive Stars and the Nature of the Observed Excitation Sequences," *Astronomy and Astrophysics*. 415 (2), 577-594 (2004).
9. Department of the Air Force. "Defense Support Program Satellites," 22 October 2004.  
<http://www.af.mil/factsheets/factsheet.asp?fsID=96>
10. Department of the Air Force. Defense Support Program. DTIC PE Number 0305911F. February 2000.
11. A. Goldberg, "Infrared signatures of the muzzle flash of a 120 mm tank gun and their implications for Kinetic Energy Active Protection System (KEAPS)," ARL-TR-909. (Army Research Laboratory, October 2001).
12. Fontijn, "Kinetics of Propellant Combustion and Muzzle Flash Reactions," ADA146109 (DTIC, 28 Nov 1990).
13. Military.com. "BRINGING DOWN THE HOUSE: Military Demolitions and Explosives," 22 October 2004.  
[http://www.military.com/soldiertech/0,14632,Soldiertech\\_Explosives,,00.html](http://www.military.com/soldiertech/0,14632,Soldiertech_Explosives,,00.html)
14. A.N. Dills, Classification of battle space detonations from temporally-resolved multi-band imagery and mid-infrared spectra. PhD dissertation, AFIT/DS/ENP/04-2, Air Force Institute of Technology (2005).
15. Y.B. Zel'dovich and Y.P. Raizer, *Physics of Shock Waves and High-Temperature Hydrodynamic Phenomena*. Mineola, New York: Dover Publications, Inc., 2002.



16. "Engineering Design Handbook. Principle of Explosive Behavior", Army Materiel Command, AD900260 (DTIC, 10 Apr 1972).
17. W. Fickett and W.C. Davis, Detonation Theory and Experiment. Mineola, New York: Dover Publications, Inc., 2000.
18. Josef Köhler, Explosives, 4<sup>th</sup> Ed. New York: VCH, 1993.
19. Paul W. Cooper, Explosives Engineering. New York: Wiley-VCH, 1997.
20. Frank M. White, Fluid Mechanics, 2<sup>nd</sup> Ed. New York: McGraw-Hill, Inc., 1986.
21. Philip J. DiNenno, et al., SFPE Handbook of Fire Protection Engineering, 2<sup>nd</sup> Ed. Boston: Society of Fire Protection Engineers, 1995.
22. D.A. Freiwald and R.A. Axford, "Approximate Spherical Blast Theory Including Source Mass," Journal of Applied Physics. 46 (3). 1171-1174 (1975).
23. Thomas A. Leonard and Peter Hammerling. "Spherical Shock Development Near Laser Heated Microshell Targets." Journal of Applied Physics. 51 (12). 6130-6133 (1980).
24. David B. Geohegan. "Fast Intensified-CCD Photography of YBa<sub>2</sub>Cu<sub>3</sub>O<sub>7-x</sub> Laser Ablation in Vacuum and Ambient Oxygen." Applied Physics Letters. 60(22). 2732-2734 (1992).
25. A. Misra and R.K. Thareja. "Investigation of Laser Ablated Plumes Using Fast Photography." IEEE Transaction on Plasma Science. 27(6). 1553-1558 (1999).
26. S.C. Miller and T.M. Fitzgerald, "Bronze Scorpio Test Report," NASIC/DEMB, 31 January 2005.
27. Bryan J. Steward, "Dual Thrust Smokey SAMs: NIR Quick-look," AFIT/ENP (bryan.steward@afit.edu), 04 November 2005 (unpublished).
28. Bryan J. Steward, "Muzzle Flash Test: NIR Quick-look," AFIT/ENP (bryan.steward@afit.edu), 08 December 2005 (unpublished).
29. Kevin Gross, Bryan Steward, Trevor Warren, and Glen Perram, "Conventional and Q30 Flashless Gunpowder Preliminary Test Report," AFIT/ENP (glen.perram@afit.edu), 20 January 2006.
30. "Speed of Sound" 25 December 2005. <http://hyperphysics.phy-astr.gsu.edu/hbase/sound/souspe.html>
31. "History: Weather Underground" 20 December 2005. [http://www.wunderground.com/history/airport/KNYL/2005/11/18/DailyHistory.html?req\\_city=NA&req\\_state=NA&req\\_statename=NA](http://www.wunderground.com/history/airport/KNYL/2005/11/18/DailyHistory.html?req_city=NA&req_state=NA&req_statename=NA)
32. L. E. Fried, W. M. Howard, P. C. Souers, and P.A. Vitello. computer code CHEETAH 3.0 (cheetah@llnl.gov, Energetic Materials Center, Lawrence Livermore National Laboratory, Livermore, CA 94551)
33. J. Orson, Collection of detonation signatures and characterization of spectral signatures. MS thesis, AFIT/GSO/ENP/00M-01. Graduate School of Engineering and Management, Air Force Institute of Technology (AU), Wright-Patterson AFB OH, March 2000 (ADA381528)

34. J. Orson, W. F. Bagby, and G. P. Perram, "Infrared signatures from bomb detonations," *Infrared Physics & Technology*, 44: 101-107 (2003).
35. W. F. Bagby, *Spectral and Temporal Characterization of High-Temperature Events*. MS thesis, AFIT/GAP/ENP/01M-01, Graduate School of Engineering and Management, Air Force Institute of Technology (AU), Wright-Patterson AFB OH, March 2001 (ADA392540)
36. Kevin Gross, PhD Prospectus, Air Force Institute of Technology, June 2004 (unpublished).
37. A.N. Dills, K. C. Gross, and G. P. Perram. "Detonation discrimination techniques using a Fourier Transform Infrared Spectrometer system and a Near-Infrared Focal Plane Array," *Targets And Backgrounds IX: Characterization And Representation*, SPIE's AeroSense, 2003.

## **Vita**

Bryan J. Steward graduated from Mountain Ridge High School in Glendale, Arizona. He entered undergraduate studies at the University of Arizona in Tucson where he graduated Summa Cum Laude with Honors with a Bachelor of Science degree in Optical Sciences and Engineering. Later that same year, he received a National Defense Science and Engineering Graduate Fellowship to study Applied Physics at the Air Force Institute of Technology. Upon graduation, he will continue his studies at the Air Force Institute of Technology to pursue a Doctoral Degree in Optics.

REPORT DOCUMENTATION PAGE			Form Approved OMB No. 074-0188		
The public reporting burden for this collection of information is estimated to average 1 hour per response, including the time for reviewing instructions, searching existing data sources, gathering and maintaining the data needed, and completing and reviewing the collection of information. Send comments regarding this burden estimate or any other aspect of the collection of information, including suggestions for reducing this burden to Department of Defense, Washington Headquarters Services, Directorate for Information Operations and Reports (0704-0188), 1215 Jefferson Davis Highway, Suite 1204, Arlington, VA 22202-4302. Respondents should be aware that notwithstanding any other provision of law, no person shall be subject to a penalty for failing to comply with a collection of information if it does not display a currently valid OMB control number. <b>PLEASE DO NOT RETURN YOUR FORM TO THE ABOVE ADDRESS.</b>					
1. REPORT DATE (DD-MM-YYYY) 22-03-2006		2. REPORT TYPE Master's Thesis		3. DATES COVERED (From - To) August 2004 - March 2006	
4. TITLE AND SUBTITLE  REPRODUCIBILITY, DISTINGUISHABILITY, AND CORRELATION OF FIREBALL AND SHOCKWAVE DYNAMICS IN EXPLOSIVE MUNITIONS DETONATIONS			5a. CONTRACT NUMBER		
			5b. GRANT NUMBER		
			5c. PROGRAM ELEMENT NUMBER		
6. AUTHOR(S)  Steward, Bryan J., Civilian			5d. PROJECT NUMBER		
			5e. TASK NUMBER		
			5f. WORK UNIT NUMBER		
7. PERFORMING ORGANIZATION NAMES(S) AND ADDRESS(S) Air Force Institute of Technology Graduate School of Engineering and Management (AFIT/EN) 2950 Hobson Way, Building 640 WPAFB OH 45433-8865			8. PERFORMING ORGANIZATION REPORT NUMBER  AFIT/GAP/ENP/06-19		
9. SPONSORING/MONITORING AGENCY NAME(S) AND ADDRESS(ES) Sharon Staley National Air and Space Intelligence Center (NASIC/DEMI) 4180 Watson Way Wright-Patterson AFB, OH 45433			10. SPONSOR/MONITOR'S ACRONYM(S) NASIC/DEMI		
			11. SPONSOR/MONITOR'S REPORT NUMBER(S)		
12. DISTRIBUTION/AVAILABILITY STATEMENT  APPROVED FOR PUBLIC RELEASE; DISTRIBUTION UNLIMITED					
13. SUPPLEMENTARY NOTES					
14. ABSTRACT The classification of battlespace detonations, specifically the determination of munitions type and size using temporal and spectral features of infrared emissions, is a particularly challenging problem. The intense infrared radiation produced by the detonation of high explosives is largely unstudied. Furthermore, the time-varying fireball imagery and spectra are driven by many factors including the type, size and age of the chemical explosive, method of detonation, interaction with the environment, and the casing used to enclose the explosive. To distinguish between conventional military munitions and improvised or enhanced explosives, the current study investigates fireball expansion dynamics using high speed, multi-band imagery. Instruments were deployed to three field tests involving improvised explosives in howitzer shells, simulated surface-to-air missiles, and small caliber muzzle flashes. The rate of shockwave expansion for the improvised explosives was determined from apparent index of refraction variations in the visible imagery. Fits of the data to existing drag and explosive models found in the literature, as well as modifications to these models, showed agreement in the near- and mid-fields (correlation coefficient, $r^2 > 0.985$ for $t < 50$ msec); the modified models typically predicted the time for the shockwave to arrive a kilometer away to better than 10%; and fit parameters typically had an uncertainty of less than 20%. The shockwave was distinctive (Fisher Ratio, $FR > 1$ ) within the first 2-10 milliseconds after detonation, then it decayed to an indistinguishable acoustic wave (coefficient of variation, $CV < 0.05$ ). The area profiles of the fireballs were also examined and found to be highly variable, especially after 10 milliseconds ( $CV > 0.5$ ), regardless of munitions type. Scaling relationships between properties of the explosive (mass, specific energies, and theoretical energies) and detonation areas, characteristic times, and properties of the shockwave were assessed for distinguishing weights and types: Efficiency decreased with mass ( $FR > 19$ ); early-time Mach number and overpressure were primarily dependent on energy release ( $FR \sim 1.5-10$ ); fireball area increased cubically with specific energies ( $r^2 \sim 0.3-0.76$ ) but its time of occurrence decreased cubically ( $r^2 \sim 0.4-0.67$ ). The relationship between fireball and shockwave features was fairly independent of variability ( $r^2 \sim 0.5-0.9$ ), indicating that both fireball and shockwave features scale similarly with variability in detonations.					
15. SUBJECT TERMS Detonation, explosive munition, shockwave, fireball, correlation, reproducibility, distinguishability.					
16. SECURITY CLASSIFICATION OF:		17. LIMITATION OF ABSTRACT	18. NUMBER OF PAGES	19a. NAME OF RESPONSIBLE PERSON	
a. REPORT	b. ABSTRACT			c. THIS PAGE	Glen P. Perram, Dr. (ENP)
U	U	UU	171	19b. TELEPHONE NUMBER (Include area code) (937) 255-3636, ext 4504 (glen.perram@afit.edu)	